

KINETICS OF MARTENSITIC INTERFACE MOTION

by

MICA GRUJICIC

B.S., Belgrade University, Yugoslavia  
(1975)

M.S., Belgrade University, Yugoslavia  
(1978)

Submitted in partial fulfillment of the requirements  
for the degree of

DOCTOR OF PHILOSOPHY

at the

MASSACHUSETTS INSTITUTE OF TECHNOLOGY

June, 1983

© Massachusetts Institute of Technology 1983

Signature of Author \_\_\_\_\_  
Department of Materials Science and Engineering  
April 29, 1983

Certified by \_\_\_\_\_  
Walter S. Owen  
Thesis Supervisor

Certified by \_\_\_\_\_  
Gregory B. Olson  
Thesis Supervisor

Accepted by \_\_\_\_\_  
Robert W. Balluffi  
Chairman, Departmental Committee on Graduate Students

Archives  
MASSACHUSETTS INSTITUTE  
OF TECHNOLOGY

JUN 21 1983

LIBRARIES

## KINETICS OF MARTENSITIC INTERFACE MOTION

by

MICA GRUJICIC

Submitted to the Department of Materials Science and Engineering  
on April 29, 1983, in partial fulfillment of the requirements  
for the degree of Doctor of Philosophy

## ABSTRACT

Thermoelastic  $\beta$ -CuAlNi alloys were chosen to study the intrinsic mobility of martensitic interfaces and the nature of the rate controlling mechanism of the interface motion. The mobility of  $\beta_1$ - $\gamma_1'$  martensitic interfaces in these alloys was investigated using stress-assisted single-interface transformations over a temperature range of 180 to 410K and imposed interfacial velocities of  $10^{-6}$  to  $10^{-2}$  m/s. The behavior is consistent with thermally-activated interfacial motion, although an anomalous temperature dependence was observed below 210K. This anomaly appears to be related to the softening of elastic constants,  $C'$  and  $C_{11}$ , which was observed in the same temperature region.

The measured mobility of the interface at temperatures above 210K was interpreted in terms of the theory of thermally-activated deformation in order to identify possible mechanisms for the thermally-activated motion. A new concept of the activation volume was introduced, which could be used for both line and surface dislocations, allowing direct comparison of the interaction of each with a given obstacle. The thermal activation analysis of the measured behavior yielded an obstacle profile, defining the force-distance characteristics of the interface/obstacle interaction. The overall profile shape and the large activation volumes of  $10^3$  and  $10^4$  atomic volumes suggested rate control by interaction with discrete particles. Subsequent transmission electron microscopy examination revealed the presence of various precipitates of different size, as well as fine scale modulations described as a tweed or mottled structure.

In order to obtain a quantitative rationale for the measured behavior, various possible mechanisms of motion of a  $\beta_1$ - $\gamma_1$  interface, treated as a dislocation array, were modelled. It was shown that the Peierls barrier for an interface is associated with a very low activation energy, which is easily surmountable by thermal activation, and excludes it from being a rate controlling mechanism of interface motion in the temperature range investigated. Interaction of a  $\beta_1$ - $\gamma_1$  interface with discrete obstacles was considered in a systematic manner. In order to obtain solutions applicable to general martensitic interfaces, some appropriate dimensionless

interaction parameters were used. Ultimate comparison of the measured behavior with predictions of the models indicates that the mobility of the  $\beta_1$ - $\gamma_1$  interface above 210K is indeed controlled by interaction with discrete particles. The modulus and the strain interactions appeared to be the most likely rate controlling mechanisms. This refers to both the thermal and athermal components of the measured friction stress (driving force). A fine scale particle dispersion (tweed structure) accounts for the major contribution to the thermal component, whereas coarser scale precipitation gives rise to the athermal part. Possible limitations of the generality of the observed behavior are discussed.

Thesis Supervisor: Walter S. Owen  
Title: Professor of Physical Metallurgy

Thesis Supervisor: Gregory B. Olson  
Title: Principal Research Associate

TABLE OF CONTENTS

<u>Chapter Number</u>		<u>Page Number</u>
	TITLE PAGE .....	1
	ABSTRACT .....	2
	TABLE OF CONTENTS .....	5
	LIST OF FIGURES .....	7
	LIST OF TABLES .....	15
	ACKNOWLEDGEMENTS .....	16
1	INTRODUCTION .....	17
2	BACKGROUND .....	19
	2.1 Structure and Mobility of Martensitic Interfaces .....	19
	2.1.1 Models of martensitic interface structure ..	19
	2.1.2 Observations of martensitic interface structure .....	28
	2.1.3 Mobility of martensitic interfaces .....	29
	2.1.4 Accommodation modes of the transformation shape change .....	34
	2.2 Kinetics of Dislocation Motion .....	36
	2.2.1 Introduction .....	36
	2.2.2 Continuous glide .....	36
	2.2.3 Thermally activated glide .....	39
3	STATEMENT OF THE PROBLEM AND DIRECTION OF RESEARCH .....	48
4	EXPERIMENTAL PROCEDURES .....	50
	4.1 Materials and Heat Treatment .....	50
	4.2 Compression Testing .....	52
	4.3 Elastic Constant Measurements .....	53
	4.4 Transmission Electron Microscopy .....	54

TABLE OF CONTENTS (Cont'd.)

<u>Chapter Number</u>		<u>Page Number</u>
5	EXPERIMENTAL RESULTS .....	55
	5.1 Compression Testing .....	55
	5.1.1 Load-displacement curves as a function of temperature and crosshead speed .....	55
	5.1.2 Temperature and velocity dependence of the friction stress .....	57
	5.2 Thermal Effect of the Single-Interface Stress-Induced $\beta_1$ - $\gamma_1'$ Martensitic Transformation ....	63
	5.3 Elastic Constants .....	65
	5.4 Data Analysis .....	70
	5.5 Transmission Electron Microscopy .....	77
	5.5.1 Introduction .....	77
	5.5.2 Dislocations in the Metastable $\beta_1$ -Phase .....	77
	5.5.3 $\gamma$ -phase precipitation .....	79
	5.5.4 2H-type precipitates .....	86
	5.5.5 Tweed structure .....	120
6	MODELS .....	124
	6.1 Prediction of the $\beta_1$ - $\gamma_1'$ Interface Structure .....	124
	6.2 The Peierls Energy of an Interface .....	133
	6.3 Stress Field of the $\beta_1$ - $\gamma_1'$ Interface .....	138
	6.4 Interaction of a Moving Interface with Discrete Second-Phase Particles .....	141
	6.4.1 Long-range interactions .....	143
	6.4.2 Short-range interactions .....	170
	6.4.3 Derivation of driving force-activation volume relations .....	175
7	DISCUSSION .....	177
	7.1 Comparison of Model and Experimental Results .....	177
	7.1.1 $\gamma$ -phase precipitates .....	178
	7.1.2 2H-phase precipitates .....	179
	7.1.3 Tweed structure .....	181
	7.1.4 Other prospective mechanisms of interaction..	184

TABLE OF CONTENTS (Cont'd.)

<u>Chapter Number</u>		<u>Page Number</u>
7.2	Anomalous Behavior at Temperatures Below $\sim 210\text{K}$ .....	187
7.3	Kinetics of Martensitic Interface Motion .....	189
8	CONCLUDING REMARKS .....	195
9	SUGGESTIONS FOR FUTURE WORK .....	198
APPENDIX A	HEAT TRANSFER ANALYSIS FOR A SINGLE INTERFACE MARTENSITIC TRANSFORMATION .....	200
APPENDIX B	MODULUS INTERACTION BETWEEN THE $\beta_1-\gamma_1^1$ MARTENSITIC INTERFACE AND A SECOND PHASE PARTICLE .....	205
APPENDIX C	STRAIN INTERACTION BETWEEN THE $\beta_1-\gamma_1^1$ MARTENSITIC INTERFACE AND A SECOND PHASE PARTICLE .....	210
REFERENCES	.....	218
BIOGRAPHICAL NOTE	.....	226

LIST OF FIGURES

<u>Figure Number</u>		<u>Page Number</u>
1	Olson-Cohen discrete dislocation model of martensitic interface: (a) coherency dislocations producing macroscopic shape strain $E$ , (b) coherency dislocations producing complementary shear, $P^{-1}$ , (c) anticoherency dislocations producing lattice-invariant deformation $P$ , (d) total interfacial structure .....	27
2	Hypothetical obstacle profiles: (a) an unsheared profile, friction stress, $\tau$ , vs. total area, $a$ ; (b) a sheared profile: friction stress $\tau$ vs. activation area, $a^*$ . $\hat{\tau}$ -mechanical threshold stress, $\tau_{app}$ -applied stress. $\Delta G$ -activation energy and $b$ -the Burgers vector .....	42
3	Typical stress (driving force) - displacement curves for isothermal constant-velocity single-interface $\beta_1-\gamma_1^+$ martensitic transformation: (a) $A_s < T < A_f + 20K$ , (b) $T > A_f + 20K$ .....	56
4	Temperature and velocity dependence of friction stress (driving force) for alloy A .....	58
5	Temperature and velocity dependence of friction stress (driving force) for alloy B1 .....	60
6	Temperature and velocity dependence of friction stress (driving force) for alloy B2 .....	61
7	Temperature and velocity dependence of friction stress (driving force) for alloy B3 .....	62

## (List of Figures, Continued)

<u>Figure Number</u>		<u>Page Number</u>
8	The thermal effect, $\Delta T(K)$ , due to single-interface stress induced $\beta_1-\gamma_1'$ martensitic transformation, recorded by two thermocouples, located at two different positions along the specimen: (a) T/C#1, $x=5\text{mm}$ ; (b) T/C#2, $x=9.5\text{mm}$ . Position of the moving interface as well as the locations of the thermocouples are specified with respect to the end of the specimen where nucleation of the single-martensitic variant occurred. The numbers on the plots give the interface velocity in m/s. ....	64
9	Temperature dependence (a) of the elastic constants $C_{11}$ , $C_{12}$ and $C_{44}$ and of the anisotropy ratio $A$ , and (b) of the bulk modulus $B$ and two shear elastic constants $C_{44}$ and $C^1$ for the alloy B1 .....	66
10	Polar plots of $T_2$ mode shear elastic constants with: (a) wave vector $\vec{k}_\perp[001]$ , polarization vector $\vec{\epsilon}_\perp[001]$ , and (b) $\vec{k}_\perp[\bar{1}10] \cdot \vec{\epsilon}[\bar{1}10]$ for alloy B1 .....	68
11	Activation energy vs. friction stress (driving force) for alloys A and B1 .....	72
12	Thermal component of friction stress (driving force) vs. activation volume for alloys A and B1 .....	76
13	Bright-field image of the alloy B1, showing a typical dislocation structure observed ..	78
14	Bright-field images of the alloy B1 showing a coarse-scale $\gamma$ -phase precipitation. Two different thin foil orientations were used: (a) $z \sim 110$ , and (b) $z \sim 001$ .....	80
15	The $[001]\beta_1$ electron diffraction patterns of the alloy B1, corresponding to (a) the parent phase, and (b) coarse precipitates..	82



## (List of Figures, Continued)

<u>Figure Number</u>		<u>Page Number</u>
16	Electron diffraction patterns associated with the coarse $\gamma$ -precipitates in the alloy B1: (a) $[120]_{\beta_1}$ and (b) $[11\bar{3}]_{\beta_1}$ .....	84
17	The $\sim[001]_{\beta_1}$ electron diffraction pattern, (a), corresponding to the bright-field image, (b), of the alloy B2 .....	87
18	The $\sim[001]_{\beta_1}$ diffraction pattern, (a), and the corresponding high-magnification bright-field image, (b), of the alloy B2 .....	90
19	The $\sim[001]_{\beta_1}$ diffraction pattern, (a), and the corresponding dark-field micrograph, (b), of the same area shown in Figure 17 .....	92
20	The $\sim[001]_{\beta_1}$ diffraction pattern, (a), and the corresponding higher magnification dark-field image, (b), of the alloy B2 .....	94
21	The $\sim[0\bar{1}1]_{\beta_1}$ diffraction pattern, (a), and the corresponding bright-field image, (b), of the alloy B2 .....	97
22	The $\sim[0\bar{1}1]_{\beta_1}$ diffraction pattern, (a), and the corresponding dark-field image, (b), of the same area shown in Figure 21b .....	99
23	The exact $[001]_{\beta_1}$ diffraction pattern, (a), in the alloy B2 and the corresponding index diagram, (b). See the text for the meaning of symbols in the index diagram .....	101
24	An $\sim[001]_{\beta_1}$ diffraction pattern, (a), in the alloy B2 and the corresponding index diagram, (b), which postulates the existence of the 2H-phase precipitates .....	104
25	The exact $[\bar{1}13]_{\beta_1}$ diffraction pattern in the alloy B2, (a), and the corresponding index diagram, (b), which postulates a presence of the 2H-phase precipitates .....	107

## (List of Figures, Continued)

<u>Figure Number</u>		<u>Page Number</u>
26	An $\sim[\bar{1}13]_{\beta_1}$ diffraction pattern in the alloy B2, (a), and the corresponding index diagram, (b), which postulates a presence of the 2H-phase precipitates .....	109
27	The exact $[1\bar{1}2]_{\beta_1}$ diffraction pattern in the alloy B2, (a), and the corresponding index diagram, (b), which postulates an existence of the 2H-phase precipitates .....	111
28	The exact $[1\bar{1}1]_{\beta_1}$ diffraction pattern in the alloy B2, (a), and the corresponding index diagram, (b), which assumes a presence of the 2H-phase precipitates .....	113
29	An $[1\bar{1}1]_{\beta_1}$ diffraction pattern in the alloy B2, (a), and the corresponding index diagram, (b), which postulates a presence of the 2H-phase precipitates .....	115
30	The exact $[0\bar{1}1]_{\beta_1}$ diffraction pattern of the alloy B2, (a), and the corresponding index diagram, (b), which postulates a presence of the 2H-phase precipitates .....	118
31	Typical tweed (mottled) structure in Cu-Al-Ni alloys, alloy B1. Orientation of the foil $\sim[001]_{\beta_1}$ .....	121
32	Computed configuration of most significant coherency dislocations in $\beta_1-\gamma_1'$ interface (parent phase is taken as the reference lattice) .....	131
33	Computed configurations of most significant coherency dislocations in $\beta_1-\gamma_1'$ interface ( $\gamma_1'$ martensite is taken as the reference lattice) .....	132
34	Discrete dislocation model of an $\beta_1-\gamma_1'$ martensitic interface: (a) twinning dislocations producing second variant of martensite, $\gamma_1'$ (II); (b) "coherency" dislocations which cancel out long-range stress field of the twinning dislocations; (c) total interfacial structure .....	139

## (List of Figures, Continued)

<u>Figure Number</u>		<u>Page Number</u>
35	Constant-stress contours for a simplified dislocation model of an $\beta_1-\gamma_1'$ martensitic interface .....	142
36	Obstacle profiles corresponding to the modulus interaction between the $\beta_1-\gamma_1'$ interface and a second-phase particle. Shear elastic moduli of the parent phase and the martensite are taken to be equal. This is the small particle solution which neglects a variation of the interaction force through the particle. Different curves correspond to different paths of the particle, as shown in (a) .....	147
37	Sheared obstacle profiles corresponding to the unsheared obstacle profiles of Figure 36 ..	149
38	Interaction force dependence of the activation energy corresponding to the obstacle profiles shown in Figures 36 and 37. Curve numbers refer to different particle paths, see Figure 36a .....	150
39	Average obstacle profiles associated with the modulus interaction between the $\beta_1-\gamma_1'$ interface and a second phase particle: 1-small particle approximation; 2-particle radius equal to $D/10$ ; 3-particle radius equal to $D$ . Plot (a) corresponds to the particle path 3 and plot (b) to the particle path 7 in Figure 36a. Sheared elastic moduli of the parent phase and the martensite are taken to be equal .....	152
40	Average sheared obstacle profiles corresponding to the unsheared obstacle profiles shown in Figure 39 .....	153
41	Interaction force dependence of the activation energy corresponding to the obstacle profiles shown in Figures 39 and 40. The small particle solution is not depicted .....	154

## (List of Figures, Continued)

<u>Figure Number</u>		<u>Page Number</u>
42	Average obstacle profiles associated with the modulus interaction between the $\beta_1-\gamma_1'$ interface and a 2H-phase particle with a radius $D/10$ , (a), and $D$ , (b). Curves 1 correspond to a solution which takes shear moduli of $\beta_1$ and $\gamma_1'$ to be equal. Curves 2 refer to a solution which takes shear moduli of $\gamma_1'$ and 2H-phase to be equal .....	156
43	Averaged sheared obstacle profiles corresponding to the unsheared obstacle profiles shown in Figure 42 .....	158
44	Interaction force dependence of the activation energy associated with the obstacle profiles shown in Figures 42 and 43 .....	159
45	Obstacle profiles associated with the strain interaction between the $\beta_1-\gamma_1'$ interface and a 2H-phase particle. Curve numbers refer to different transformation variants of the 2H-phase. It was assumed that $\epsilon_{ij}^T$ is the same at both sides of the interface .....	163
46	Effect of the particle path on the obstacle profile associated with the strain interaction between the $\beta_1-\gamma_1'$ interface and a 2H-particle (variant 3). $\epsilon_{ij}^T$ is assumed to be equal on both sides of the interface. Curve numbers refer to different particle paths, see Figure 36a for indexing .....	165
47	Obstacle profiles associated with strain interaction between the $\beta_1-\gamma_1'$ interface and a 2H-particle variant 3, (a), and variant 6, (b). Curve numbers refer to different $\epsilon_{ij}^T$ 's on the negative side of the x-axis: 1- $\epsilon_{ij}^T$ is equal on both sides of the x-axis; 2- and 3- $\epsilon_{ij}^T$ at the negative side of the x-axis is modified by $\xi$ and $\xi$ , respectively .....	166

## (List of Figures, Continued)

<u>Figure Number</u>		<u>Page Number</u>
48	Average obstacle profiles, (a), and average sheared obstacle profiles, (b), associated with the strain interaction between the $\beta_1-\gamma_1'$ interface and a 2H-particle, variant 3. Curve numbers refer to different particle size: 1- small particle solution; 2- and 3- particle radius equal to $D/10$ and $D$ , respectively .....	168
49	Interaction force dependence of the activation energy associated with the obstacle profiles shown in Figure 48. The small particle solution is not plotted .....	169
50	Obstacle profiles associated with the short-range interaction between an interface and a second-phase particle with different lattice friction stress, $\Delta\tau$ .....	172
51	Obstacle profile associated with an interface energy change attending the short-range interaction between an interface and a particle ....	174
52	Interaction force dependence of the activation energy for the obstacle profile shown in Figure 51 .....	174
53	Schematic representation of the critical event of an interaction between an interface and regularly distributed second-phase particles, the average planar spacing of which is $\lambda$ .....	176
54	Comparison of the measured obstacle profile, curve 1, with different obstacle profiles derived from the models for the interaction of the $\beta_1-\gamma_1'$ interface with strain (tweed) domains: curve 2 - modulus interaction; curve 3a - strain interaction, tweed domains with a tetragonal distortion; curve 3b - tweed domains of the 2H-phase; curve 4 - lattice friction stress change interaction; curve 5 - interface energy change interaction .....	183

## (List of Figures, Continued)

<u>Figure Number</u>		<u>Page Number</u>
A1	A simple model for a single interface $\beta_1-\gamma_1'$ transformation .....	200
A2	The model-derived thermal effect due to single interface stress-induced $\beta_1-\gamma_1'$ martensitic transformation expressed as a temperature increment, $\Delta T$ (K), at two positions: (a) $x=5\text{mm}$ and (b) $x=9.5\text{mm}$ which varies with a position of the moving interface. The numbers on the plots give the interface velocity in m/s .....	202
A3	The temperature profiles, $\Delta T$ (K), along the specimen length corresponding to two different positions of the moving interface: (a) $x=5\text{mm}$ ; (b) $x=9.5\text{mm}$ . The numbers on the plot give the interface velocity in m/s .....	203
A4	Variation of the interface temperature accompanying its motion. Numbers in the plot correspond to the interface velocity in m/s .....	204

LIST OF TABLES

<u>Table Number</u>		<u>Page Number</u>
1	Cu-Al-Ni Alloys Used in this Study .....	51
2	Elastic Constants (in $10^{10}$ N/m <sup>2</sup> ) and Anisotropy Ratio at Room Temperature .....	69
3	Crystallography of the $\beta_1$ - $\gamma_1$ ' Transformation .....	125
4	Coherency Dislocations in $\beta_1$ - $\gamma_1$ ' (Variant I) Interface .....	127
5	Coherency Dislocations in $\beta_1$ - $\gamma_1$ ' (Variant II) Interface .....	128
6	Coherency Dislocations in $\gamma_1$ ' (Variant I) - $\beta_1$ Interface .....	129
7	Coherency Dislocations in $\gamma_1$ ' (Variant II) - $\beta_1$ Interface .....	130

ACKNOWLEDGEMENTS

I would like to express my extreme gratitude to Professor Walter S. Owen without whose guidance and encouragement this doctoral thesis would be a difficult undertaking. Professor Owen allowed me a great deal of freedom in pursuing my research interest and for this I am greatly indebted.

Dr. Gregory B. Olson introduced me to the field of martensite and imparted upon me a sense of wonder and excitement for the interesting phenomena of martensitic transformations. His sincere interest and constant help throughout the duration of this work is greatly appreciated.

Discussions with Professor Morris Cohen and Professor Robert W. Balluffi, who served on my thesis committee, were very helpful. Their valuable comments helped me to produce this thesis in its final form.

Ms. Marge Meyer served in her usual capacity as a constant source of support and advice. Mrs. Mim Rich was very helpful with her excellent technical assistance. Mrs. Barbara Rich provided much-needed support during the course of this research and did a superb job of typing the manuscript. Mr. Keith Taylor assisted me with the TEM investigations. Discussions with Mr. Dennis M. Haezebrouck and Mr. Eric Kvam were very valuable. To all these people, I extend my sincere thanks.

Dr. L. A. Shepard of AMMRC, Watertown, Massachusetts, grew the Cu-Al-Ni single crystals used in this research. This valuable assistance is greatly appreciated.

The essentials of life as well as the overall research program were supported by the National Science Foundation.

My fellow countrymen, Mila, Zora, Vesna, Caba, Zdravko and Zoran helped make life more enjoyable.

I dedicate this thesis to my mother, Radmila, and my brother, Drasko who, in their own ways, inspired me and made it possible for me to earn this degree.



## 1. INTRODUCTION

Martensitic transformations represent an important class of displacive diffusionless transformations in which the lattice deformation has such a large shear component that the resulting strain energy governs the kinetics and determines the morphology of the transformation. This situation leads often to extraordinary difficulties in the nucleation stage of the transformation, which can be surmounted only by large driving forces, whether of chemical or mechanical origin. Once nucleated, martensite (the product of the martensitic transformation) grows by migration of its interfaces. When driven by the large driving force, due to difficult nucleation, the martensitic interfaces are observed to migrate very fast with a temperature-insensitive velocity approaching the velocity of sound in the material. This behavior suggests the absence of atomic diffusion. In the course of martensite growth and in a similar sense to the usage of this term in dislocation theory, such martensitic interfaces are said to be "glissile". A special subclass of martensitic transformations, known as "thermoelastic", are characterized by a relatively low driving force attending the nucleation process. The interfaces of the thermoelastic martensites are then always close to the equilibrium and their rate of motion is determined by the rate of change of the net-driving force. It is this relative controllability

of the growth kinetics that makes thermoelastic martensitic transformations very attractive for investigation. In the experimental part of this work, use is made of a single-interface stress-induced martensitic transformation in thermoelastic Cu-Al-Ni alloys to measure interface mobility in a low-velocity region.

Martensitic interfaces are an important class of general interphase interfaces, characterized by their high mobility. Geometrical models of the interfacial structure involve the concept of primary (misfit or anticomherency) and secondary (transformation or coherency) dislocations. To account for the unique glissile nature of martensitic interfaces, martensitic interface dislocations are required to satisfy some special conditions. These requirements appear to be consistent with the formal crystallographic theories of martensite. These, and other, structural implications of the martensitic interface mobility are addressed in this work.

A number of microscopic models for slip dislocation mechanisms of motion have been developed in the literature. These models appear to be directly applicable to martensitic interfaces provided the interface dislocations are widely separated. Closely-spaced interface dislocations, on the other hand, are expected to act in groups rather than individually. Microscopic slip models must then be appropriately modified. Modifications of existing models and development of new models for the mechanisms of martensitic interface motion are proposed.

## 2. BACKGROUND

### 2.1. Structure and Mobility of Martensitic Interfaces

#### 2.1.1. Models of martensitic interface structure

Models of the structure of grain boundaries have recently been developed much more rapidly than models of interphase interfaces. This is largely because computer simulations of the atomic structure of coincidence boundaries with a reasonably low reciprocal density of coincidence sites are reasonably straightforward, while dislocation models which usually specify the secondary dislocation content of boundaries which deviate slightly from a coincidence boundary reference state are more difficult to handle. For the interphase interfaces, comparable reference states in general do not exist, except for the quite rare cases when the lattices may be related by an invariant plane strain (IPS). Current models of interfaces are therefore based entirely on the concept of interfacial dislocations, known in the modern theory of grain boundary structure as primary and secondary dislocations.

Frank's theory (1) of the net (primary) dislocation content of a grain boundary was generalized to interfaces by Bilby (2) who also introduced the concept of the surface dislocation tensor,  $B_{ij}$ . The formal equivalence of the Frank-Bilby equation and the relations derived by Bollmann (3) in his O-lattice theory was demonstrated by Christian (4). In its simplest form, this equation specifies the net Burgers vector of the primary dislocations,  $\underline{b}_p$ , crossing any vector

$\underline{p}$  of a stress-free interface as:

$$\underline{b}_p^{(1)} = (\underline{S}^{-1} - \underline{I})\underline{p} \quad (1)$$

where the Burgers vectors are defined in a reference lattice based on the parent structure (assigned as lattice 1) and  $\underline{S}$  is the lattice deformation relating parent and product structures. A similar equation can be obtained for the primary dislocation content of the interface when the product structure is chosen for the reference lattice. It can be easily demonstrated that the primary dislocation content becomes identically zero when the interface is parallel to the invariant (habit) plane of the IPS lattice deformation. This type of interface is usually referred to as fully-coherent; conversely, stress-free interfaces, for which the Frank-Bilby equation yields a non-zero content of primary dislocations, are considered as semi-coherent. Even though these two classes of interface have certain structural features in common, and a continuous transition between the two structures can be envisaged, it is often preferred to treat them separately. This approach will be adopted in this work.

A martensitic interface, a special type of interphase interface, is required to be glissile (i.e., to move conservatively) as it is displaced. Bullough and Bilby (5) first demonstrated that the concept of the glissile semi-coherent martensitic interface is equivalent to the formal crystallographic theories of martensite (6,7).

Fully-coherent interfaces with zero primary dislocation content can be further subdivided (8) as follows:

- (i) Rational, fully-coherent interfaces;
- (ii) Irrational planar or curved interfaces slightly rotated from a rational fully-coherent orientation;
- (iii) Irrational (or high-index) fully-coherent interfaces, and
- (iv) Planar or curved interfaces rotated away from a fully-coherent irrational (or high-index) fully-coherent orientation.

For two lattices related by an IPS, there are two conjugate modes of transformation and consequently two different habit planes. In general, neither of the habits need be rational, and even when one habit is a rational low-index plane, the other will be irrational. The energy of a rational and irrational pair of conjugate interfaces, or even of a low-index and a high-index rational pair, is likely to differ very substantially (9), so that lattice matching in a formal sense is not adequate to ensure a low energy interface. According to the Bilby-Bollman equation, both interfaces have zero dislocation density, from which it follows that the formal dislocation content of an interface does not provide useful information about its energy.

Continuous migration of a rational, fully-coherent interface as a single unit (to be considered in the next section) seems unlikely

and it is generally assumed that interface mobility depends upon the formation of steps which move along the interface. An atom height step in an otherwise planar interface of exact fit is called a "transformation dislocation" (4) and may be regarded as a natural extension of the concept of a twinning dislocation (10, 11).

The effective Burgers vector of a transformation dislocation,  $\underline{b}_T$ , of step height  $d$  is defined by Christian (12) as:

$$\underline{b}_T = d \cdot \gamma \cdot \underline{d}^P + d \cdot \epsilon_n \cdot \underline{n} \quad (2)$$

where:  $\underline{d}^P$  is a unit vector in the direction of the shear component of the IPS lattice deformation,

$\underline{n}$  habit plane normal,

$\gamma, \epsilon_n$  magnitude of the shear and normal strain components.

In general, the vector  $\underline{b}_T$  is not a repeat vector of either lattice and it may be defined by a Burgers circuit construction if the reference circuit is made in a dual reference lattice consisting of the two interpenetrating real lattices in contact along the invariant plane (13). In terms of modern grain boundary theory,  $\underline{b}_T$  is often defined as a repeat vector of the DSC lattice (3).

The structure of an interface which is slightly rotated from the low-index rational habit plane, so that no new discontinuities are introduced, is best modelled as stepped sections of the habit plane. This type of interface, thus, can be represented by an array of transformation dislocations. Obviously, the extent to which any particular

interface may be usefully regarded as a discrete array of the transformation dislocations depends upon both the actual separation of the steps and on the effective width of each step. If there is an appreciable overlap of neighboring steps, the discrete model only has a formal significance and the concept of the surface dislocation (5) becomes more realistic.

When the fully-coherent interface is a high-index or irrational plane, the concept of an elementary transformation dislocation as a step between adjacent habit planes is no longer useful since the spacing of these planes is very small, and in the irrational limit zero. However, as emphasized by Olson (14), steps associated with neighboring rational (probably close-packed) planes will dominate interface structure in this case. These steps are also considered to act like transformation dislocations. Furthermore, a differential density of these transformation dislocations may be used to describe planar or curved interfaces slightly rotated away from the exact irrational (or high-index) habit plane.

Semi-coherent interfaces. The condition for a fully-coherent interface that the lattice deformation  $\underline{S}$ , relating two structures, is an IPS, cannot be met for most transformations since it implies some special relations between the dimensions of the unit cells in the two structures. Nevertheless, experiments indicate that the shape deformation,  $\underline{E}$ , undergone by large vectors, is an invariant plane strain, and thus differs from the deformation  $\underline{S}$  of small lattice vectors. The phenomenological theories of

martensites (6,7) have overcome this problem by postulating the existence of some discontinuities which restore the lattice structure but modify the shape change. The density of these discontinuities, which are in fact primary interface dislocations, often appears to be quite large. Therefore, they were considered initially as continuously distributed, which led to the concept of the surface dislocation (5). However, Owen et al. (15) emphasized that the continuous distribution of the surface dislocation could not account for the high mobility, i.e., glissile character of martensitic interfaces. Instead, the interface between the parent and product lattices was visualized as being composed of relatively large areas of full coherency separated by local regions in which strain accumulated over the coherent region is compensated by the presence of the primary dislocations. Yet, no dislocation description for the coherent regions of good matching between two lattices was recognized at that time. This might be justified only in the special case where the macroscopic habit plane is a rational low-index plane. More often, however, the habit plane is an irrational (or high-index) plane which possesses a stepped structure and accordingly is modelled in terms of transformation dislocations.

Recently, a new theory of interphase-boundary structure has been developed (16) and subsequently applied to martensitic interfaces (17). This theory combines the Bollmann discrete-lattice description of interfacial dislocations (3) with the physical concept of lattice continuity and coherency. Furthermore, it has been shown that an



interfacial dislocation is not necessarily a physical discontinuity and that for any transformation which includes a lattice deformation the coherent interface must contain partial but discrete dislocations. Consequently, a distinction between two types of interfacial dislocations was made: (a) COHERENCY DISLOCATIONS which accomplish the transformation lattice deformation while maintaining continuity of the two lattices across the interface, and (b) ANTICOHERENCY DISLOCATIONS which accomplish a lattice-invariant deformation that disrupts lattice continuity and lowers the degree of coherency across the interface. Olson (17) has shown that coherency dislocations are dominated by the step structure of the interface and demonstrated the equivalence of the coherency and transformation dislocations. Anticoherency dislocations, since they restore the lattice, were identified as primary (sometimes called misfit) interface dislocations.

If displacement of the interface is to produce a fault-free product lattice, the anticoherency dislocations have to have Burgers vectors which are corresponding lattice vectors of the two crystals. The spacing of these dislocations, which is fixed by the magnitude of the lattice invariant shear, generally will not correspond to an integer number of slip-plane spacings. Therefore, some variability in the actual dislocation spacing is expected to give the correct average. In some martensitic transformations (usually noble-metal  $\beta$ -alloys), the Frank-Bilby equation can be satisfied with an array

of discrete anticoherency dislocations, the individual Burgers vector of which is a lattice vector of the parent phase but a partial lattice vector of the martensite phase. The martensite then contains an evenly spaced (on average) array of stacking faults. Finally, if the faults cluster on adjacent planes rather than spread evenly, they coalesce into a set of twins. This suggests that lattice invariant deformation, by either slip, stacking faults, or twinning, originates from the primary interfacial dislocations.

Application of the Olson-Cohen theory of interfacial structure to martensite (18) has resulted in the martensitic interface structure shown in Figure 1. The two types of interfacial dislocations, coherency and anticoherency dislocations, have been directly related to the two deformations prescribed by the phenomenological theories of martensite (6, 7): the lattice deformation  $\underline{S}$  and lattice-invariant deformation  $\underline{P}$ , respectively. The coherency dislocations have been further separated into arrays that account for the macroscopic transformation strain,  $\underline{E}$  (Figure 1a) and the complementary ("invisible") shear portion of the lattice deformation,  $\underline{P}^{-1}$  (Figure 1b). Superposition of these coherency dislocation arrays of Figures 1a and b, with the anticoherency dislocation array of Figure 1c has created the total martensitic interface of Figure 1d.

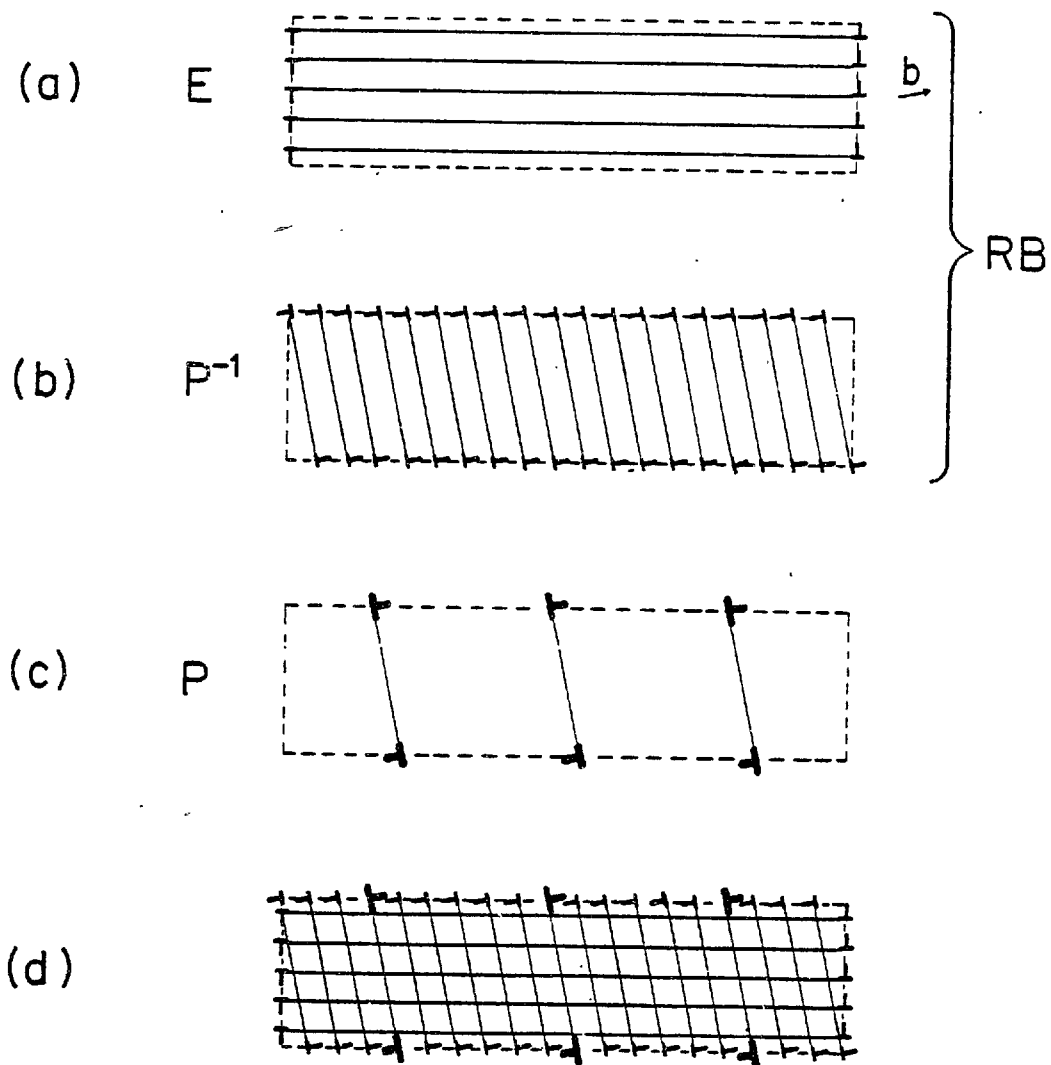


Figure 1. Olson-Cohen discrete dislocation model of martensitic interface: (a) coherency dislocations producing macroscopic shape change,  $E$  ; (b) coherency dislocations producing complementary shear,  $P^{-1}$  , (c) anticoherency dislocations producing lattice-invariant shear,  $P$  , (d) total interfacial structure.

### 2.1.2. Observation of martensitic interface structure

Since the anticoherency dislocations have the same properties as crystal-lattice dislocations (16), they are observable by conventional electron microscopy techniques, provided they are spaced sufficiently far apart to allow resolution of individual dislocations. This has already been accomplished in a number of cases (19-22). The closer spacing and smaller Burgers vectors of coherency dislocations make their resolution more difficult. In addition, the special properties of coherency dislocations can render techniques such as lattice-fringe imaging ineffective in view of the continuity of the lattice through these dislocations. Although the presence of coherency dislocations can in some cases be inferred from the bending of the lattice fringes across the interface (23), individual coherency dislocations appear to be more clearly identified by diffraction-contrast techniques. Twinning (coherency) dislocations in very thin tapering twins have already been observed in both f.c.c. (24) and b.c.c. (25) structures by means of the conventional strain-contrast technique. The same technique enabled an observation of coherency dislocations for an f.c.c.  $\rightarrow$  h.c.p. (26) martensitic transformation. Application of the weak-beam technique and the high resolution electron microscope, despite some difficulties related to the image interpretation, should in future provide more information about interfaces at near atomic level.

### 2.1.3. Mobility of martensitic interfaces

Freely growing martensites are usually divided into two classes, named by Forster and Scheil (27) as umklapp and schiebung processes.

The umklapp transformation refers to the growth of plate martensite which is often very fast, with a growth velocity of  $\sim 10^3$  m/s. This very rapid growth usually occurs at low temperatures and under high driving forces (due to difficult nucleation) and is presumed to be mainly athermal and to be limited only by various energy dissipating effects.

The schiebung process, on the other hand, corresponds to the formation of lath martensite in packets, and in iron alloys occurs above room temperature. Nominal growth rate ranges between  $10^{-3}$  and  $10^{-1}$  m/s (8) and the process appears to be akin to the thermally activated slip.

In spite of these two apparent regimes of martensite growth, it is generally agreed that the martensitic interface is very mobile. This conclusion was strengthened by different experiments on stress induced pseudo-elastic martensite (28-32) where it was shown that interface velocity adjusts itself very quickly to a change in chemical and/or mechanical driving force. Expressed in the language of dislocation slip, a martensitic interface is considered to be glissile; a property which is assumed to be closely linked to its structure. Structural aspects of the martensitic interface mobility will be discussed here.

Migration of a fully-coherent rational low-index interfaces is usually considered to proceed by the motion of steps in the interface. In this process, an island of a new layer, surrounded by a loop of coherency dislocation, is formed on a flat surface by thermal fluctuations. This then spreads across the interface under the influence of the chemical and/or mechanical driving force. The classical calculation of the rate of such a process (33) appears to be only approximate due to uncertainties about the core configuration and energy of the coherency dislocation loop. Nevertheless, the required critical size of loop, activation free energy, and driving force seem to be too large, even at moderate temperatures (33). Most of the rather sparse available evidence suggests that the new layers are formed at points of stress concentration, such as at the intersection of the growing plate with a grain boundary. Some indirect evidence has also been cited (34) for the operation of a pole mechanism (35) which provides the transformation dislocations on successive planes.

Fully-coherent irrational (or high-index rational) interfaces as well as interfaces slightly rotated away from the exact habit plane are best modelled, as already discussed, in terms of their step structure and associated array (or a number of arrays) of coherency dislocations. Olson and Cohen (16) have shown that the coherency dislocations are capable of glide and a conservative climb, but that their motion is limited to particular lattice planes. Since no long-range diffusion is required for their

motion, coherency dislocations are said to be glissile. However, the precise mechanism of coherency dislocation motion is not clear, especially when individual dislocations overlap considerably and/or when a number of intersecting coherency dislocation arrays reside in the interface.

In the simplest theory of semicoherent martensite, there is only one set of anticoherency dislocations, parallel to the (possibly irrational) invariant line of the lattice deformation  $\underline{S}$ . For the interface to be glissile, motion of anticoherency dislocations must be conservative. In other words, except in the special case of pure screw orientation, the Burgers vector must not be parallel to the interface. Slightly more complex arrays of anticoherency dislocations should also be consistent with a glissile, semicoherent interface. One possibility is for all dislocation lines to be parallel and to have the same glide planes but with two or more Burgers vectors, such that the weighted average vector satisfies the Frank-Bilby equation. Another possibility is for two or more sets of lines to have the same Burgers vector but to move in different glide planes. Again, the average of the glide vectors must satisfy the Frank-Bilby condition. Both models correspond in the crystallographic theory of martensite (6, 7) to combinations of lattice invariant shears which reduce to a simple shear. Combinations of shears which have neither the shear direction nor the shear plane in common do not reduce in this way, and it is not clear whether or not the corresponding arrays of dislocations

would produce a glissile interface.

Almost all semi-coherent martensites have irrational or high-index habit planes which must be stepped on an atomic scale. In other words, coherent regions of an interface, composed of coherency dislocations, are separated by anticoherency dislocations. Obviously, the mechanism of motion of the coherent parts of the interface is expected to be similar to that for coherent irrational martensites, already discussed. In looking for the rate-controlling mechanism of interface motion, the role of the coherency dislocations is often neglected because of their small Burgers vector. This might be justified for a case of well separated coherency dislocations. However, closely spaced dislocations would instead move in groups, acting as superdislocations with larger Burgers vectors. The friction stress to the motion of such superdislocations is expected to be comparable with the one associated with the anticoherency dislocations. This means that the contribution of coherency dislocation to the kinetics of martensitic interface motion should not be overlooked. For a twinned martensite, the Olson-Cohen theory (16) describes the interface in terms of alternating arrays of coherency dislocations with zero content of anticoherency dislocations. The interface motion kinetics is thus, in this case, completely dominated by the coherency dislocations.

A different approach to the kinetics of motion of martensitic interfaces is also worth considering. Calculations done by Olson and Cohen (17) suggest that strong attractive interaction exists



between the coherency and anticoherency dislocations. It is expected, therefore, that both driving and resisting forces can be easily transmitted along the interface. An interface is thus visualized as an elastic membrane, with a unique continuous structure. Acting as a two-dimensional dislocation analogue, the interface is characterized by a local interface normal and by the shape deformation tensor,  $\underline{E}$ .

#### 2.1.4. Accommodation modes of the transformational shape change

One of the features which define martensitic transformations is a large shape change accompanying the transformations. The surrounding matrix of growing martensite plates or laths exerts an opposing stress trying to restrict the shape change of the transforming regions. These shape-incompatibility stresses can be relaxed by either elastic or plastic strains, or, as is often the case, by a combination of the two. This provides a basis for one of the classifications of martensitic transformations as thermoelastic and nonthermoelastic transformations.

Thermoelastic behavior is defined as a relative absence of plastic accommodation of the transformational shape change (36, 37). A concept of thermoelastic equilibrium was introduced to explain the observed reversibility of these transformations and the recovery of the accompanying transformation strain. When thermoelastic systems undergo a stress-induced martensitic transformation, various phenomena, known as pseudoelasticity, shape memory effect, etc., are observed (38). It was rationalized (39) that all these phenomena have a common origin in the elastic strain accommodation of the transformational shape change. TEM investigations showed that no noticeable accumulation of defects is associated with cycling of the martensitic transformation in thermoelastic systems (39-42). However, a small plastic accommodation of the shape change, met in non ideal thermoelastic systems, gives rise to some defect formation causing a poor fatigue life associated with

transformation cycling (43).

Nonthermoelastic martensitic transformations are characterized by a substantial contribution of plastic deformation to the accommodation of the transformation shape change. The ensuing plastic zones, ahead of the advancing martensitic interfaces, are observed to have a high density of dislocations (39, 40, 44-46). A direct correlation has been found between the dislocation density and the extent of reversibility of martensitic transformation (41).

The occurrence of plastic accommodation of the shape change can effect the mobility of the martensitic interface in various ways, some inhibiting and some assisting (47). The generation of plastic zones in regions adjacent to the interface may affect the driving force acting on the interface as well as the friction stress opposing interface motion. Under some circumstances, interaction of a moving interface with dislocations within the surrounding plastic zones may become rate controlling. However, these dislocations are not an integral part of the internal structure of a martensitic interface and should be treated as prospective obstacles to interface motion.

Differences in shape accommodation mode, difficulty of nucleation, etc., from one system to another often give rise to different apparent interface mobilities. However, it is our belief that a common internal mobility exists for all martensitic interfaces, simply as a natural consequence of their common internal structure.

## 2.2. Kinetics of Dislocation Motion

### 2.2.1. Introduction

Applied stress on a body typically exerts a force on a dislocation tending to move it. The ensuing increase in the free energy of the crystal provides an internal friction stress,  $\tau_f$ , opposing the motion of a dislocation. The resulting friction stress generally varies markedly from place to place in the lattice and reaches occasional peak values referred to as the mechanical threshold stress,  $\hat{\tau}_f$ . Different concepts of the friction stress have been developed depending on whether consideration is being given to the motion of a dislocation segment or a single dislocation, or groups of dislocations (48).

Usually a distinction is made between two regimes of dislocation glide, continuous glide and thermally activated glide, which corresponds respectively to the case when the applied stress,  $\tau_{app}$ , is greater or smaller than the mechanical threshold stress. ( $\tau_{app}$  refers to the component of the applied stress tensor,  $\Sigma$ , resolved onto the glide plane of the dislocation.)

### 2.2.2. Continuous glide

According to the general concept of a force on a dislocation (49), the notion of a local driving force,  $(\tau_{app} - \tau_f)b$ , which tends to move the dislocation, has been developed, where  $b$  is the Burgers vector.

A dislocation which experiences a positive driving force everywhere throughout the crystal tends to accelerate at a rate determined by its inertial mass,  $m$ , which has been defined by Frank (50). This tendency

is opposed by drag or damping mechanisms which dissipate energy, and the classical Newtonian equation of motion can be invoked:

$$m \frac{d^2 y}{dt^2} + B \frac{dy}{dt} = (\tau_{app} - \tau_f) b \quad (3)$$

where  $y$  is the direction of dislocation motion,

$t$  is time, and

$B$  is a drag coefficient, which describes the interaction of the moving dislocation with the phonons and at low temperatures with electrons.

All proposed phonon-drag mechanisms to date (51-54) have led to representing the drag coefficient in the form:

$$B = \frac{kT}{\Omega \nu} \quad (4)$$

where  $k$  = Boltzmann's constant,

$T$  = temperature,

$\Omega$  = atomic volume, and

$\nu$  = atomic frequency.

According to equation (4), the interaction of a dislocation with phonons becomes stronger as the temperature rises, leading to a lower steady-state dislocation velocity:

$$v = \frac{\Omega \nu (\tau_{app} - \tau_f) b}{kT} \quad (5)$$

The concept of a retarding force on a moving dislocation due to the drag mechanisms, as introduced above, assumes that the dislocation

encounters more phonons from the forward direction than from the backward direction. The same concept can be applied to the case of interphase-interface dislocations which move with the interface and produce a change in structure across the interphase boundary. However, as noted by Eshelby (42) and Weertman (43), an interfacial dislocation may either gain energy or lose it, since the phonon modes will usually be different for the two structures.

Abrupt change in the local driving force on a moving dislocation may bring about two special dynamic phenomena: (a) energy radiation through the oscillating motion of segments of the dislocation, and (b) inertial effects, which have led to the concept of a dynamic threshold (48). For the usual slow variation of the driving force throughout the crystal, an average dislocation velocity and effective driving force have also been introduced, the latter being a fairly complicated function of the local driving force (48).

Johnston and Gilman (57) and Gilman (58) demonstrated experimentally that at high driving forces the dislocation velocity approaches some limiting value (the shear wave velocity) and is not a linear function of the driving force as predicted by equation (5). This was afterwards rationalized (46) by postulating different relativistic effects coming into play at velocities comparable to the shear wave velocity. These effects can alter the stress field of a dislocation and its interaction forces with other dislocations but do not influence the force on a dislocation produced by an applied stress.

### 2.2.3. Thermally activated glide

When the applied stress does not exceed the mechanical threshold of the crystal, a dislocation reaches a state of static equilibrium at places where the local driving force falls to zero. Further motion of the dislocation requires thermal activation to assist the applied stress in overcoming the barrier of the internal friction stress. Once the dislocation overcomes this barrier, it accelerates and reaches a drag-controlled velocity. This velocity is maintained until the dislocation encounters another barrier.

Apart from a thermodynamically imposed lower limit of the applied stress, there generally exist other minimum values of the applied stress,  $\tau_{\mu}$ , below which any thermal activation, even though thermodynamically feasible, may be practically neglected.  $\tau_{\mu}$  is termed the ATHERMAL RESISTING STRESS and refers to obstacles which possess long-range stress fields and large activation energies. Consequently, at stress levels below  $\tau_{\mu}$ , the influence of the thermal activation on dislocation motion is negligible. On the other hand, obstacles with short-range stress fields give rise to an effectively smaller value of the activation energy, making the thermal activation more probable. These obstacles are termed thermal obstacles and the corresponding THERMAL RESISTING STRESS is designated as  $\tau_{th}$ .

In the general case when both types of obstacles are present, thermal activation of the dislocation motion is feasible when the applied stress is greater than the athermal resisting stress.

It should be emphasized that the term "obstacle" has been used quite generally, and it does not necessarily refer to a physical entity in the crystal. Thus, any event during the dislocation motion, which is associated with a temporary or permanent increase in the energy of a crystal, brings about an internal friction stress and is considered as an obstacle. Sometimes, there is a particular physical entity behind this friction stress, but often, as in the case of the Peierls obstacle (50, 51), the friction stress is associated solely with a higher energy configuration of the moving dislocation itself.

Model activation parameters. The average dislocation velocity,  $v$ , in a thermally-activated regime is often defined as:

$$v = v_0 \exp - \frac{\Delta G}{kT} \quad (6)$$

where:  $v_0$  - the preexponential term which might be temperature dependent through the thermal expansion coefficient and temperature variation of the elastic constants. Possible variation of  $v_0$  with stress comes from the stress dependence of the vibration frequency of a dislocation segment involved in the critical event;

$\Delta G$  - the activation energy;  $\Delta G$  has the same origin for its temperature dependence as  $v_0$ . The stress dependence of  $\Delta G$  is the central issue in the theory of thermally activated slip and will be discussed in more detail later.



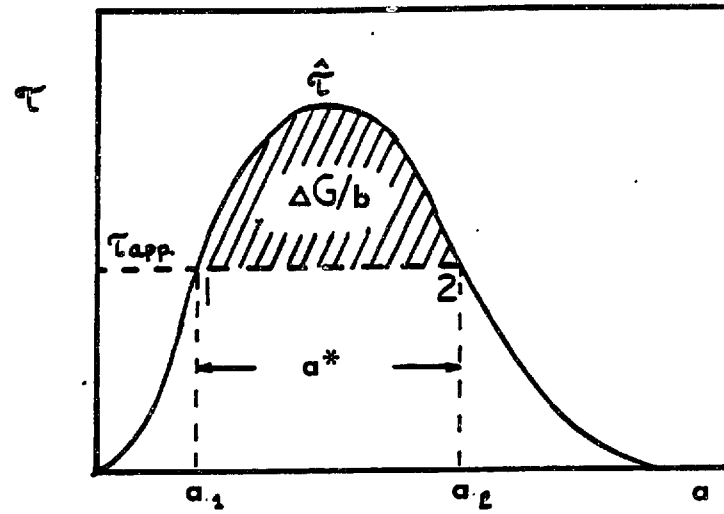
The Arrhenius type of rate equation, equation (6), even though extensively used, is strictly valid only when certain conditions, pertaining to the magnitude of the activation energy and the number of thermally activated events, are met. Otherwise, appropriate modifications of the rate equation are necessary (48).

Figure 2a shows a hypothetical obstacle profile where the friction stress,  $\tau$ , is plotted against a total area,  $a$ , swept by a dislocation during its interaction with the obstacle. The width of the obstacle profile,  $a^*$ , at any particular value of the applied stress, defines an increment in the area swept by the dislocation segment during the critical thermally activated event and is often referred to as "the true activation area".

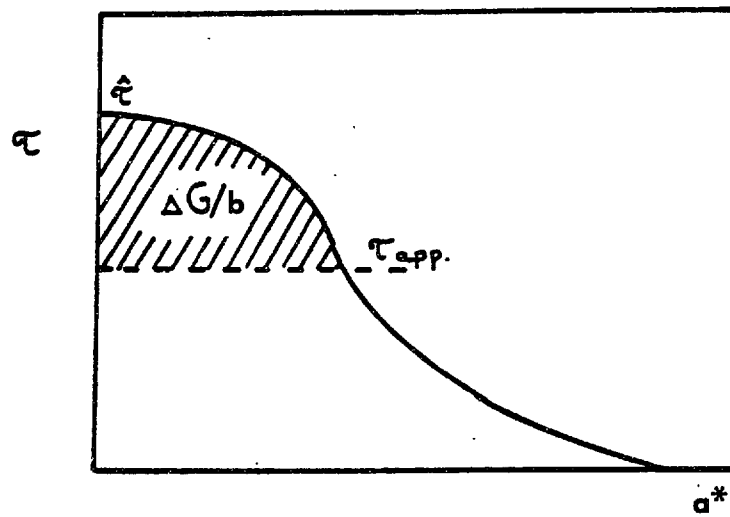
A plot showing friction stress against the activation area, as in Figure 2b, is called "the sheared obstacle profile", since it can be obtained by a simple shear of the corresponding  $\tau$  vs.  $a$  profile parallel to the  $a$ -axis. It is this sheared obstacle profile that can be derived from experimental measurements and which represents a basic material property.

According to Figure 2, the activation energy can be defined as:

$$\Delta G = b \int_{a_1}^{a_2} \tau \cdot da = b \int_{\tau_{app}}^{\hat{\tau}} a^* \cdot d\tau \quad (7)$$



a.



b.

Figure 2 Hypothetical obstacle profiles: an unsheared profile; friction stress,  $\tau$ , vs. total area,  $a$ ; and (b) a sheared profile; friction stress vs. activation area,  $a^*$ ;  $\hat{\tau}$  - mechanical threshold stress;  $\tau_{app}$  - applied stress;  $\Delta G$  - activation energy and  $b$  - the Burgers vector.

A stress dependence of the activation energy expressed as  $-(\partial\Delta G/\partial\tau)_T/b \equiv a'$ , "apparent activation area", can be defined, according to the equation (7) as:

$$a' = a^* - \int_{\tau_{app}}^{\hat{\tau}} \left( \frac{\partial a^*}{\partial \tau_{app}} \right) d\tau \quad (8)$$

The last term in the equation (8) represents a stress dependence of the obstacle profile itself and is often, but not always, negligible when compared with  $a^*$ .

The product of the Burgers vector and the corresponding activation area, either  $a'$  or  $a^*$ , is usually referred to as the true, or apparent stress activation volume,  $V_T$ . For the lattice dislocations, with a Burgers vector comparable with the spacing of the slip planes,  $V_T$  does describe the volume of the thermally-activated dislocation configuration. However, for partial dislocations, where  $b$  is a small fraction of the lattice parameter,  $V_T$  may significantly underestimate the volume of the configuration and  $a^*$  (or  $a'$ ) becomes a more basic quantity.

The magnitude of the stress activation volume, expressed in terms of the number of atomic volumes, as indicated by Conrad (62), can be used as a criterion for a selection of the rate-controlling mechanism of dislocation motion. Often, however, an exact knowledge of the obstacle profiles is needed to separate two mechanisms with comparable values of  $V_T$ .

A number of microscopic models for specific dislocation mechanisms of motion have been developed in order to explain macroscopic slip phenomena and the dependence on applied stress, strain rate, temperature and structural parameters (48). These have been used, in some cases, to distinguish between different dislocation mechanisms on the basis of macroscopic observations. Unfortunately, sometimes two different rate-controlling mechanisms of dislocation motion lead to essentially indistinguishable macroscopic behavior (48).

Operational activation parameters. Various experimental techniques provide an opportunity for measuring interrelations between rate, stress, and temperature. These interrelations are often expressed in terms of different operational activation parameters as:

Operational activation energy:

$$Q \equiv \frac{\partial \ln v}{\partial (-1/kT)}_{\tau} \quad (9)$$

Operational activation area:

$$a'' \equiv \frac{kT}{b} \left. \frac{\partial \ln v}{\partial \tau} \right|_T \quad (10)$$

and operational stress activation volume:

$$V''_{\tau} \equiv ba'' \quad (11)$$

The following relations exist between the corresponding model and operational activation parameters:

$$Q = kT \left. \frac{\partial \ln v_o}{\partial \ln \tau} \right|_{\tau} + \Delta H \quad (12)$$

and

$$a'' = \frac{kT}{b} \left. \frac{\partial \ln v_o}{\partial \ln \tau} \right|_{\tau} + a' \quad (13)$$

Operational activation analysis consists in finding ways to measure separately each of the terms on the right side of equations (12) and (13), or to prove some of them negligible and to measure the rest. This procedure usually starts by recognizing that, from the data-analysis point of view, equation (6) should be rewritten as follows:

$$v = v_o \exp(\Delta S/k) \cdot \exp -(\Delta H/kT) = v_H \exp -(\Delta H/kT) \quad (14)$$

where  $\Delta S = -(\partial \Delta G / \partial T)_{\tau}$  is the activation entropy and

$$\Delta H = -\partial(\Delta G/kT) / \partial(1/kT) \Big|_{\tau} \text{ is the activation enthalpy.}$$

A simple test can be employed to check temperature variations of  $v_H$  and  $\Delta H$ . Namely, if a  $\ln v$  vs.  $1/kT$  plot gives straight iso-stress lines, then both  $v_H$  (and  $v_o$ ) and  $\Delta H$  are temperature invariant. Equation (12), in this case, suggests that the operational activation energy,  $Q$ , is equal to the model activation enthalpy,  $\Delta H$ . The model activation entropy,  $\Delta S$ , is governed by the temperature dependence of

the elastic constants (63). Often, the contribution of  $\Delta S$  to  $\Delta G$  is negligible when compared with  $\Delta H$  and consequently the model activation energy can be approximated by the operational activation energy.

When all iso-stress straight lines in a  $\ln v$  vs.  $1/kT$  plot go through the same point at infinite temperature, the preexponential term,  $v_H$  (and  $v_0$ ) can be considered as stress independent. According to equation (13), the operational and the model activation areas, as well as the volumes, then become equal.

When the iso-stress lines in a  $\ln v$  vs.  $1/kT$  plot do not make the same intercept at the  $\ln v$ -axis, it means that the preexponential term  $v_H$  is stress dependent. Equation (14) can be differentiated to give:

$$\frac{kT}{b} \frac{\partial \ln v}{\partial \tau} \Big|_T = \frac{kT}{b} \frac{\partial \ln v_H}{\partial \tau} \Big|_T - \frac{1}{b} \frac{\partial \Delta H}{\partial \tau} \Big|_T \quad (15)$$

The first term in equation (15) represents the operational activation area and can be evaluated from a  $\ln v$  vs.  $\tau$  plot. The third term in equation (15) is, in fact, equal to  $-(dQ/d\tau)/b$  and can be determined from a plot of  $\ln v$  vs.  $1/kT$ . This term, in general, is not equal to the apparent activation area,  $-(\partial \Delta G/\partial \tau)/b$ , since the activation entropy, entering the  $v_H$  term, can also be stress dependent. Generally, it is not possible to separate contributions of  $v_0$  and  $\Delta S$  to the stress-dependence of  $v_H$  and consequently the apparent activation areas cannot be determined. However, some model-inspired estimates of the stress variations of  $v_0$  and  $\Delta S$  can be employed. For example, the stress dependence of the activation entropy is known to have two

contributions (63). The first contribution comes from the thermal expansion coefficient and often has a quite small magnitude. The second contribution is a product of a temperature dependence of the appropriate elastic modulus and an inverse slope of the obstacle profile,  $\partial \ln a^* / \partial \ln \tau|_T$ . A systematic analysis (48) has proved that the stress dependence of the activation entropy for the short-range obstacles is negligible. This means that the last term in equation (15) can be considered as the apparent activation area. For the long range obstacles, however, the stress dependence of the activation entropy may have a significant contribution to the apparent activation area and must be taken into account.

The stress dependence of  $v_0$  comes from the obstacle stiffness, which is often a very weak function of the stress.

When a  $\ln v$  vs.  $1/kT$  plot does not show straight iso-stress lines, this may be due to a temperature dependence of the activation energy or of the preexponential term. Such temperature dependences may have a simple origin. For example, many theoretical models predict that these terms should depend on the shear modulus,  $\mu$ . In this case, one can properly introduce new variables  $\tau/\mu$  and  $\mu b^3/kT$ , instead of  $\tau$  and  $1/kT$ , and employ the same analysis already discussed.

### 3. STATEMENT OF THE PROBLEM AND DIRECTION OF RESEARCH

The aims of this research are to understand the phenomenon of intrinsic mobility of martensitic interfaces and elucidate the nature of the rate controlling mechanisms of the interface motion. These problems will be approached both experimentally and theoretically.

Thermoelastic Cu-Al-Ni alloys, which undergo a single-interface stress-induced  $\beta_1-\gamma_1'$  martensitic transformation provide an ideal system for the measurement of interface mobility. Using an uniaxial compressive deformation, the single-interface mobility measurements have been conducted over a wide range of temperature and an experimentally imposed range of interface velocities extending to low velocities. The observed behavior is interpreted in terms of the theory of kinetics of slip phenomena. Possible mechanisms for the interface motion are discussed.

Ultrasonic wave velocity measurements of the parent phase have been made over a wide range of temperature in our effort to identify correlations, if any, between the change in elastic constants and interface mobility.

Transmission electron microscopy has been employed to search for the prospective rate controlling obstacles, anticipated by the observed mobility behavior. A quantitative analysis of the structure, crystallography, size, and distribution of the potential obstacles has been undertaken.



The theoretical approach to the problem of the martensitic interface mobility includes modelling of various possible mechanisms of interface motion. When convenient, most general solutions are sought. Otherwise, particular interactions of a  $\beta_1-\gamma_1'$  interface with different obstacles, observed by TEM investigations, are considered. The extent of the qualitative and quantitative agreement between the predictions of the models and experimentally observed mobilities then serve as a ground for the conclusions about the most probable rate-controlling mechanisms of the interface motion.

Models for the single-interface motion in Cu-Al-Ni alloys are subsequently used in a discussion about the more general problem of the martensitic-interface mobility. Differences in the transformation shape change, accommodation modes, critical driving force for the nucleation process, etc. from system to system certainly affect the apparent interface mobility. However, the common structural nature of all martensitic interfaces is suggestive of a common intrinsic mobility. It is, therefore, hoped that the models derived in this work will be generally applicable.

#### 4. EXPERIMENTAL PROCEDURE

##### 4.1. Materials and Heat Treatment

Cu-Al-Ni alloys were prepared from 99.99 percent Cu, 99.99 percent Al and 99.9 percent Ni by melting in a high frequency furnace under an argon atmosphere, followed by casting into a water-cooled copper mold. The resulting ingots were homogenized at 1273 K for 24 hours and chemically analyzed. Several alloy ingots of different compositions were made in order to get different parent phase stabilities with respect to the  $\beta_1$  (parent)  $\rightarrow \gamma_1'$  (martensite) transformation, Table 1. After removing oxide layers, the ingots were cut into small pieces which were used for single-crystal preparation. The single crystals, in the form of 5 mm diameter rods, were grown by the Bridgeman method using a sharp temperature gradient in a moveable vertical furnace. The ingot pieces, charged into a graphite crucible along with a  $[001]_{\beta_1}$  seed, were melted and resolidified to single crystals under an argon atmosphere. Since specimens at this stage were dendritic, they were solution treated at 1273 K for two hours in quartz capsules which were evacuated and backfilled with argon to a pressure of  $10^5$  Pa. Specimens were subsequently quenched into water. The orientation of the single crystal specimens was then determined by the Back-reflection Laue technique. The axis of the rod-shape specimens were found to be  $\sim [001]_{\beta_1}$ .

The martensitic transformation temperatures were determined by both observing the surface relief of specimens and by electrical resistance measurement during cooling.

TABLE 1. Cu-Al-Ni ALLOYS USED IN THIS STUDY

	<u>Alloy Composition</u> (wt.pct.)	<u>Heat Treatment</u>	<u>M<sub>s</sub></u>	<u>M<sub>f</sub></u>	<u>A<sub>s</sub></u>	<u>A<sub>f</sub></u>
A	Cu 13.9 Al 3.9 Ni	1073K(4min)→273K	218K	206K	249K	253K
B1	Cu 14.2 Al 3.5 Ni	1249K(10min)→273K	150K	135K	161K	172K
B2	Cu 14.2 Al 3.5 Ni	1293K(1hr)→273K	157K	142K	166K	181K
B3	Cu 14.2 Al 3.5 Ni	1293K(1hr)→273K	155K	140K	166K	177K

Several different heat treatments were employed in order to obtain a better alloy stability with respect to a  $\beta_1-\gamma_1'$  transformation, Table 1. For the heat treatments marked A, B1 and B2, Table 1, the quenching rate was kept constant within the limits of reproducibility of the quenching procedure employed.

On the other hand, a much faster quenching rate was used for heat treatment B3. A rapid quenching apparatus was constructed consisting of a narrow stainless steel tube which held the specimen in the center of the heating zone of a vertical furnace. This tube was connected to a gas reservoir, which could be filled and emptied by operating a pair of valves. The gas reservoir was pressurized with argon at 7 MPa (1 Ksi). When the pressure in the reservoir was released, it forced the specimen B3 downward into a well-stirred bath of iced-brine.

#### 4.2. Compression Testing

Compression tests of the single crystals were carried out on an Instron Machine with a 90,000 N capacity over a temperature range of 170 to 410K and an interface velocity range of  $10^{-6}$  to  $10^{-2}$  m/s. In order to achieve a better uniaxiality of the compression load, special attention was given to the parallelism of the specimen ends and a ball-bearing platen was used to prevent the specimen from slipping off under the load.

For testing at different subambient temperatures, a methanol bath was used, which was substituted by an iso-pentane bath at temperatures below 200K. The temperature was kept constant within  $\pm 1$  degree adding liquid nitrogen into the well agitated bath.

For testing at temperatures above room temperature a silicone-oil bath was used. A 300-watt immersion heater connected to a temperature controller kept the temperature of the well-stirred bath within  $\pm 1$  degree.

Some recent experiments (64-66) on Cu-Al-Ni alloys have indicated that a significant thermal effect can be associated with the latent heat of a martensitic transformation. At high transformation rates, the temperature close to the interface can increase by few tens of degrees. To measure this thermal effect, two 0.2 mm diameter iron-constantan thermocouples were mounted on the compression specimens and their position relative to the specimen ends was precisely determined. The thermocouple outputs were then recorded on a chart-recorder during compression testing.

### 4.3. Elastic Constant Measurements

The elastic constants were measured by the ultrasonic Pulse-Echo-Overlap method (67) using a Panametrics Ultrasonic Gage (Model 5221) instrument. This method of measuring ultrasonic wave velocity in solids involves a high frequency (5 - 10MHz) quartz transducer, cemented on one end of a specimen having two parallel end faces. The transducer serves both as a generator and a detector of radio frequency pulses propagating in the specimen. Each pulse results in a series of echos with a round trip travelling time  $t$ . Identical pulses are produced at regular intervals,  $1/f$ , where  $f$  is the frequency. Both signals, i.e., ultrasonic pulses and resulting echos, are viewed on an oscilloscope with its x-axis driven by an oscillator. The frequency of the oscillator is adjusted until the two signals overlap. At this condition, an inverse of the frequency of the oscillator, which is measured by a frequency counter, is equal to the round-trip travelling time of the echos. Ultrasonic wave velocity is then simply determined as a ratio of the round-trip distance (the specimen length doubled) and the travelling time.

Subambient temperature measurements of ultrasonic wave velocity were done in either a methanol or an iso-pentane isothermal bath. Temperatures in the range of 150K to room temperature were controlled within  $\pm 1$  degree.

A longitudinal wave V315 and a Normal Incident Shear Wave V221 Panasonic Videoscan Immersion transducer with frequency of 10 MHz were used. Nonaqueous Stopcock grease served as a bond between the specimen and the transverse wave transducer. Salol was used for the

longitudinal wave transducer.

All the elastic constants of the second order for the cubic  $\beta_1$ -phase could be determined by measuring three independent wave velocities of one longitudinal and two transverse waves along a  $\langle 110 \rangle_{\beta_1}$  propagation direction. Single crystal specimens were brought into a  $\langle 110 \rangle_{\beta_1}$  orientation using the Laue back-reflection technique. Typical specimens for elastic constants measurements were slabs 3mm x 4mm x 8mm ranging within  $\pm 1$  degree from the exact orientation.

#### 4.4. Transmission Electron Microscopy

Transmission electron microscopy was performed on all the alloys listed in Table 1. Both heat treated and heat treated and subsequently compression tested specimens were examined.

A typical sample was sliced into discs approximately 0.5mm thick, which were further mechanically thinned on both sides to a thickness of  $\sim 0.15$ mm. Discs of 3mm diameter were then punched and thinned to 0.03mm, both mechanically and chemically, in a solution containing 1 part HCl, 4 parts  $\text{HNO}_3$  and 5 parts of  $\text{H}_3\text{PO}_4$  at room temperature. The thinned discs were then jet polished, until a suitable hole formed, in a 3 parts methanol - 1 part  $\text{HNO}_3$  solution, at:  $-40^\circ\text{C}$ , 5 - 6 V and 20-20mA. The perforated discs were then examined at 200 kV in a JEOL 200 CX electron microscope equipped with a double-tilt stage.

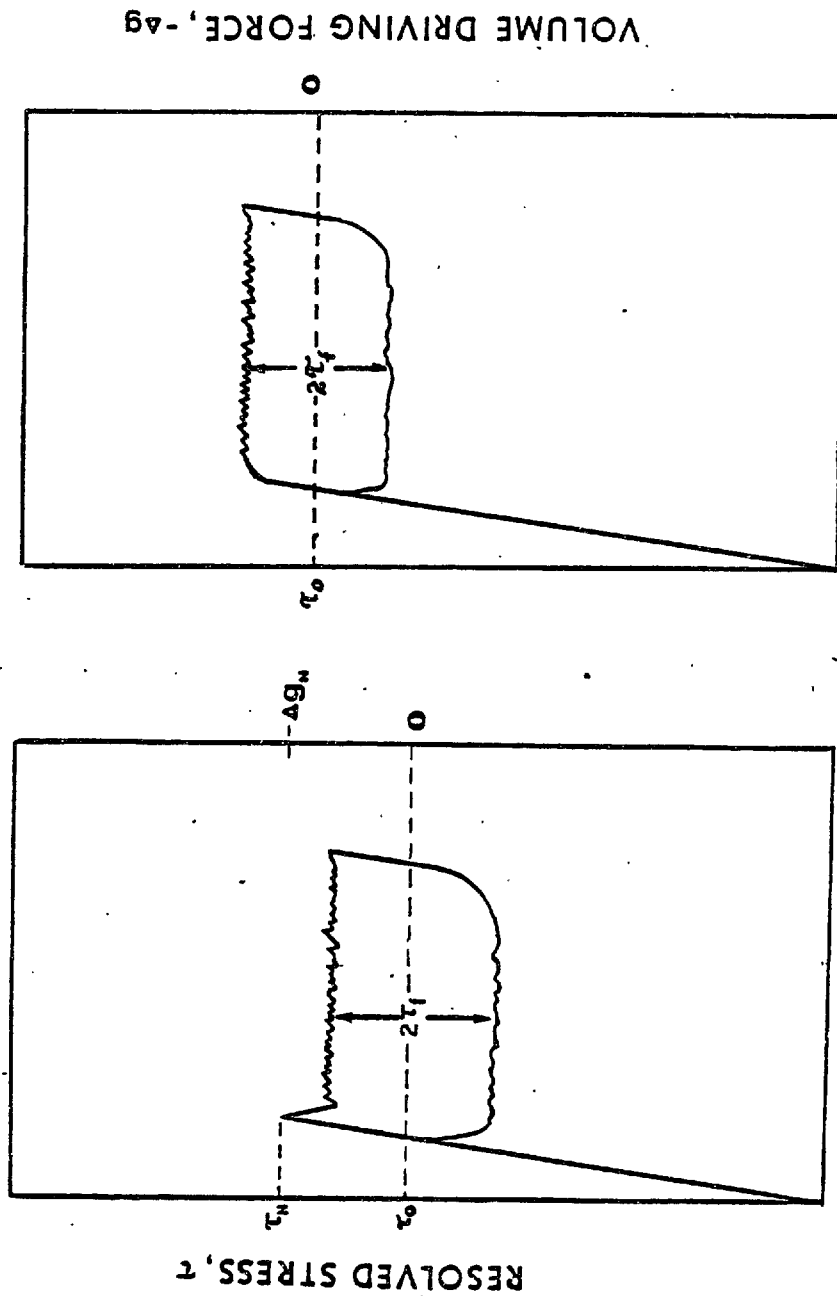
## 5. EXPERIMENTAL RESULTS

### 5.1. Compression Testing

#### 5.1.1. Load-displacement curves as a function of temperature and cross-head speed

Recorded applied load versus cross-head displacement curves were converted to resolved stress (volume driving force) versus interface displacement curves using the known transformation invariant-plane shape strain (68,69). Applied loads were resolved in the shape strain plane and direction (70) for the most favorably oriented transformation variant (71,72). Furthermore, using Christian's relation (73), a correlation between cross-head and interface position was computed and thus crosshead speed was converted into interface velocity.

Typical driving force-displacement curves as observed at temperatures above  $A_s$  are shown in Figure 3. Both resolved stress,  $\tau$ , and total driving force per unit volume,  $\Delta g$ , are indicated. At  $\tau_N$  (or  $\Delta g_N$ ), the  $\gamma'_1$ -martensite nucleates at a specimen corner. The load then drops and the interface moves forward at a nearly constant level of  $\tau$  and  $\Delta g$ . Reversing the direction of crosshead displacement, the interface moves in the reverse direction at a lower level of  $\tau$  and  $\Delta g$ . The average "friction stress",  $\tau_f$  (and the corresponding  $\Delta g$ ) is one-half of the resulting hysteresis for forward and reverse interface motion. If  $\tau_f$  is assumed equal in magnitude in both directions, the hysteresis midpoint defines  $\tau_0$  where  $\Delta g = 0$  (72,74).



DISPLACEMENT

DISPLACEMENT

Figure 3 Typical stress (driving force) - displacement curves for isothermal constant-velocity single-interface  $\beta_1 \rightarrow \beta_1'$  martensitic transformation : (a)  $A_s \leq T \leq A_f + 20K$ , (b)  $T > A_f + 20K$ .

VOLUME DRIVING FORCE,  $-\Delta G$



The shape of the driving force-displacement curves was not visibly affected by a change of interface velocity in the range  $10^{-6}$  to  $10^{-2}$   $\text{ms}^{-1}$ . However, it was observed that the hysteresis increases with interface velocity that is consistent with findings of Otsuka et al. (72) and Shepard (75).

Temperature has some effect on the shape of the driving force-displacement curves. Namely, at temperatures higher than approximately  $A_f + 20^\circ\text{K}$ , no sharp load drop was recorded. Close examination revealed that a few parallel plates of  $\beta_1'$ -martensite (76,77) formed at  $\tau_N$  before the  $\beta_1-\gamma_1'$  interface passed through. This small end effect did not affect the motion of the  $\beta_1-\gamma_1'$  interface as it approached the center of the specimen.

#### 5.1.2. Temperature and velocity dependence of the friction stress

The measured  $\tau_f$  and corresponding  $\Delta g$  values for alloy A are shown in Figure 4 for a temperature range 270 to 410 K and an interfacial velocity range of  $10^{-6}$  to  $10^{-2}$  m/s. The temperature and rate dependence of  $\tau_f$  are characteristic in both sign and magnitude of thermally-activated dislocation motion, resembling the typical behavior of the plastic flow stress. Furthermore, the value of  $\tau_f$  appears to approach a constant minimum level at the lowest velocities and highest temperatures. This suggests an "athermal" contribution to  $\tau_f$  of  $\tau_\mu \approx 22 \text{MN/m}^2$  (with a corresponding athermal level of  $\Delta g_\mu = -2.2 \text{MJ/m}^3$ ).

Due to the lower  $M_s$  temperature of all B alloys, Table 1, compression tests were carried out in a lower temperature range, 170 to 298K. The interface velocity range, however, was the same for both A

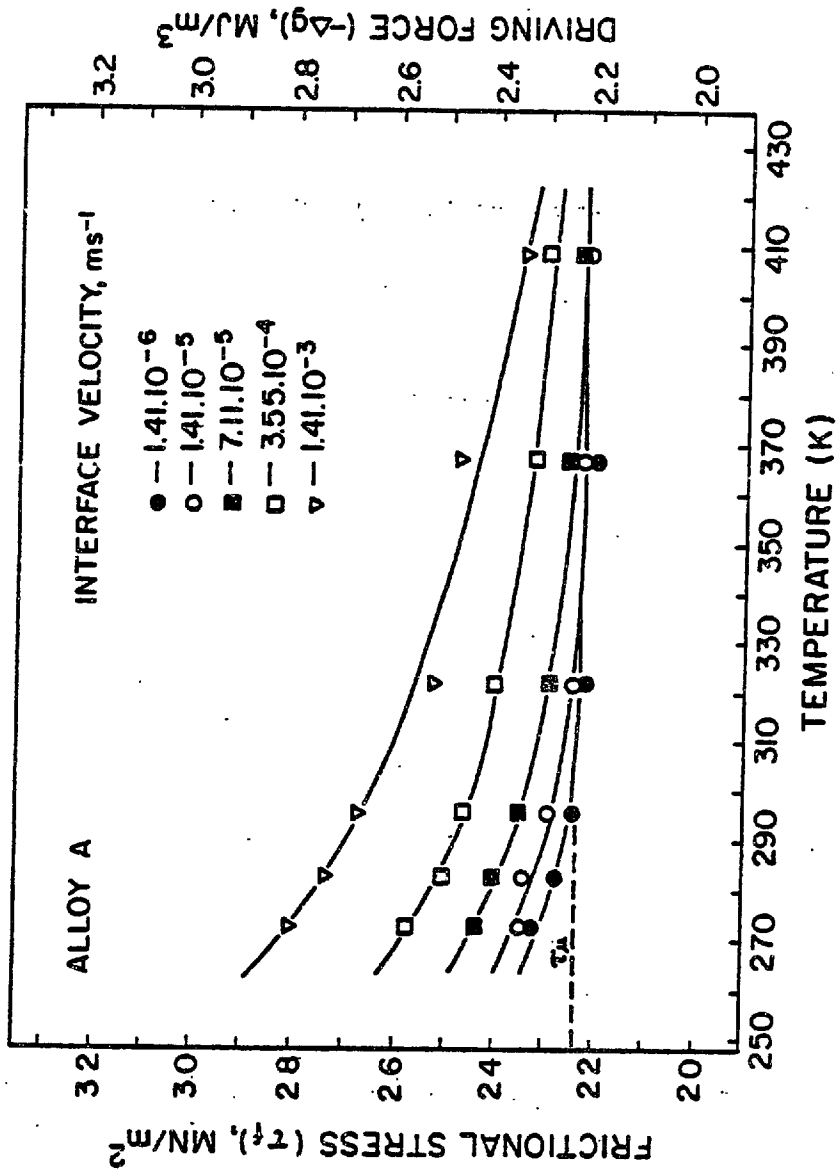


Figure 4 Temperature and velocity dependence of friction stress ( driving force) for alloy A.

and B alloys ( $10^{-6}$  to  $10^{-2}$  m/s).

Figure 5 shows the temperature and rate dependence of the frictional stress and the driving force for alloy B1. A behavior similar to that of Alloy A is found at temperatures above  $\sim 210\text{K}$ . However, an anomalous, positive temperature dependence is observed below this temperature. No noticeable change in shape of the driving force-displacement curves was recorded in this temperature range. It should be noticed that a minimum constant level of the friction stress,  $\tau_{\mu}$ , is not well defined, but seems to be lower than for alloy A, with an estimated value of  $\tau_{\mu} \approx 15\text{MN/m}^2$ ,  $\Delta g_{\mu} \approx -1.5\text{MJ/m}^3$ .

Figures 6 and 7 show temperature and rate dependence of the friction stress and the driving force for alloys B2 and B3, respectively. There is good agreement between these data and those for alloy B1, Figure 5, especially in the temperature range of a normal negative temperature dependence of  $\tau_f$  ( $T > 210\text{K}$ ). A common minimum level of friction stress is estimated as  $\tau_{\mu} \approx 15\text{MN/m}^2$ .  $\Delta g_{\mu} \approx -1.5\text{MJ/m}^3$ . A slightly higher scattering of the individual experimental data is recorded in the temperature range of anomalous behavior,  $T < 210\text{K}$ .

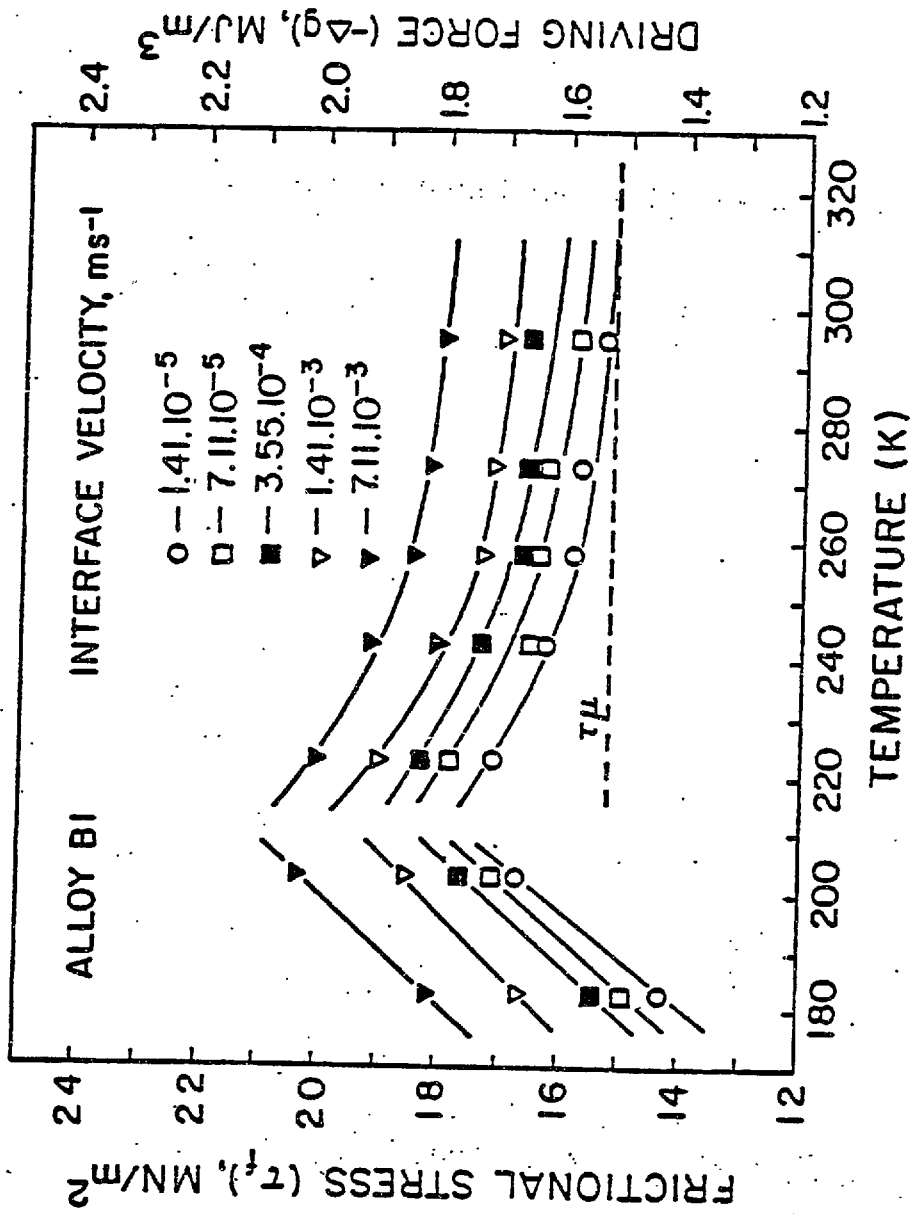


Figure 5 Temperature and velocity dependence of friction stress ( driving force) for alloy B1.

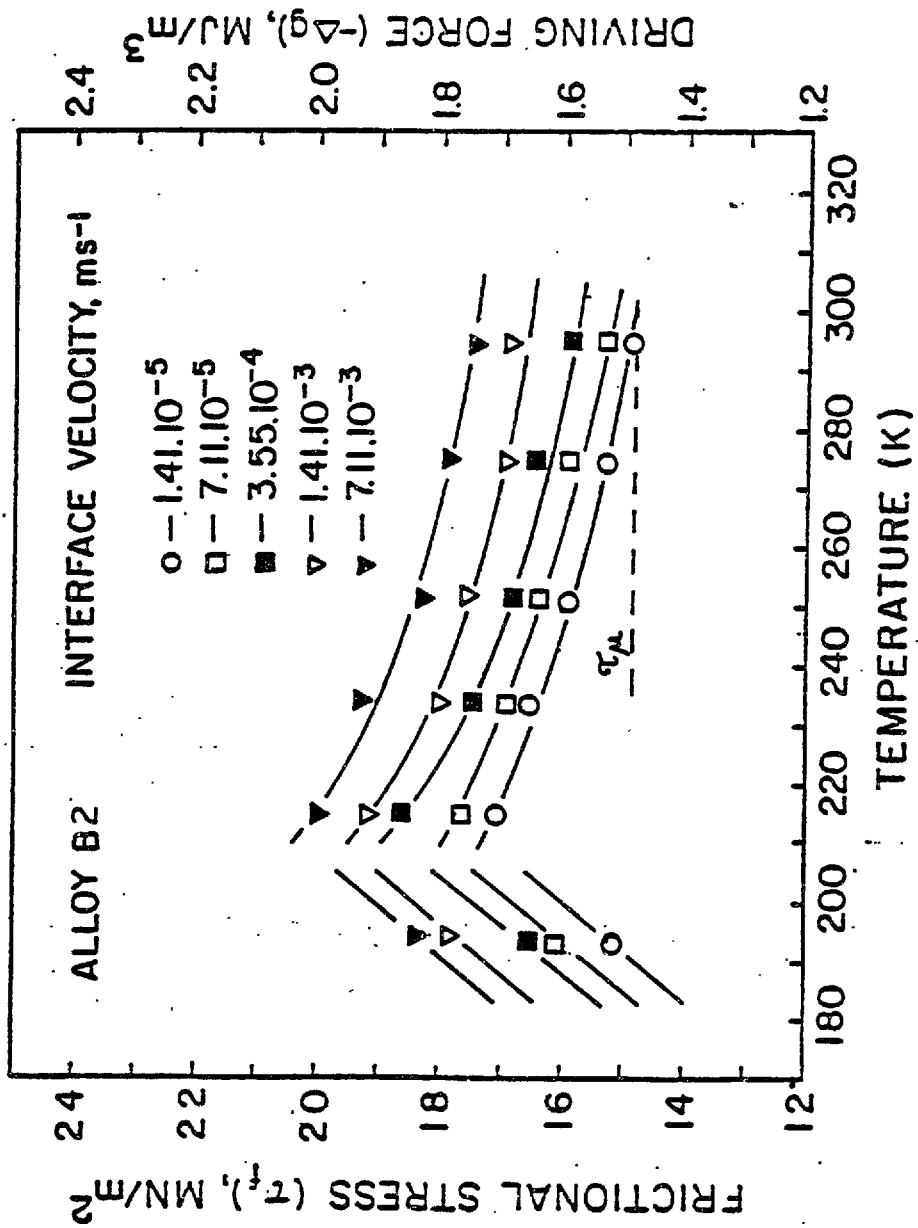


Figure 6 Temperature and velocity dependence of friction stress ( driving force) for alloy B2.

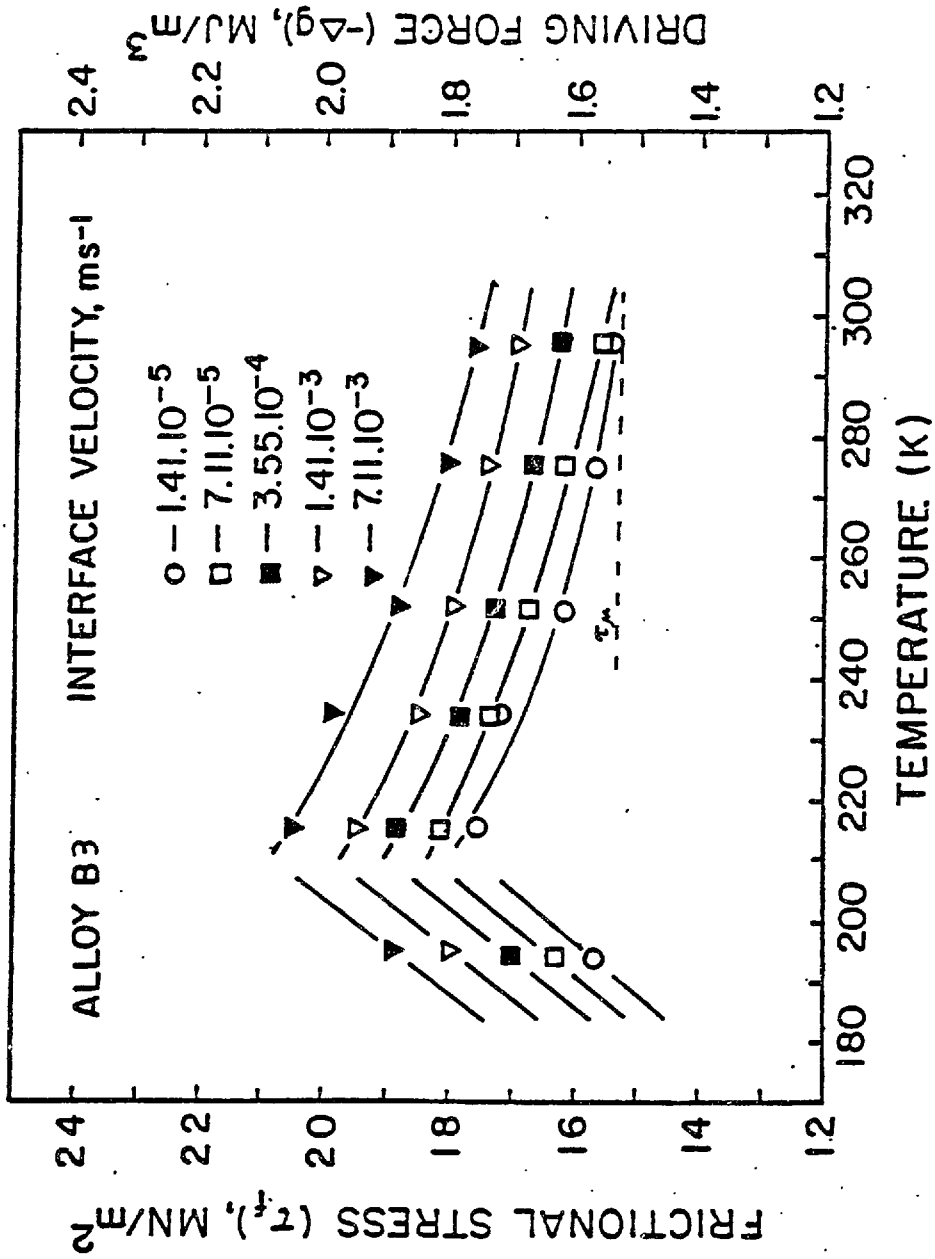


Figure 7 Temperature and velocity dependence of friction stress ( driving force ) for alloy B3.

## 5.2. Thermal Effect of the Single-Interface Stress-Induced $\beta_1 \rightarrow \gamma_1'$ Martensitic Transformation

Figure 8 gives the thermal effect associated with a single-interface stress-induced  $\beta_1 \rightarrow \gamma_1'$  martensitic transformation in Cu-Al-Ni alloys. An increment in temperature measured by two thermocouples T/C #1 and T/C #2 was plotted against position of the moving interface with respect to the end of the specimen where nucleation of a single variant of martensite occurred. Positions of the two thermocouples, T/C #1 at 5mm and T/C #2 at 9.5 mm, were also referred to the same end of the specimen. The thermal effect of the transformation was measured for the entire range of the interface velocities employed.

According to Figure 8, the thermal effect associated with the highest interface velocity,  $7.11 \cdot 10^{-3} \text{ms}^{-1}$ , was as high as 7 degrees. This indicates that isothermal conditions adopted throughout this work could be significantly disturbed. Fortunately, interface velocity next to the highest produces a much smaller thermal effect,  $\sim 2.5$  degrees. Thermal effects associated with lower interface velocities are even smaller i.e., under 0.5 degree. Compression test data referring to the highest interface velocity were, therefore, ignored in order to maintain the assumption that the interface motion took place under isothermal conditions.

Heat transfer for a single-interface martensitic transformation has been analyzed in Appendix A. It was shown that a simple model could account for the measured thermal effect and recorded temperature distribution presented in this section.

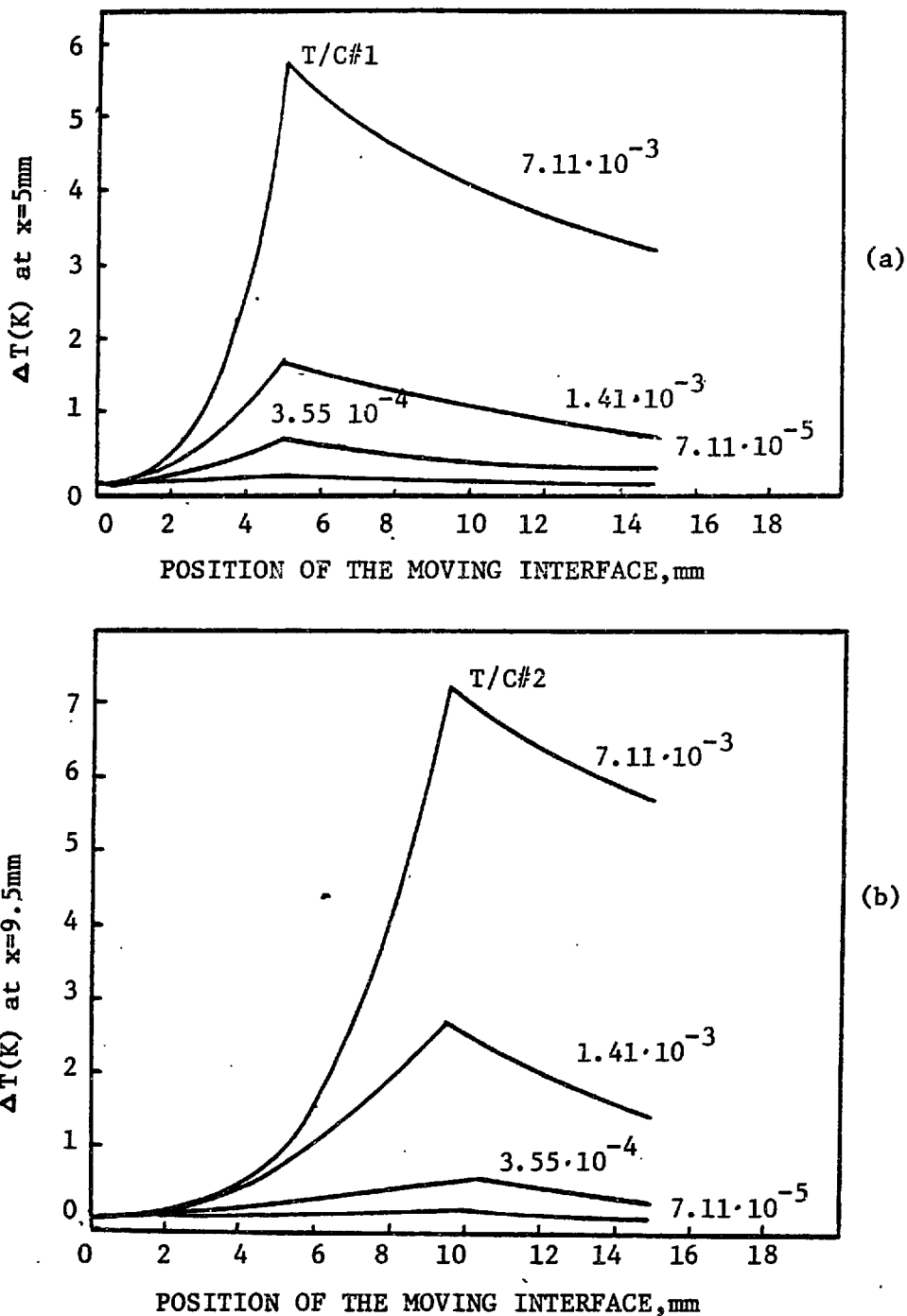


Figure 8 The thermal effect,  $\Delta T(K)$ , due to single-interface stress-induced  $\beta_1 \rightarrow \gamma_1'$  martensitic transformation recorded by two thermocouples located at two different positions along the specimen: (a) T/C#1,  $x=5\text{mm}$ ; (b) T/C#2,  $x=9.5\text{mm}$ . Position of the moving interface as well as the location of the thermocouples are specified with respect to the end of the specimen where nucleation of the single-martensitic variant occurred. The numbers on the plots give the interface velocity in m/s.



### 5.3. Elastic Constants

The use of  $\langle 110 \rangle_{\beta_1}$  oriented single crystals allowed the following elastic constants to be measured:

$$C_L = (C_{11} + C_{12} + 2C_{44})/2, \quad (16)$$

$$C = C_{44}, \text{ and} \quad (17)$$

$$C' = (C_{11} - C_{12})/2. \quad (18)$$

Thus,  $C_{11}$  and  $C_{12}$  as well as the anisotropy ratio of the two shear constants,  $A = C_{44}/C' = 2C_{44}/(C_{11} - C_{12})$ , could be calculated. The variation of these parameters with temperature for alloy B1 is plotted in Figure 9(a).

With respect to the stability of the bcc  $\beta$ -lattice, it is worthwhile to follow the variations of the quantities  $C_{44}$ ,  $B = (C_{11} + 2C_{12})/3$  and  $C_{11}^2 - C_{12}^2$ . Stability criteria for a cubic lattice requires all three quantities to be positive (78,79). Since the physical meaning of the quantity  $C_{11}^2 - C_{12}^2$  is not readily apparent, it is a common practice to follow the behavior of  $C'$  which is the resistance to a  $\{110\}\langle \bar{1}10 \rangle$  shear.  $C_{44}$  is the resistance to a shear deformation in a  $\langle 100 \rangle$  direction on any plane in the  $\langle 100 \rangle$  zone or the resistance to a shear deformation in any direction in a  $\{100\}$  plane and bulk modulus,  $B$ , is the resistance to a hydrostatic deformation. Variation of these stability quantities with temperature for alloy B1 is shown in Figure 9(b).

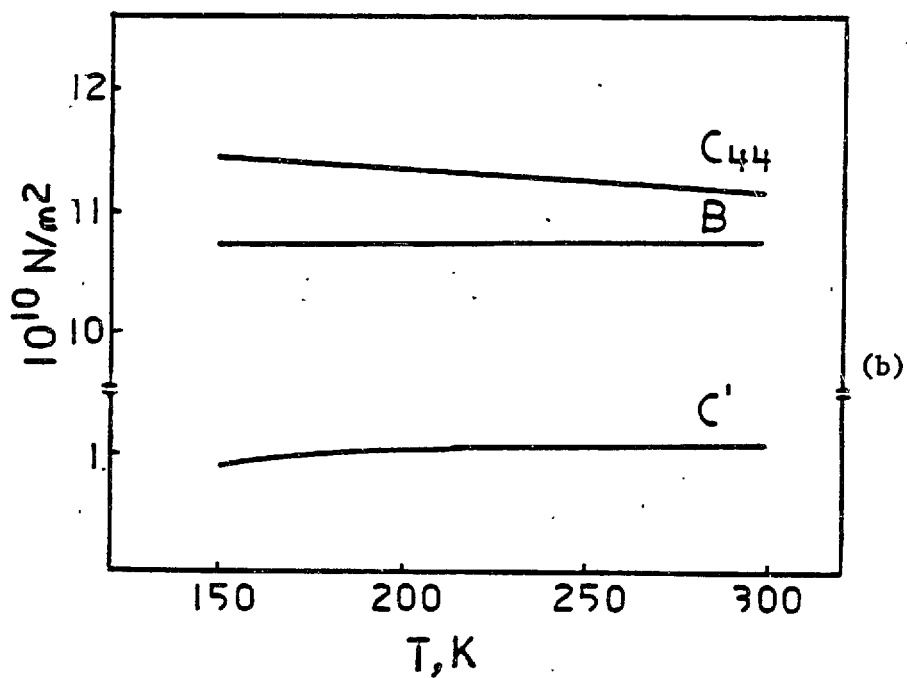
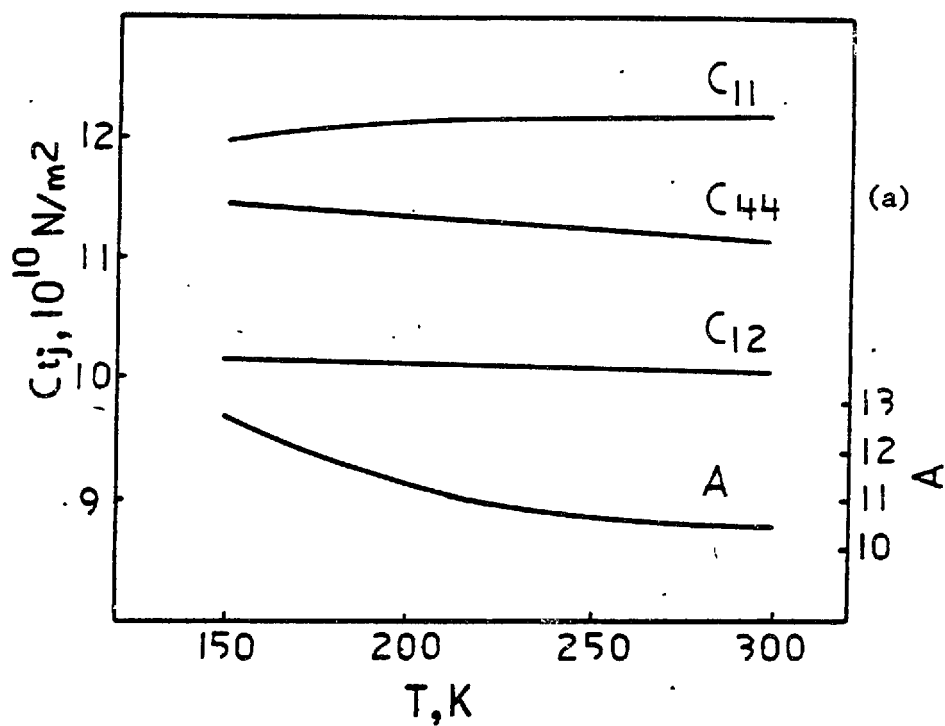


Figure 9. Temperature dependence of the elastic constants  $C_{11}$ ,  $C_{12}$  and  $C_{44}$  and of the anisotropy ratio,  $A$ , (a) and of the bulk modulus,  $B$ , and two shear elastic constants  $C'$  and  $C_{44}$ , (b) for alloy B1.

As discussed by Nagasawa et al. (79), a better insight into the mechanical stability of a lattice can be obtained by constructing velocity surfaces of elastic waves. The three kinds of velocity surfaces can be obtained by substituting elastic constants in the elastic wave equation. They are L,  $T_1$  and  $T_2$ . L and T refer to longitudinal and transverse types of waves, respectively. From the mechanical stability point of view, extremum points on velocity surfaces are of particular interest.

For a cubic crystal, the Christoffel equation (80,81) can be used to get different planar sections of the velocity surfaces. Figure 10 shows the polar plots of the  $T_2$  velocity surface sections in the  $(001)_\beta$  and  $(\bar{1}10)_\beta$  planes. The effective shear constant in a direction  $\vec{K}$  on these planes is measured by the magnitude of the radius vector from the origin to the velocity surface along  $\vec{K}$ . The local minimum on the  $(001)$  section of the  $T_2$  velocity surface, (Figure 10(a)), corresponds to a  $(110) \langle \bar{1}10 \rangle$  shear with the resistance measured by  $C'$ . A second minimum exists in the velocity surface in the  $(\bar{1}10)$  plane, Figure 10(b), with  $\vec{K}$  about  $40.5^\circ$  from  $[001]$ . It is this local minimum which Nagasawa and Ueda (82) named the "special mode". An effective elastic constant along  $\vec{K} = [112]$ , in Figure 10(b), corresponds to a  $\{112\} \langle \bar{1}1\bar{1} \rangle$  b.c.c. twinning shear. This elastic constant is very close to the minimum associated with the special mode.

Some general findings concerning the temperature dependence of the elastic constants and stability quantities, drawn on the basis of Figures 9 and 10, can now be summarized:

- Three basic elastic constants,  $C_{11}$ ,  $C_{12}$ , and  $C_{44}$ , show a weak

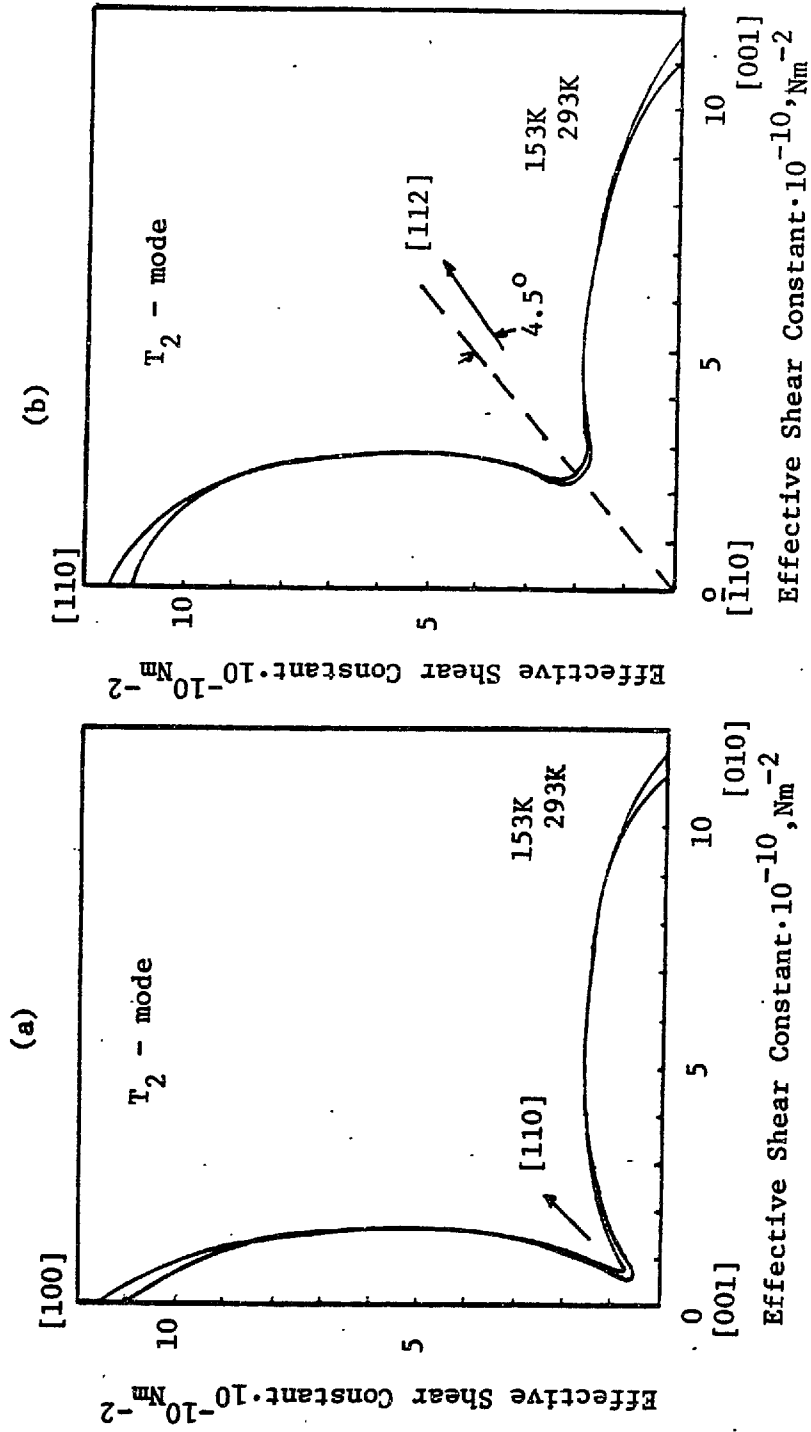


Figure 10 Polar plots of  $T_2$ -mode shear constants with: (a) wave vector  $\vec{k}_\perp$  [001] and polarization vector  $\vec{\epsilon}_\perp$  [110]; and (b)  $\vec{k}_\perp$  [112],  $\vec{\epsilon}_\perp$  [110] for the alloy. Bl.

temperature dependence, their relative change being less than  $\pm 0.3\%$ ;

- The anisotropy ratio, as in other noble-metal base alloys (83-90), is fairly high and increases with decreasing temperature;
- All the stability quantities,  $B$ ,  $C_{44}$ , and  $C'$ , are positive, suggesting a stable structure of the matrix  $\beta_1$ -phase. However,  $C'$  is quite soft and also shows an anomalous positive temperature dependence, indicating a low lattice resistance to a  $\{110\}\langle\bar{1}10\rangle$  shear. Similar behavior of  $C'$  in the subambient temperature range has already been reported for similar  $\beta$ -alloys (83-90).
- The lattice resistance to a  $\{112\}\langle\bar{1}1\bar{1}\rangle$  shear is also relatively small, yet approximately three times as large as  $C'$ .

Elastic constants of the alloys A, B2, and B3 were determined at room temperature and results are summarized in Table 2.

TABLE 2. ELASTIC CONSTANTS (IN  $10^{10}$  N/m<sup>2</sup>) AND ANISOTROPY RATIO AT ROOM TEMPERATURE

Alloy	$C_{11}$	$C_{12}$	$C_{44}$	$C'$	$B$	$\mu^{*1}$	$A$
A	13.30	9.80	16.62	1.75	10.97	7.22	9.5
B1	12.20	10.05	11.15	1.08	10.74	4.74	10.5
B2	12.20	10.10	10.90	1.05	10.80	4.63	10.4
B3	12.25	10.20	10.90	1.03	10.88	4.60	10.6

\*1.  $\mu$  - effective isotropic shear modulus

Throughout this work, only the isotropic elasticity approach was used, which employs elastic moduli rather than elastic constants. Several different averaging techniques have been proposed in the literature (91-94) for calculation of the isotropic shear elastic modulus from the elastic constants. Hill's procedure (94) seems to give the best average and was employed here. Calculated values of the shear elastic modulus,  $\mu$ , are given in Table 2. Based on the temperature dependence of elastic constants of alloy B1,  $\mu$  can be taken as independent of temperature.

#### 5.4. Data Analysis

The single-interface mobility data, presented in Section 5.1, will now be analyzed in terms of the theory of thermally-activated deformation (48), which was briefly outlined in Section 2.2.3. Only a temperature range above  $\sim 210\text{K}$ , associated with the negative temperature dependence of the friction stress, is treated here. The anomalous behavior at temperatures below  $\sim 210\text{K}$  is not analyzed in this section, since it is apparently inconsistent with the theory of thermally-activated deformation. It was shown in Section 5.1 that the friction stress (and the volume driving force) has two components: a thermal component and an athermal component. Only the thermal component of the friction stress (and of the volume driving force) enters the activation analysis employed here.

Validity of the velocity law, described by equation (6) was confirmed by replotting the mobility data, Figures 4 through 7, into corresponding  $\ln v$  vs.  $1/kT$  plots. According to the data analysis procedure, described

in Section 2.2.3, a linear relation between  $\ln v$  and  $1/kT$ , at constant stress, which was found here, validates the proposed velocity law. Furthermore, the operational activation energy,  $Q$ , becomes equal to the model activation enthalpy,  $\Delta H$ . The model activation entropy,  $\Delta S$ , is predominantly of vibrational character (48) and thus depends on the temperature variation of elastic moduli. It was shown in Section 5.3 that the elastic constants, and therefore the elastic moduli, are very weak functions of temperature. This means that the activation entropy has a very low magnitude, and that its contribution to the model activation energy,  $\Delta G$ , when compared with the activation enthalpy, is negligible. Consequently, the model activation energy,  $\Delta G$ , can be successfully approximated with the operational activation energy,  $Q$ . The plots of  $\ln v$  vs.  $1/kT$  along with equation (9) enabled a determination of the activation energy and its stress dependence, as shown in Figure 11. Data for all A and B alloys, over the temperature range investigated, are in reasonable agreement, suggestive of a common rate controlling mechanism. The standard deviation for the activation energy, averaged over a number of values of the friction stress, is estimated to be  $3.2 \cdot 10^{-21} \text{ J}$  (0.02 eV). According to the theory of thermally-activated deformation, plots of the activation energy versus stress can often be described as:

$$\Delta G = F_0 \left[ 1 - \left( \frac{\tau_f}{\tau} \right)^p \right]^q \quad (19)$$

where:  $F_0$  - total activation energy corresponding to the zero applied stress,  $p, q$  - coefficients which taken on characteristic values for different mechanisms of dislocation motion.

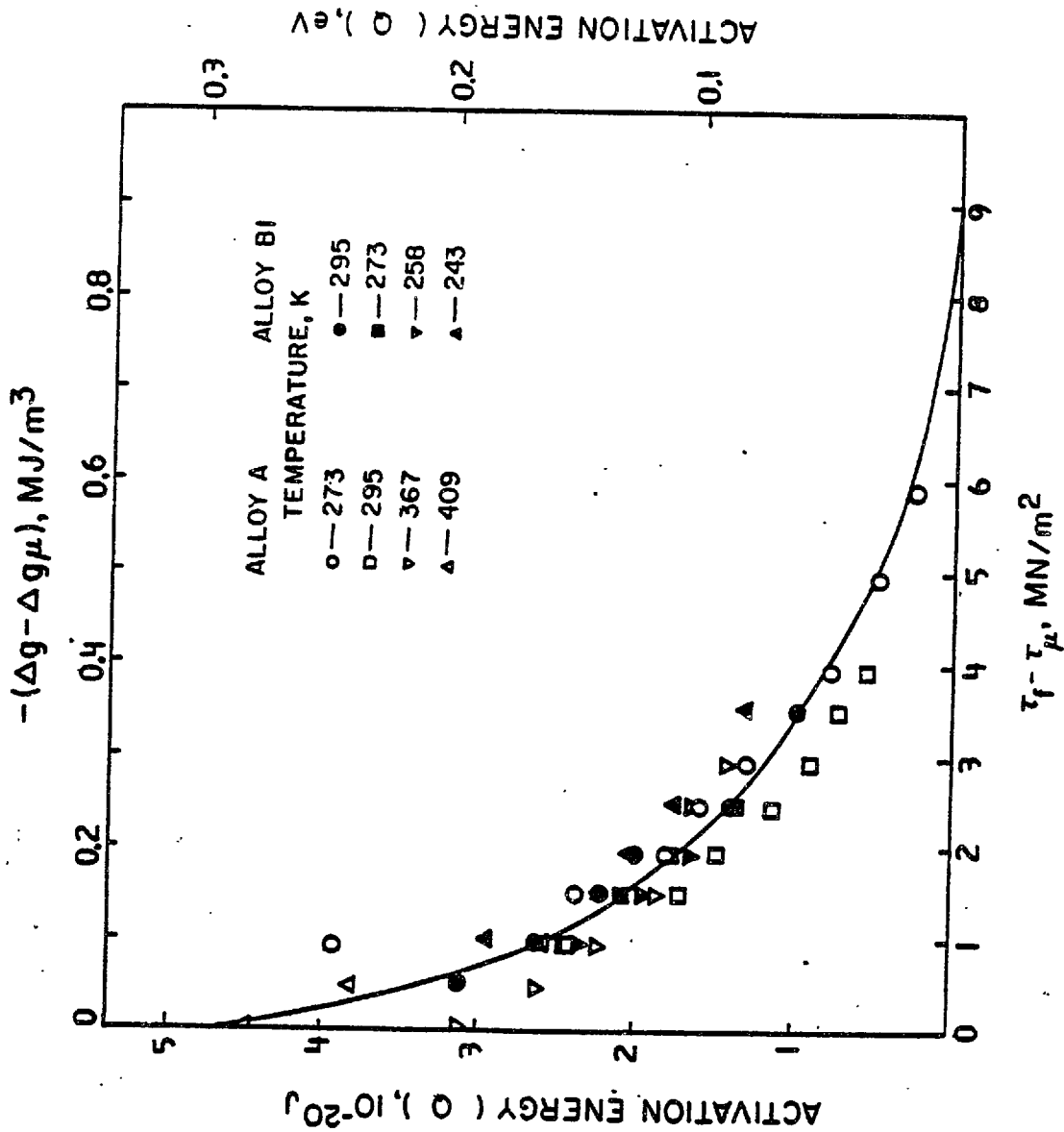


Figure 11 Activation energy vs. friction stress (driving force) for alloys A and B1.



Adopting this type of relation, the data shown in Figure 11 are best fitted by a curve,  $\Delta G(\text{eV}) = 0.305[1 - (\tau(\text{MN}/\text{m}^2/9)^{0.39}]^{1.35}$ . Values of the coefficients  $p = 0.39$  and  $q = 1.35$  correspond, in the theory of thermally-activated slip, to a rate control by modulus and/or strain interaction between slip dislocations and discrete particles.

Using the plots of  $\ln v$  vs.  $1/kT$ , it was found that the pre-exponential term,  $v_0$ , lies in a range of 10 to 40 m/s. However, it could not be concluded that the  $v_0$  is a particular function of stress. According to equation (13), if the preexponential term is stress invariant, then the operational activation area (volume) and the apparent activation area (volume) become equal to each other. This simplifies the calculation procedure of the apparent activation area and corresponding stress activation volume and equations (10) and (11) can be invoked. However, a word of caution should be drawn at this point to some significant differences between lattice- and interface-dislocations. The critical event for the thermally-activated motion of a line dislocation is two-dimensional in character. Since the Burgers vector of the lattice dislocation is close to the slip plane spacing, a product of the activation area and the Burgers vector indeed defines a volume of the critical configuration. Discrete dislocation models for the structure of coherent interfaces (including the local structure of the twinned semicoherent interfaces dealt with here) describe the interface in terms of transformation or coherency partial dislocations which propagate the local transformation lattice deformation. When the coherency dislocations in

a particular array are relatively widely spaced, it is expected that the interaction of the individual coherency dislocations with a given obstacle involves an activation area,  $a^*$ , similar to that for the case of slip dislocations. Yet,  $ba^*$  in this case may considerably underestimate the activation volume of the critical configuration since the Burgers vector of the coherency dislocation is a small fraction of the lattice parameter. Furthermore, if the coherency dislocations are closely spaced, the interface will behave as a quasi-continuous distribution of dislocations or a "surface dislocation". Then, when interacting with an obstacle, the critical event is more three-dimensional in character (95). Accordingly, it is useful to introduce a new definition of the "activation volume",  $V^*$ , as the derivative of activation energy with respect to volume driving force.

$$V^* = \left. \frac{\partial Q}{\partial \Delta g} \right|_T \quad (20)$$

If we regard the local strain,  $\gamma$ , accompanying the motion of line dislocations as,  $\gamma = b/d$ , with  $d$  the interplanar spacing, then the local driving force is  $\Delta g = -\tau\gamma = -\tau b/d$ . The activation volume associated with an activation area,  $a^*$  is  $V^* = da^*$ , which corresponds to the volume of the critical configuration. Hence,  $V^*$  can conveniently be used to describe the behavior of both line and surface dislocations allowing direct comparison of the interaction of each with a given obstacle. An added benefit of the use of a volume driving force formulation for thermally-activated interfacial motion is that  $\Delta g$  can be used to describe response

to chemical forces as well as mechanical forces. For chemical forces, such as those operative in the spontaneous martensitic transformation on cooling, a tensor quantity corresponding to  $\tau$  does not exist.

Analogous to equation (10), "operational activation volume", can be defined as:

$$V'' = -kT \left( \frac{\partial \ln v}{\partial \Delta g} \right)_T \quad (21)$$

Using this relation to evaluate  $V^*$  from the experimental data, the variation of  $\Delta g$  with  $V^*$  (and  $\tau$  with  $V_T$ ) for all A and B alloys above 210K, corrected for the athermal contributions, is shown in Figure 12. Activation volumes are expressed in terms of the atomic volumes  $\Omega$ . Again, data for all alloys over the temperature range investigated are in reasonable agreement, indicating a single rate controlling mechanism. A long range "tail" of the obstacle profile in Figure 12 is consistent with the coefficient  $p = 0.39$ . Details of the short range (low  $V^*$ ) behavior could not be discerned due to the intervention of the anomalous effect at low temperatures.

The overall profile shape and large activation volumes of  $10^3$  to  $10^4 \Omega$  are similar to those for discrete particles such as fine precipitates or solute clusters, possibly with a distribution of sizes. Transmission electron microscopy should help identify these rate controlling obstacles to the interface motion.

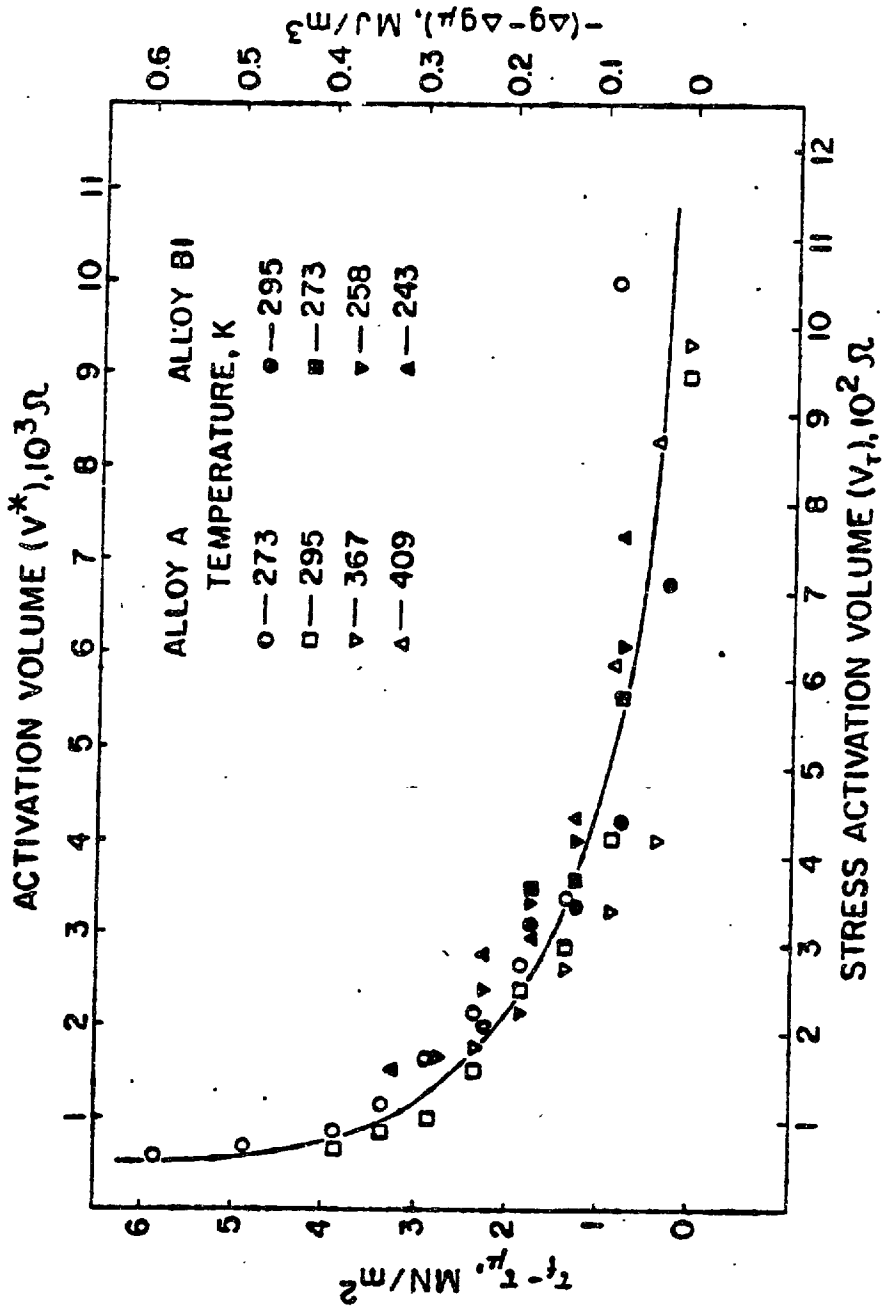


Figure 12 Thermal component of friction stress ( driving force ) vs. activation volume for alloys A and B1.

## 5.5. Transmission Electron Microscopy

### 5.5.1. Introduction

The heat treatments described in Section 4.1, which involved quenching from a high temperature single-phase region, were meant to provide a single metastable  $\beta$ -phase structure of the specimens at room temperature. It was known that a  $\beta(\text{b.c.c.}) \rightarrow \beta_1(\text{DO}_3)$  ordering reaction could not be suppressed (96) but the heat treatments employed should have prevented decomposition of the  $\beta_1$ -phase. However, transmission electron microscopy (TEM) has revealed that a variety of precipitates were formed. Some of these precipitates could be removed by raising the solution temperature (alloy B2) or by increasing the quenching rate (alloy B3). However, formation of the second phases could not be suppressed completely. Once this was realized, an effort was made to understand and characterize the structure and morphology of the precipitates.

### 5.5.2. Dislocations in the metastable $\beta_1$ -phase

A bright-field electron micrograph of alloy B1 for a foil orientation  $\sim[001]_{\beta_1}$  is shown in Figure 13. Besides a second phase (to be discussed in the next section), a dislocation structure is observed. Two types of dislocations can be recognized. Many dislocations appear as single lines, straight or stepped, running in  $[100]_{\beta_1}$  and  $[010]_{\beta_1}$  directions. Some of them look more curved but a close examination reveals that they have a fine  $\langle 100 \rangle_{\beta_1}$  step structure. The image width of these dislocations varies from  $\sim 10$  to  $20\text{nm}$ . A second type of dislocation occurs always in pairs of parallel dislocations with a separation  $\sim 20\text{nm}$ . These also run in

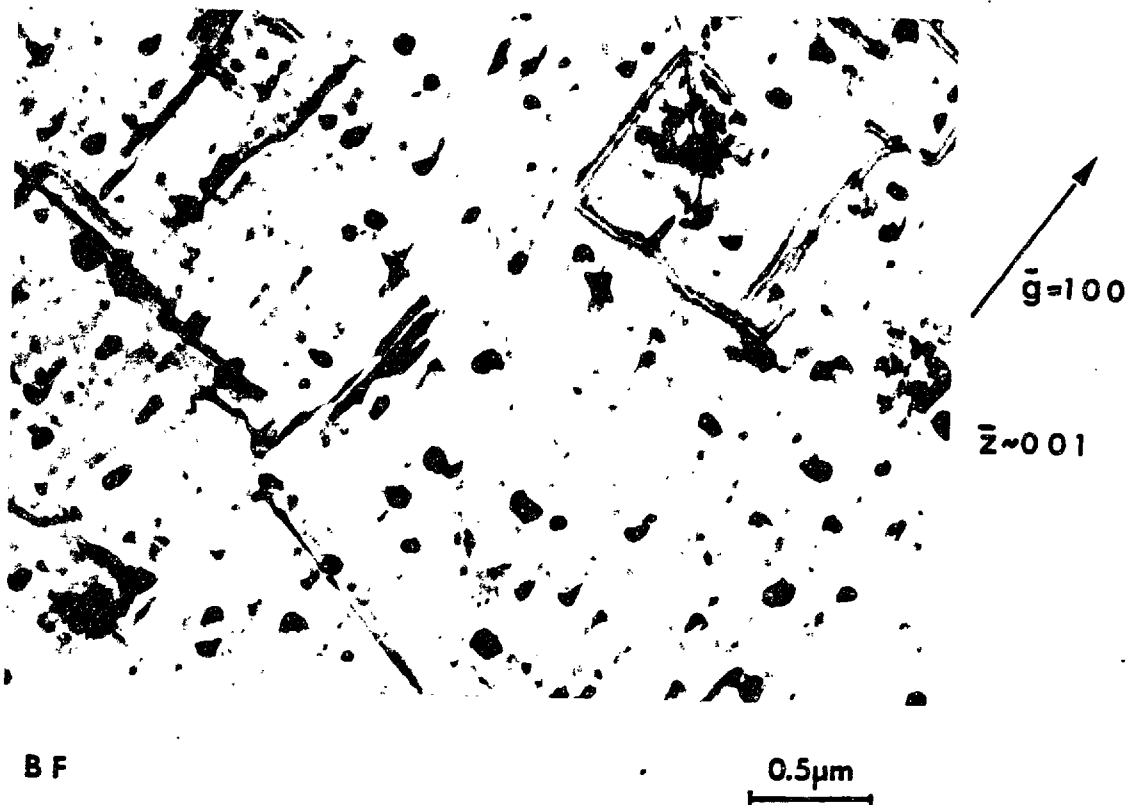


Figure 13 Bright-field image of the alloy B1 showing a typical dislocation structure observed.

$\langle 100 \rangle_{\beta_1}$  directions and often have a quite coarse  $\langle 100 \rangle_{\beta_1}$  step structure.

It should be noticed that these two apparently different types of dislocations often appear to react generating common nodes. Furthermore, wide single dislocations are sometimes revealed to be unresolved dislocation pairs. Thus, it seems probable all the dislocations are paired but some pairs cannot be resolved by the TEM technique used in this study.

The dislocation density was estimated to be  $\sim 10^{12}$  lines/m<sup>2</sup>. Stressing the specimens after quenching did not affect noticeably the dislocation density. This is consistent with theories of thermoelastic martensitic transformations (37,97,98) which postulate an elastic accommodation of the martensitic transformation shape change.

It was observed, furthermore, that the dislocation structure, in both character and density, was insensitive to changes in the heat treatment and in the alloy composition.

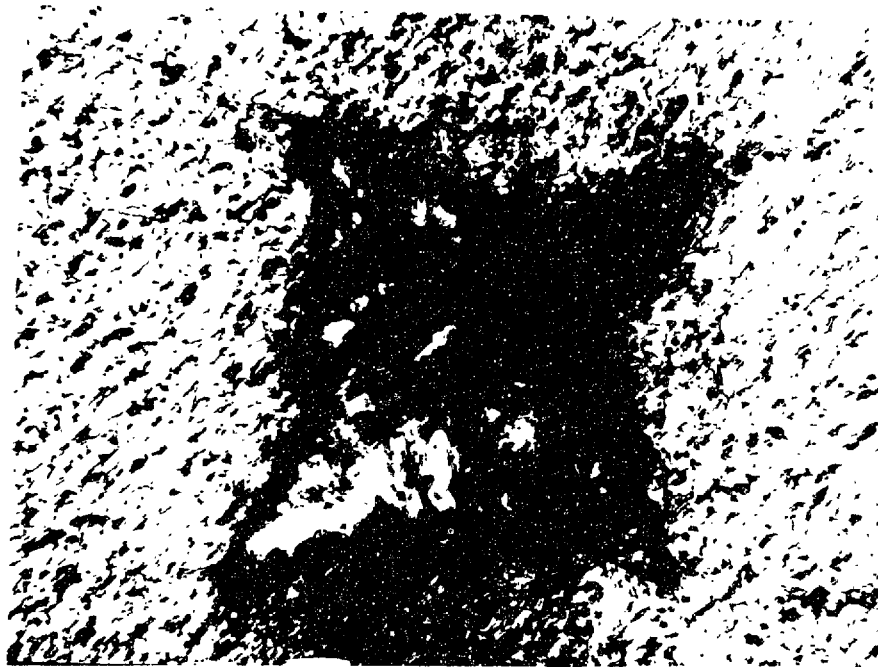
### 5.5.3. $\gamma$ -phase precipitation

Figure 14 shows coarse-scale precipitation which occurred only in alloys A and B1 solution treated at relatively low temperatures. The precipitates are distributed uniformly and their shape can be described as cuboidal elongated in diagonal directions. Their size, expressed in terms of the cube edge length, ranges from 0.5 - 2.5  $\mu\text{m}$ . These precipitates were also seen under an optical microscope. Using a point-grid technique (99), the average planar precipitate spacing, averaged over a few optical micrographs, was estimated to be 9.5  $\mu\text{m}$ .

Selected area diffraction (SAD) was employed to determine the structure of these precipitates. Figure 15 compares  $[001]_{\beta_1}$  -zone

Figure 14 Bright-field images of the alloy B1 showing a coarse  
-scale  $\gamma$ -phase precipitation : Two different thin-  
foil orientations were used: (a)  $z^{\sim}110$  and (b)  $z^{\sim}001$ .





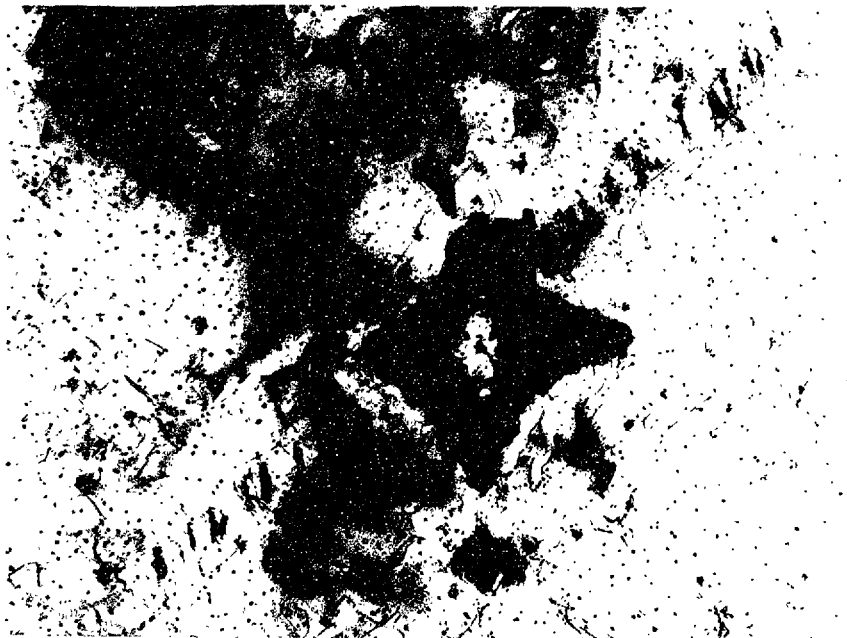
$\bar{g} = \bar{1}10$

$\bar{z} \sim 110$

BF

(a)

1.0 $\mu$ m



$\bar{g} = \bar{1}10$

$\bar{z} \sim 001$

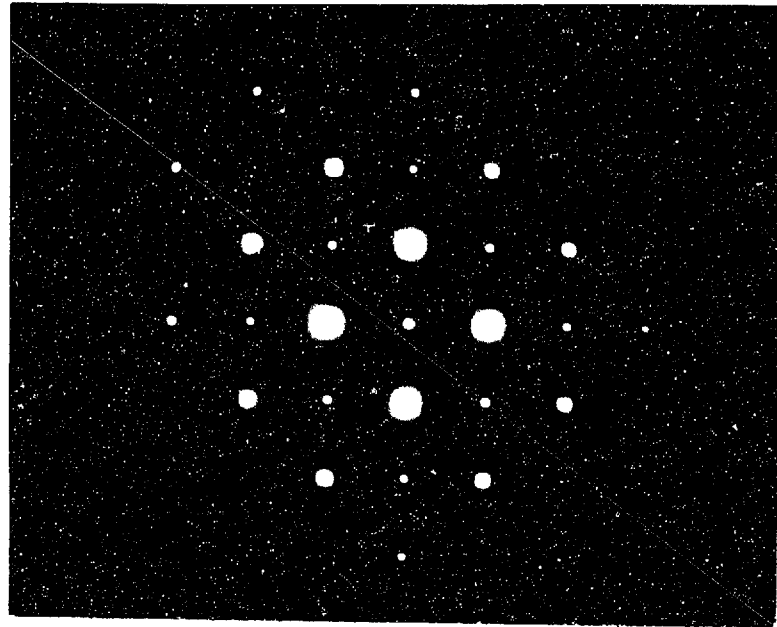
BF

(b)

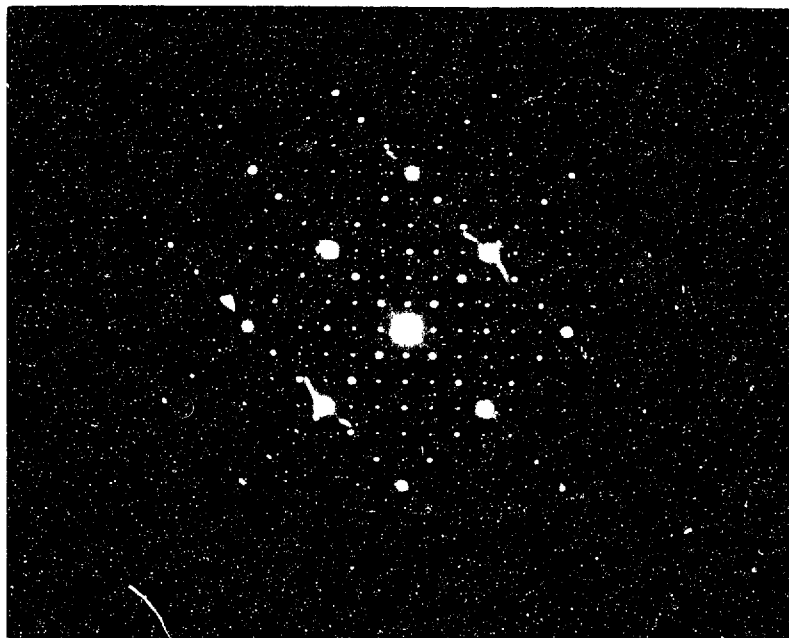
2.0 $\mu$ m

Fig. 14

Figure 15 The  $[001]_{\beta_1}$  electron diffraction pattern of the alloy B1 corresponding to: (a) the parent phase and (b) coarse-scale  $\gamma$ -phase precipitate.

 $\vec{g}=100$  $\vec{z}\sim 001$ 

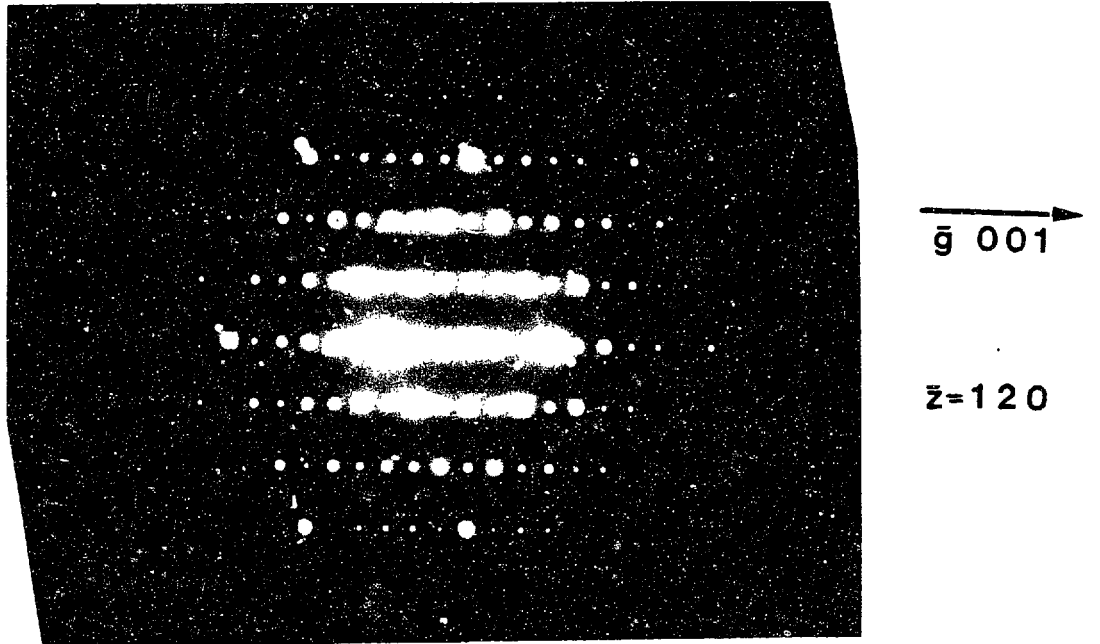
(a)

 $\vec{g}=100$  $\vec{z}\sim 001$ 

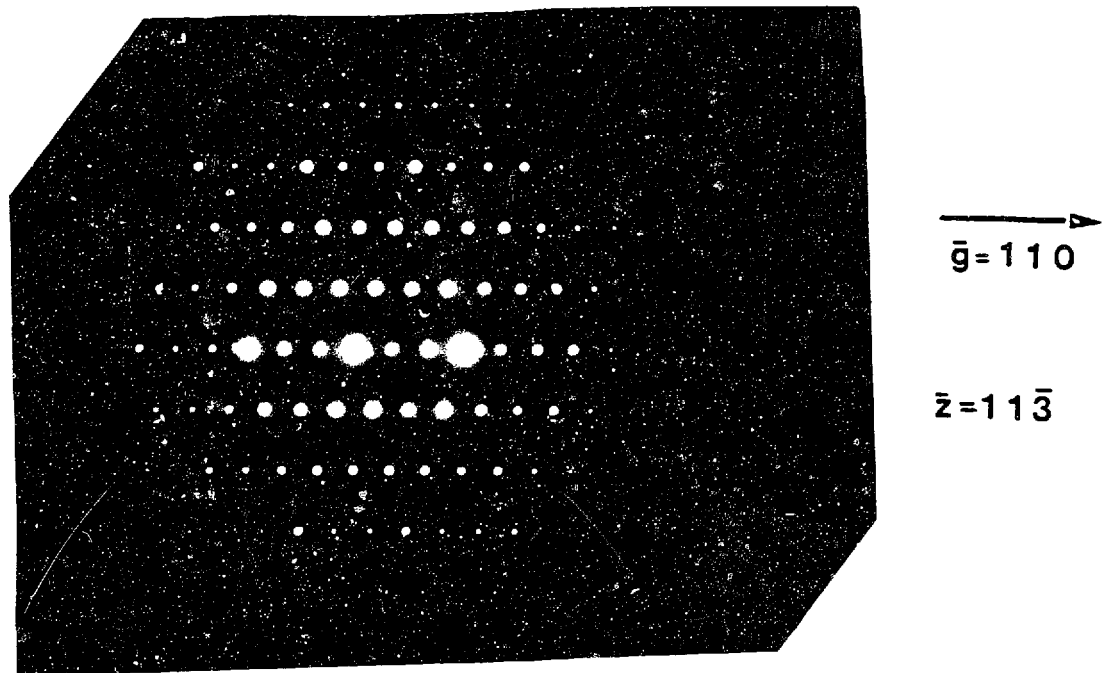
(b)

Fig. 15

Figure 16 Electron diffraction patterns associated with the coarse  $\gamma$ -precipitates in the alloy B1: (a)  $[120]_{\beta_1}$  and (b)  $[11\bar{3}]_{\beta_1}$ .



(a)



(b)

Fig.16

diffraction patterns outside and inside a coarse precipitate. As can be seen, the reciprocal lattice points associated with the precipitate divide distances between matrix points into thirds. The same conclusion holds for  $[120]_{\beta_1}$  and  $[11\bar{3}]_{\beta_1}$  zones, shown in Figure 16, where only SAD's inside a precipitate are presented.

These findings suggest that the coarse precipitates have a cubic structure coherent with the matrix and with a lattice parameter approximately three times as large as that of the matrix. All these conditions can be accounted for by a  $\gamma$ -structure, space group  $T_1^d$ , with a stoichiometric composition  $(\text{Cu,Ni})_9\text{Al}_4$  (100-102). Subsequently, it was confirmed by dispersive X-ray scattering technique microanalysis that precipitates, in fact, have a high aluminum content.

The presence of  $\gamma$ -precipitates was quite unexpected. The ternary Cu-Al-Ni phase diagram (103) indicates a single  $\beta$ -phase region at the solution temperatures used for alloys A and B1 (1073 and 1249K, respectively). However, when the solution temperature was raised to 1293K, no  $\gamma$ -precipitates were observed after quenching.

#### 5.5.4. 2H-type precipitates

Whereas a higher solution temperature eliminated the formation of  $\gamma$ -precipitates, another phase separation could not be suppressed completely. Precipitates other than coarse  $\gamma$ -phase particles, were observed in all four alloys (A, B1, B2, and B3).

Figure 17 shows a bright-field image of the alloy B2, with the foil orientation  $\sim[001]_{\beta_1}$  as demonstrated by the diffraction pattern

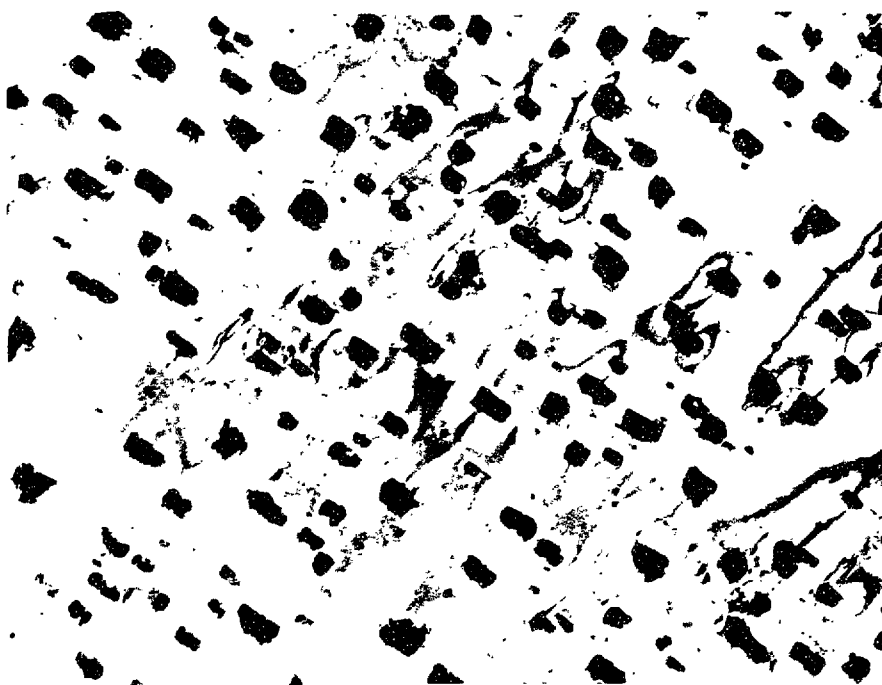
Figure 17 The  $\psi[001]_{\beta_1}$  electron diffraction pattern ,(a) ,  
corresponding to the bright-field image ,(b) , of  
the alloy B2.



$\bar{g} = 100$

$\bar{z} \sim 001$

(a)



B F

(b)

0.5 $\mu$ m

Fig. 17



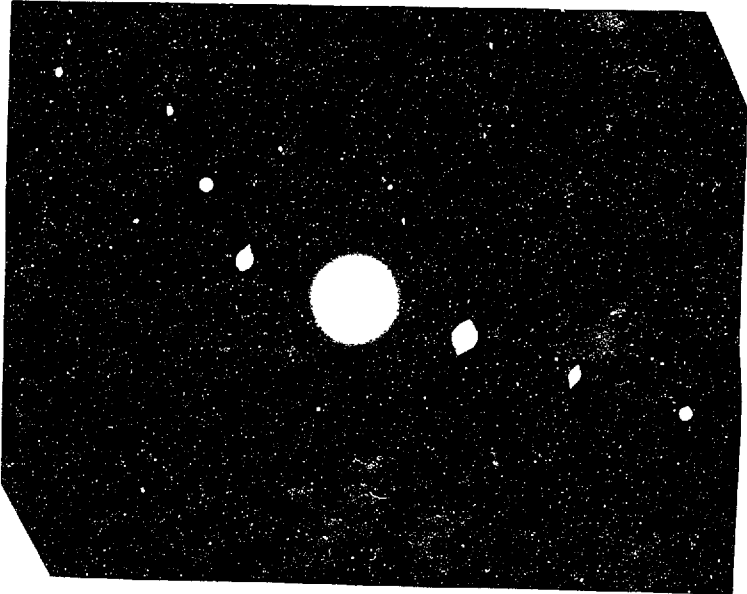
shown in the same figure. Evenly distributed precipitates of a rectangular shape appear to lie along  $[100]_{\beta_1}$  and  $[010]_{\beta_1}$  directions. On the other hand, the  $\sim[001]_{\beta_1}$  diffraction pattern contains, besides fundamental and superlattice matrix reflections, some extra reflections and streaking in  $[110]_{\beta_1}$  and  $[\bar{1}\bar{1}0]_{\beta_1}$  directions. Splitting of matrix reflections as well as satellites around them can be observed also.

Figure 18 shows a higher magnification bright-field image of the same area as Figure 17. The precipitates now seem to have a fine striated structure, with striations running in  $[110]_{\beta_1}$  and  $[\bar{1}\bar{1}0]_{\beta_1}$  directions. Furthermore, some additional fine precipitates are observed. The fringed structure of these precipitates is apparent. The fringes cluster around  $\langle 110 \rangle_{\beta_1}$  but do not lie exactly along these directions.

A dark-field image of the alloy B2 with the same foil-orientation,  $\sim[100]_{\beta_1}$ , is shown in Figure 19. An extra reflection, as shown by the diffraction pattern in Figure 19a, was used for the dark-field imaging. Most of the large striated precipitates and some of the fine ones light up. This is a strong indication that the extra reflection observed in the  $\sim[001]_{\beta_1}$  zone is associated with the precipitates. Furthermore, the fine precipitates appear to be of the same nature as the large ones, occurring probably in a variety of transformation variants.

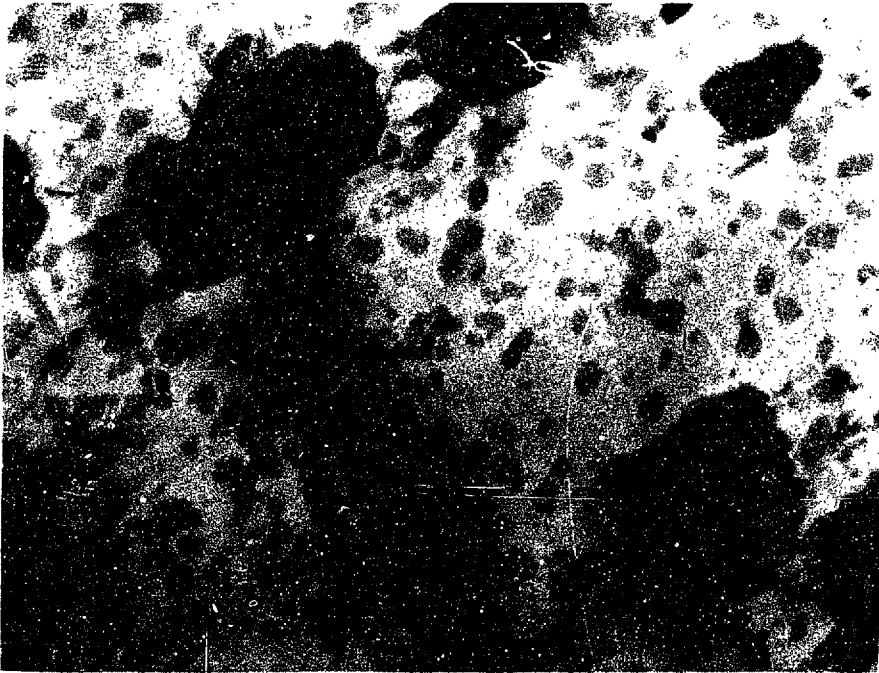
Figure 20 is a high magnification dark-field image of the same area as in Figure 19. Striations of both coarse and fine precipitates seem to lie in the  $[110]_{\beta_1}$  direction only. This suggests that the reflection used for the dark-field imaging originates from that particular variant of the precipitates.

Figure 18 The  $\sim[001]_{\beta_1}$  diffraction pattern, (a) , and the  
corresponding high-magnification bright-field image,  
(b), of the alloy B2.



$\vec{g} = 100$   
 $\vec{z} \sim 001$

(a)

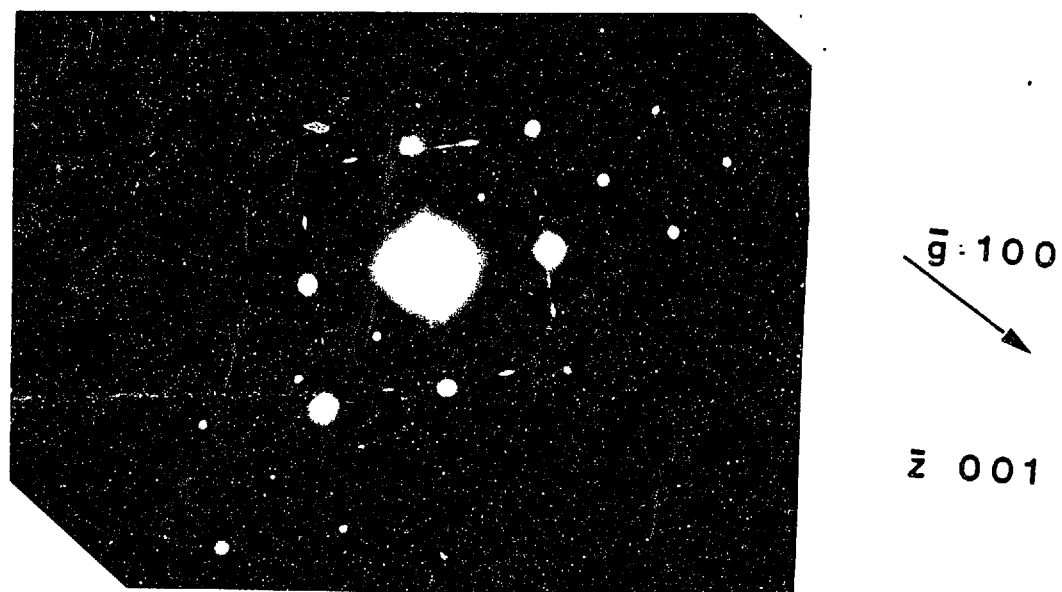


B F

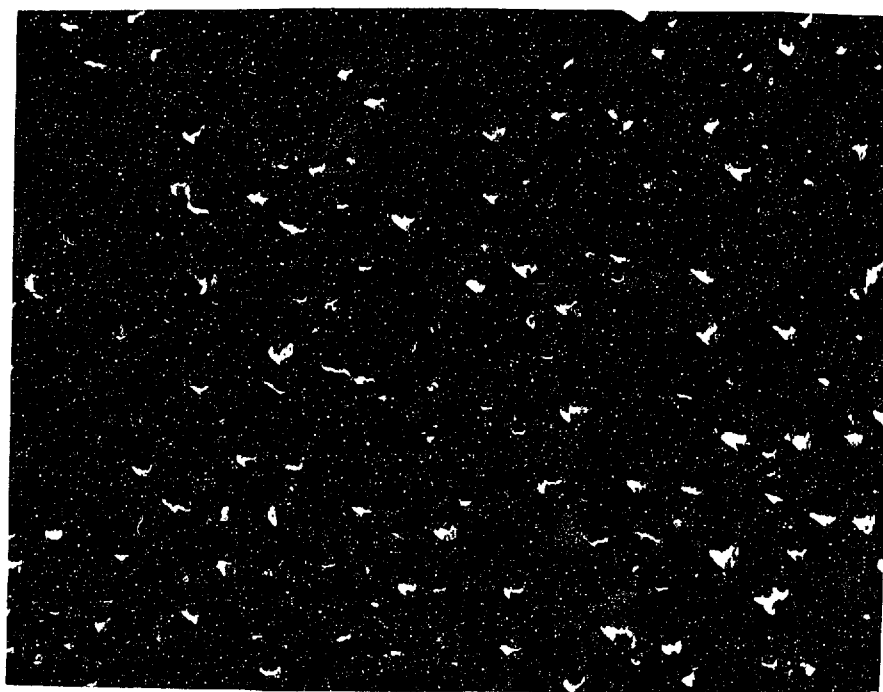
(b)  
Fig. 18

0.1 $\mu$ m

Figure 19 The  $\sim[001]_{\beta_1}$  diffraction pattern, (a) , and the corresponding dark-field micrograph, (b) , of the same area shown in Figure 17.



(a)



DF

(b)

Fig. 19

0.5  $\mu\text{m}$

Figure 20 The  $\nu[001]_{\beta_1}$  diffraction pattern, (a) , and the corresponding higher magnification dark-field image, (b), of the alloy B2.

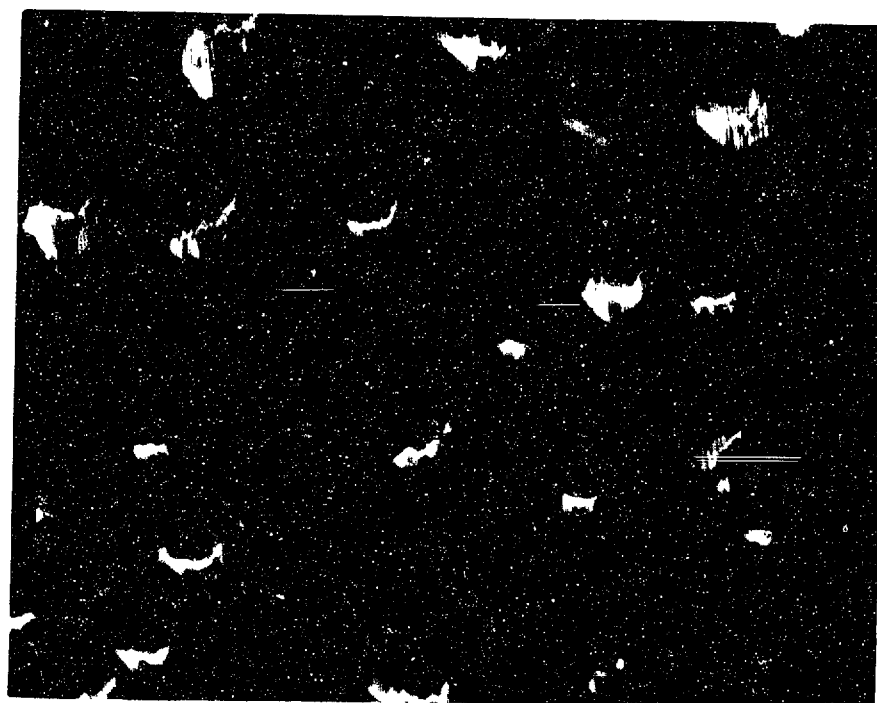
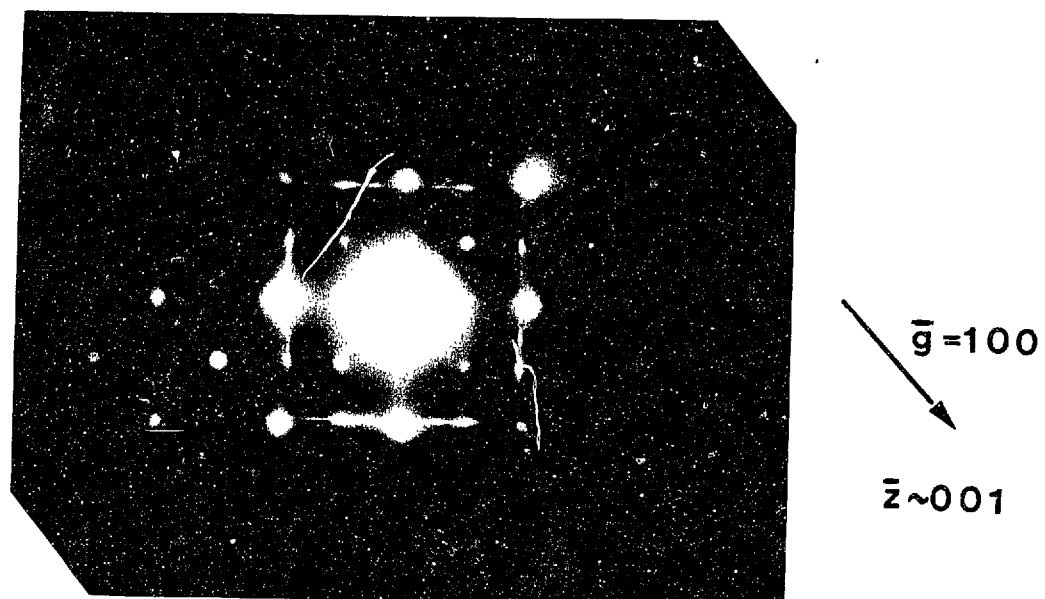


Fig. 20

A thin-foil with orientation  $\sim[0\bar{1}1]_{\beta_1}$  was used to produce the micrographs shown in Figures 21 and 22, which are bright and dark-field images of the alloy B2. Both coarse and fine precipitates are observed with striation along  $\sim[\bar{1}11]_{\beta_1}$  direction. Yet, the shape of the precipitates appears to be more irregular than of those shown in Figures 17 through 20. In the  $\sim[0\bar{1}1]_{\beta_1}$  zone, some extra diffraction spots can be seen.

According to Figures 17 through 22, precipitates appear to be present in two different sizes (more precisely, in two different distributions of sizes): The large particles are estimated to have a diameter between 100 and 150 nm and an average planar spacing (104) of 900 to 950 nm. The fine precipitates, on the other hand, have a diameter of 15 - 20 nm and an average planar spacing of 100 - 120 nm. Corrections have been made for particle image overlap and truncation (104).

In order to rationalize the nature of the large and fine precipitates, a systematic selected area diffraction investigation was conducted over a number of prominent diffraction zones of the  $\beta_1$ -phase. For this purpose, thin foils with different orientation were prepared to cover a tilting range of  $\sim 90^\circ$ .

An exact  $[001]_{\beta_1}$  zone is shown in Figure 23. Besides fundamental and superlattice matrix spots, some streaking in  $\langle 110 \rangle_{\beta_1}$  directions is observed. Some extra diffuse reflections situated along the streaks are also seen, but only far away from the central spot. This suggests that, due to buckling, a portion of the specimen had an orientation differing from an exact  $[001]_{\beta_1}$  zone.



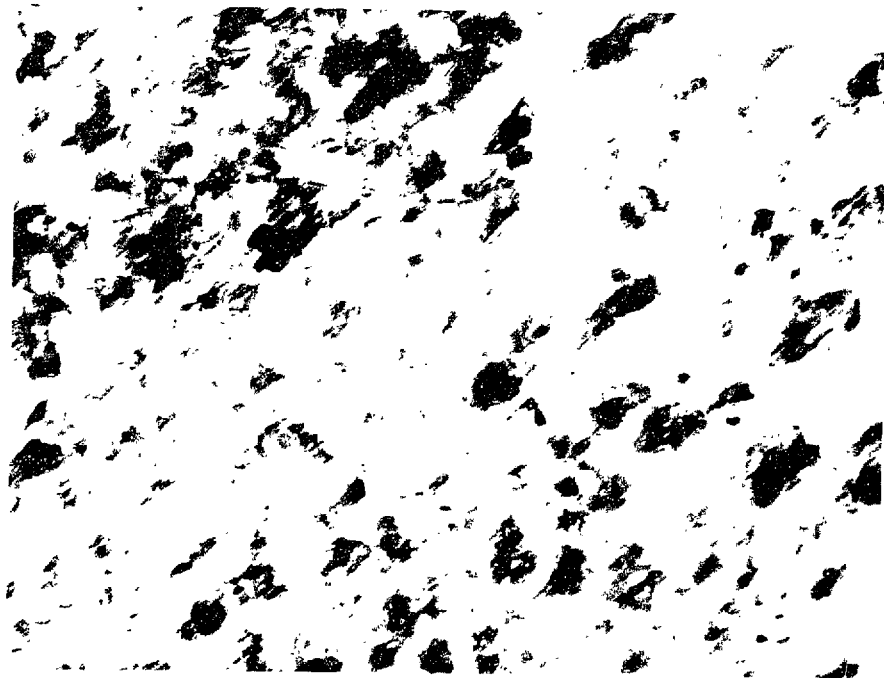
Figure 21 The  $\sim[0\bar{1}1]_{\beta_1}$  diffraction pattern, (a) , and the corresponding bright-field image, (b) ,of the alloy B2.



$\bar{g} = \bar{1}11$

$\bar{z} \sim 0\bar{1}1$

(a)



BF

(b)

0.5 $\mu$ m

Fig. 21

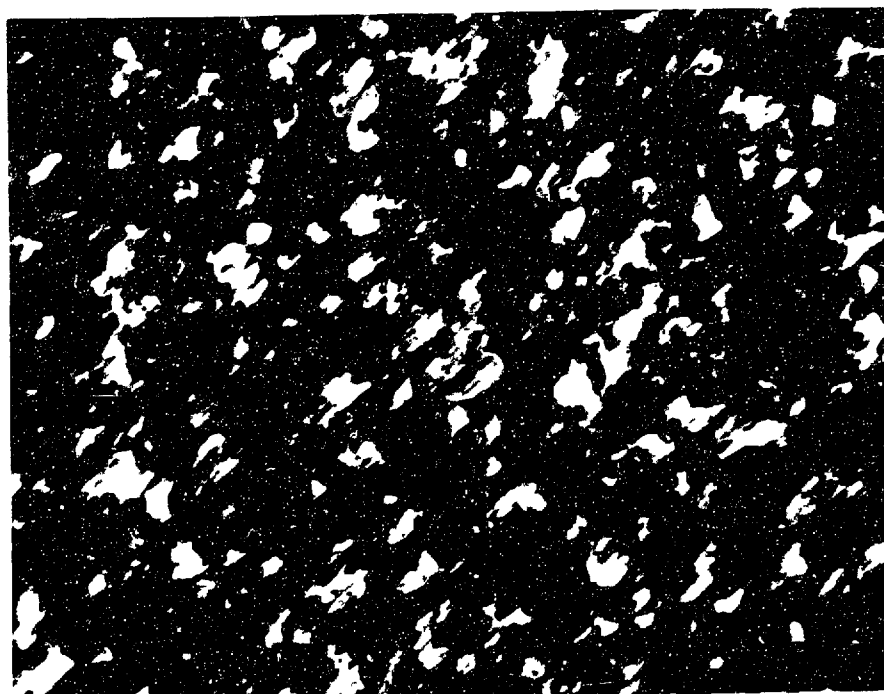
Figure 22 The  $\sim[0\bar{1}1]_{\beta_1}$  diffraction pattern, (a) , and the corresponding dark-field image, (b) , of the same area shown in figure 21.(b).



$\bar{g} = \bar{1}11$

$\bar{z} \sim 0\bar{1}1$

(a)



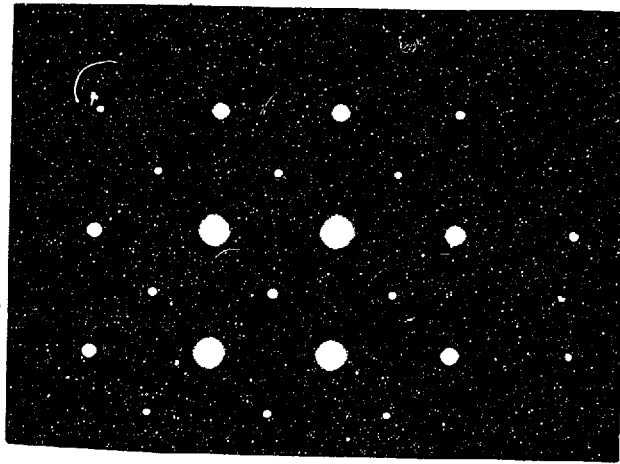
DF

(b)

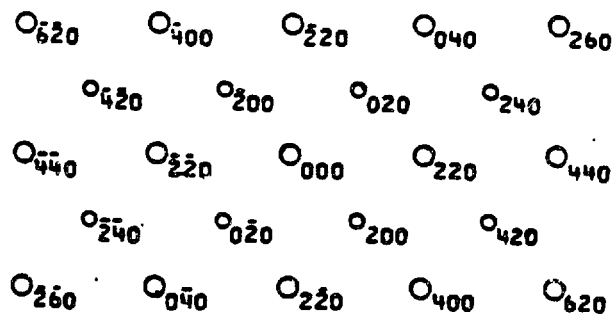
0.5 $\mu$ m

Fig. 22

Figure 23 The exact  $[001]_{\beta_1}$  diffraction pattern, (a) , in the alloy B2 and the corresponding index diagram, (b). See the text for the meaning of symbols in the index diagram.



(a)



[001]<sub>β</sub> ZONE

(b)

Fig. 23

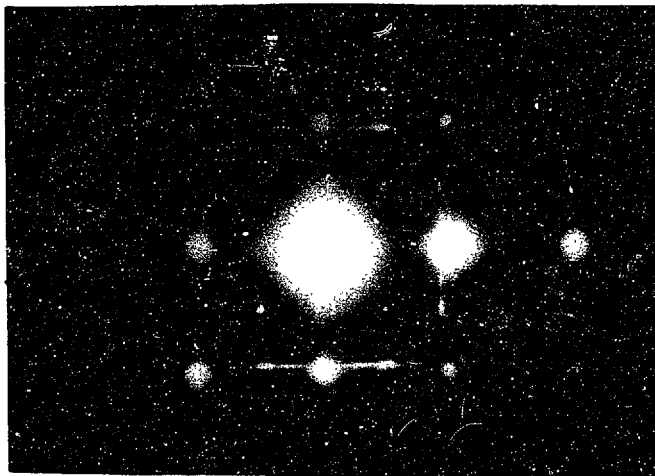
In order to interpret different diffraction features, use was made of index diagrams. These are shown in the same figure as the corresponding diffraction pattern, as in Figure 23. The following symbols were used in the index diagrams:

- Fundamental reflections of the  $\beta_1$ -matrix phase;
- ◉ Superlattice reflections of the  $\beta_1$ -matrix phase;
- ◻ Reflections of a 2H-type structure (to be discussed);
- ▲ Reflections of the other variant of a 2H-type structure;
- Reflections of the 2H-type phase which lie slightly above or below  $(6\bar{9}8)_{2H}$  plane and which appears as a result of buckling of the thin film specimen;
- Streaking;
- + Streak intersections, and
- x Double diffraction reflections.

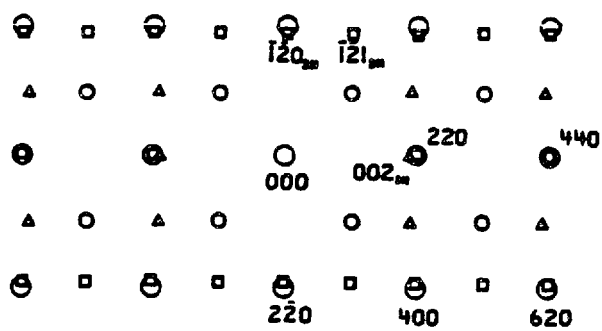
In a diffraction pattern slightly off the  $[001]_{\beta_1}$  zone shown in Figure 24, the  $\langle 110 \rangle_{\beta_1}$  streaking and the diffuse extra reflections are more pronounced. Furthermore, there is a close similarity between the diffraction pattern in Figure 24 and the corresponding pattern of a number of  $\beta$ -phase noble-metal base alloys (105-113). As discussed by Delaey et al. (105), the extra diffraction spots can be explained by the presence of two phases: the  $\omega$ -phase (106-108) and an hexagonal 2H-type phase (109-113). More recently, Murakami et al. (110) analyzed extra reflections in the quenched Cu-Zn-Al alloy and demonstrated that all

Figure 24 An  $\sim[001]_{\beta_1}$  diffraction pattern, (a) , in the alloy B2 and the corresponding index diagram, (b) , which postulates the existence of the 2H-phase precipitates.





(a)



~[001]<sub>β<sub>1</sub></sub> ZONE

(b)

Fig. 24

the extra reflections could be explained by the 2H-type structure. Using a  $\beta_1 \rightarrow 2H$  transformation correspondence proposed by Takezawa and Sato (109), it was shown that the 2H-phase could be present in six different transformation variants. Murakami et al. (110) further used a computer program developed by Van Houtte et al. (114) to construct index diagrams corresponding to different  $\beta_1$ -zones and associated 2H-zones (all the six 2H-variants were considered). These index diagrams are used throughout this thesis for comparison with the corresponding diffraction patterns.

In the exact  $[\bar{1}13]_{\beta_1}$  zone, Figure 25(a), no extra reflections are observed. This is consistent with the corresponding index diagram, Figure 25(b). However, streaking in  $[110]_{\beta_1}$  direction is present giving rise to an elongation of diffraction spots in this direction.

In the diffraction pattern  $\sim[\bar{1}13]_{\beta_1}$ , Figure 26(a), streaking is present not only in  $[110]_{\beta_1}$  but also in  $[2\bar{1}1]_{\beta_1}$  and  $[1\bar{2}1]_{\beta_1}$  directions. Furthermore, some extra spots are present which are in excellent agreement with the index diagram which postulates the presence of the 2H-type phase (Figure 26(b)).

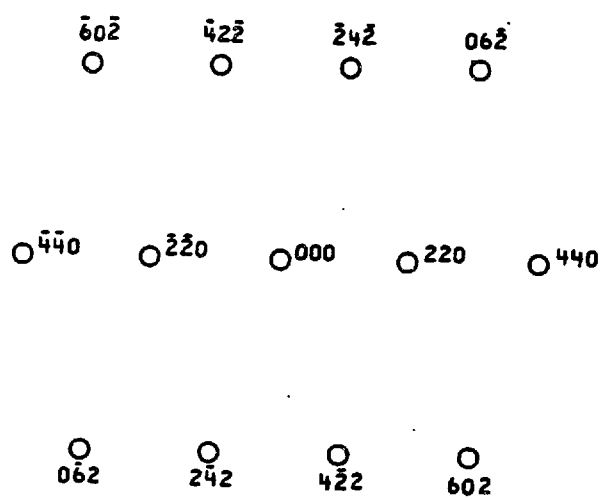
An exact  $[1\bar{1}2]_{\beta_1}$  zone, Figure 25(a), shows some additional  $[\bar{1}32]_{\beta_1}$  and  $[\bar{3}12]_{\beta_1}$  streaking. Furthermore, extra reflections which are observed are consistent with a  $[\bar{2}30]_{2H}$  zone as suggested by the index diagram, Figure 27(b).

Besides the streaking in  $\langle 110 \rangle_{\beta_1}$  direction, the exact  $[1\bar{1}1]_{\beta_1}$  zone, Figure 28, shows no extra reflections. However, tilting the specimen off the  $[1\bar{1}1]_{\beta_1}$  orientations, Figure 29(a), gives rise to the appearance of

Figure 25 The exact  $[\bar{1}13]_{\beta_1}$  diffraction pattern in the alloy B2, (a) ,  
and the corresponding index diagram, (b) .which  
postulates a presence of the 2H-phase precipitates.



(a)

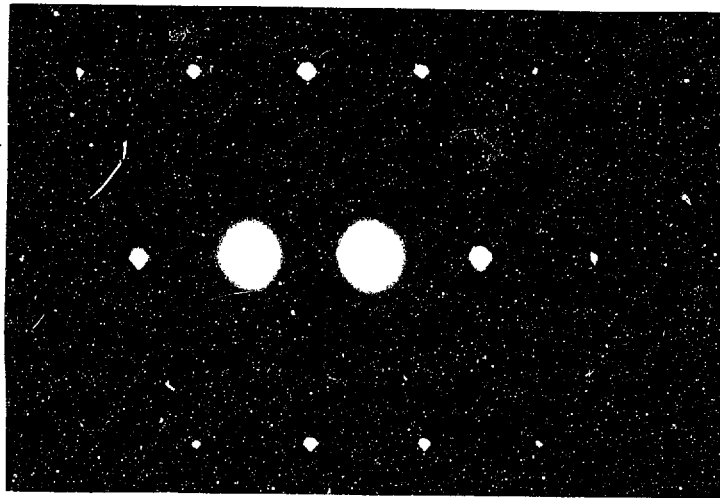


[113]<sub>β</sub> ZONE

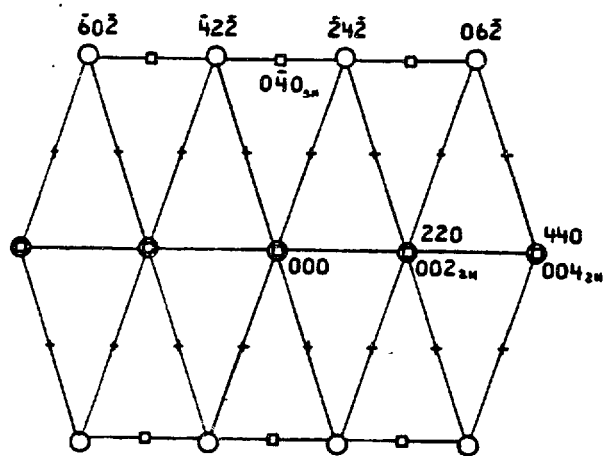
-- (b)

Fig. 25

Figure 26 An  $\sim[\bar{1}13]_{\beta_1}$  diffraction pattern in the alloy B2, (a) ,  
and the corresponding index diagram, (b) ,which  
postulates a presence of the 2H-phase precipitates.



(a)

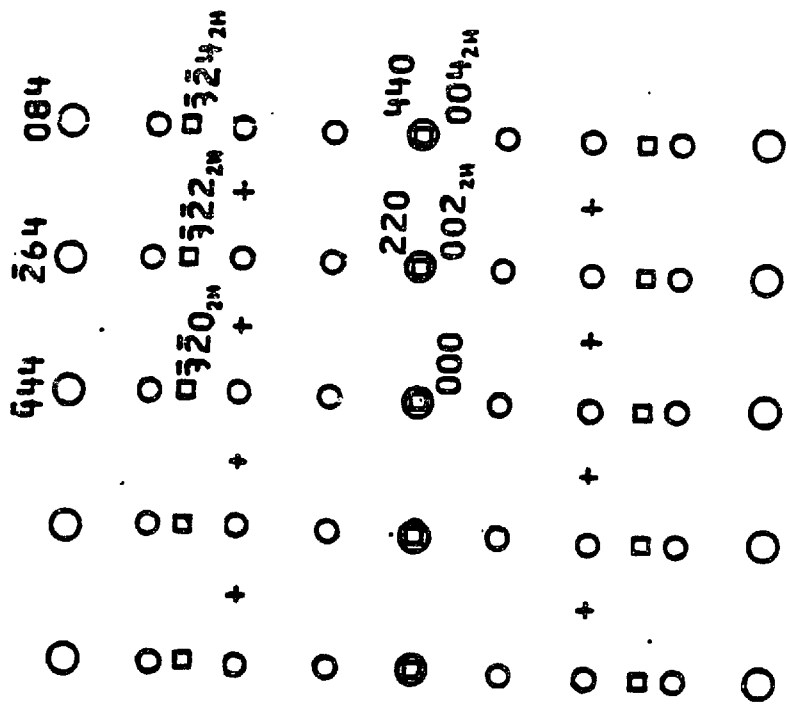


$\sim [11\bar{3}]_{\rho_1}$  ZONE

(b)

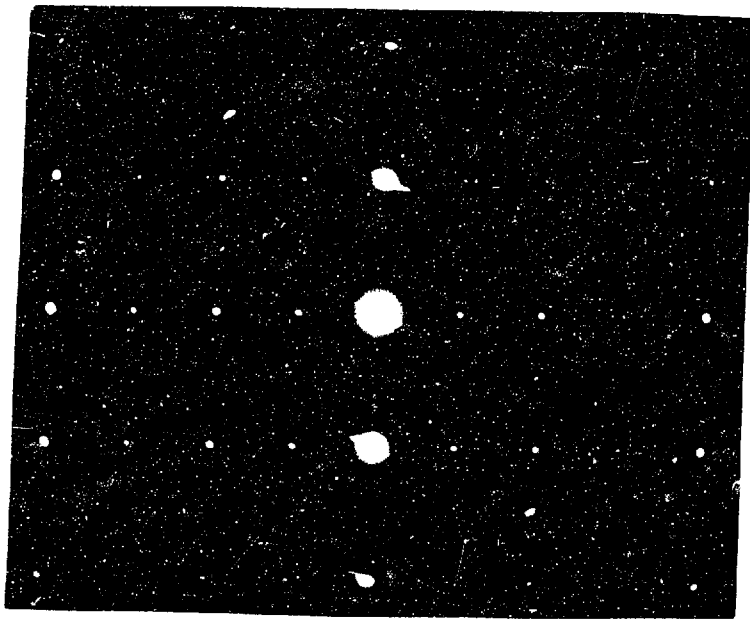
Fig. 26

Figure 27 The exact  $[1\bar{1}2]_{\beta_1}$  diffraction pattern in the alloy B2, (a) , and the corresponding index diagram, (b) ,which postulates an existence of the 2H-phase precipitates.



$[112]_{\beta_1}$  ZONE

(b)

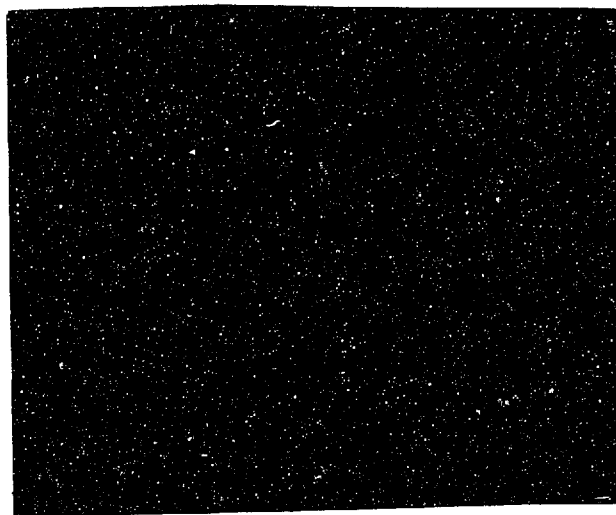


(a)

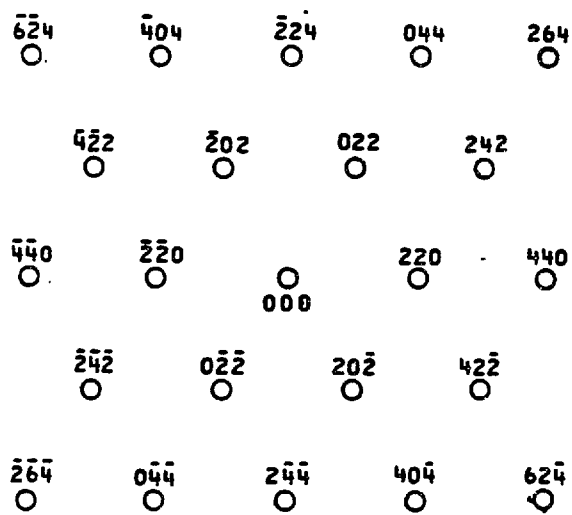
Figure 27



Figure 28 The exact  $[1\bar{1}1]_{\beta_1}$  diffraction pattern in the alloy B2, (a), and the corresponding index diagram, (b), which assumes a presence of the 2H-phase precipitates.



(a)

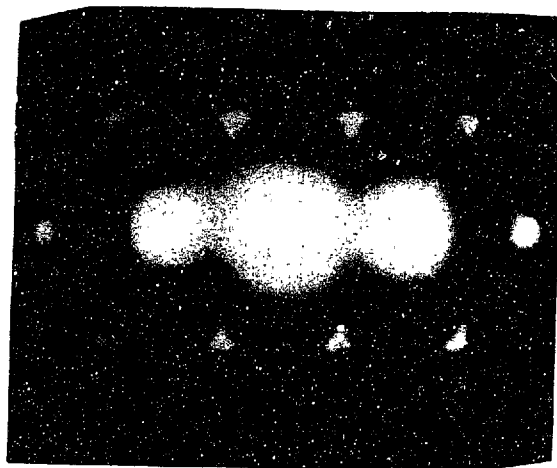


$[1\bar{1}1]_{\beta_1}$  ZONE

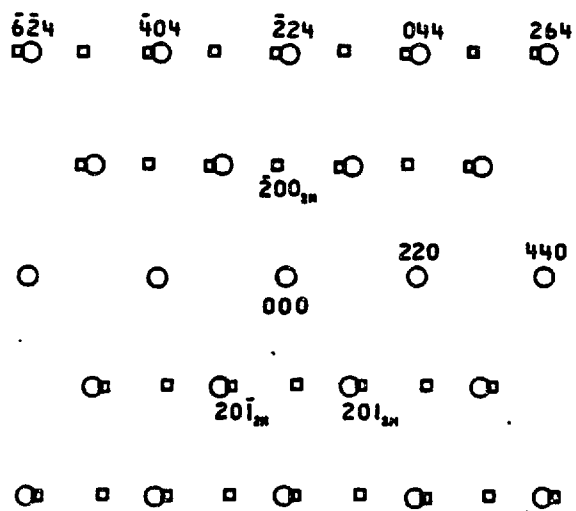
(b)

Fig. 28

Figure 29 An  $[1\bar{1}1]_{\beta_1}$  diffraction pattern in the alloy B2, (a) ,  
and the corresponding index diagram, (b) ,which  
postulates a presence of the 2H-phase precipitates.



(a)


 $\sim[111]_{\beta_1}$  ZONE

(b)

Fig. 29

extra spots. These spots can be explained by the index diagram shown in Figure 29(b). Furthermore, intersection of  $\langle 110 \rangle_{\beta_1}$  streaks with the  $[1\bar{1}1]_{\beta_1}$  zone may account for the apparent triangular shape of the matrix reflections in Figure 29(a).

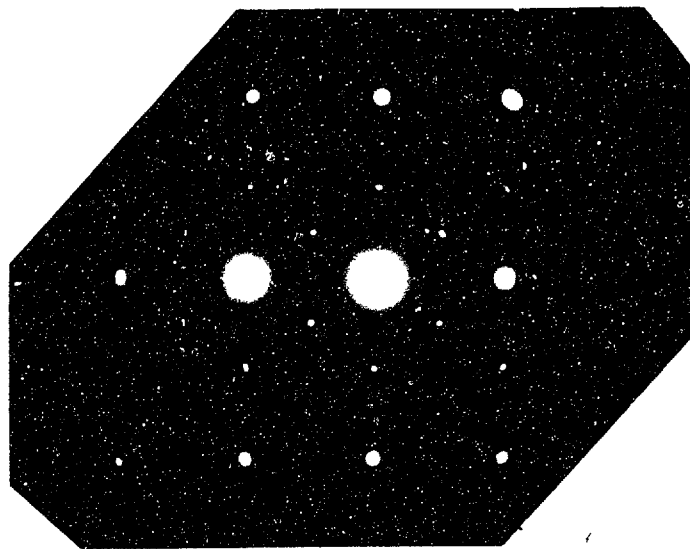
The  $[0\bar{1}1]_{\beta_1}$  zone, Figure 30, contains  $[011]_{\beta_1}$ ,  $[211]_{\beta_1}$  and  $[\bar{2}11]_{\beta_1}$  streaking as well as some extra reflections. Again, all the extra reflections could be accounted for by a 2H-type phase.

To summarize, all the extra reflections observed within several prominent diffraction  $\beta_1$ -zones can be explained by the presence of the 2H-type phase proposed by Takezawa and Sato (13). This also suggests that both the large and the fine precipitates have the same 2H-structure. The fine precipitates probably form as a result of room temperature aging.

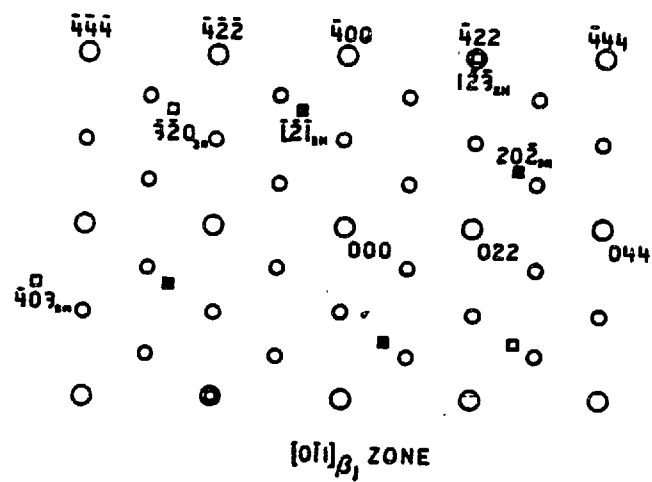
Otsuka et al. (111) have shown, by heating specimens inside the electron microscope, that the 2H-phase disappears at some critical temperature, estimated to be between 500 to 600K. Upon cooling, the 2H-phase reappears very quickly, suggesting that its formation is diffusionless. In situ observation (111) also showed that the 2H-phase remained present after a martensitic transformation was induced by cooling the specimen. No interaction of the nucleating martensite and the 2H-type particles was observed.

The formation mechanism of the 2H-type phase, proposed by Takezawa and Sato (109), involves two shear modes: The first shear mode,  $(1\bar{1}2)_{\beta_1}$   $[\bar{1}11]_{\beta_1}$ , introduces a lattice deformation, and the second shear mode,  $(110)_{\beta_1}$   $[1\bar{1}0]_{\beta_1}$ , introduces a shuffling, which produces correct stacking

Figure 30 The exact  $[0\bar{1}1]_{\beta_1}$  diffraction pattern of the alloy B2, (a), and the corresponding index diagram, (b), which postulates a presence of the 2H-phase precipitates.



(a)



(b)

Fig. 30

sequence of the close-packed planes in the obtained orthorhombic structure. The elastic constants associated with these two shear modes are found to be relatively small, when compared with other shear elastic constants, Figure 10. Low resistance of the lattice with respect to these two shears then explains the occurrence of the 2H-type phase at room temperature and its insuppressibility by fast quenching.

The striated structure of the coarse 2H-precipitates can be explained as resulting from a lattice invariant deformation accomplished by twinning on  $\{121\}_{2H} \parallel \{110\}_{\beta_1}$ . Splitting of some 2H-reflections in  $\langle 110 \rangle_{\beta_1}$  directions, as best seen in Figure 17, supports this view. Most fine precipitates are completely enclosed by the matrix phase. This may explain the absence of striations, which are defined as lines of intersections of twinning planes with the foil surface. Nevertheless, the periodic twinned structure of the fine precipitates gives rise to the formation of Moiré fringes which appear to be close to  $\langle 110 \rangle_{\beta_1}$  orientations.

#### 5.5.5. "Tweed" structure

Some fine-scale modulation in image contrast are found in regions near the extinction contours. These are commonly referred to as "tweed" structure. This modulation appears usually in a regular pattern, cross-hatched, striated, or speckled. Figure 31 gives an example of the tweed structure in alloy B1, for the foil orientation  $\sim [001]_{\beta_1}$ . The mottling is of a much finer scale (3 - 6 nm) than the domain size (0.15 - 0.25  $\mu\text{m}$ ) and therefore does not appear to be related to the ordering.



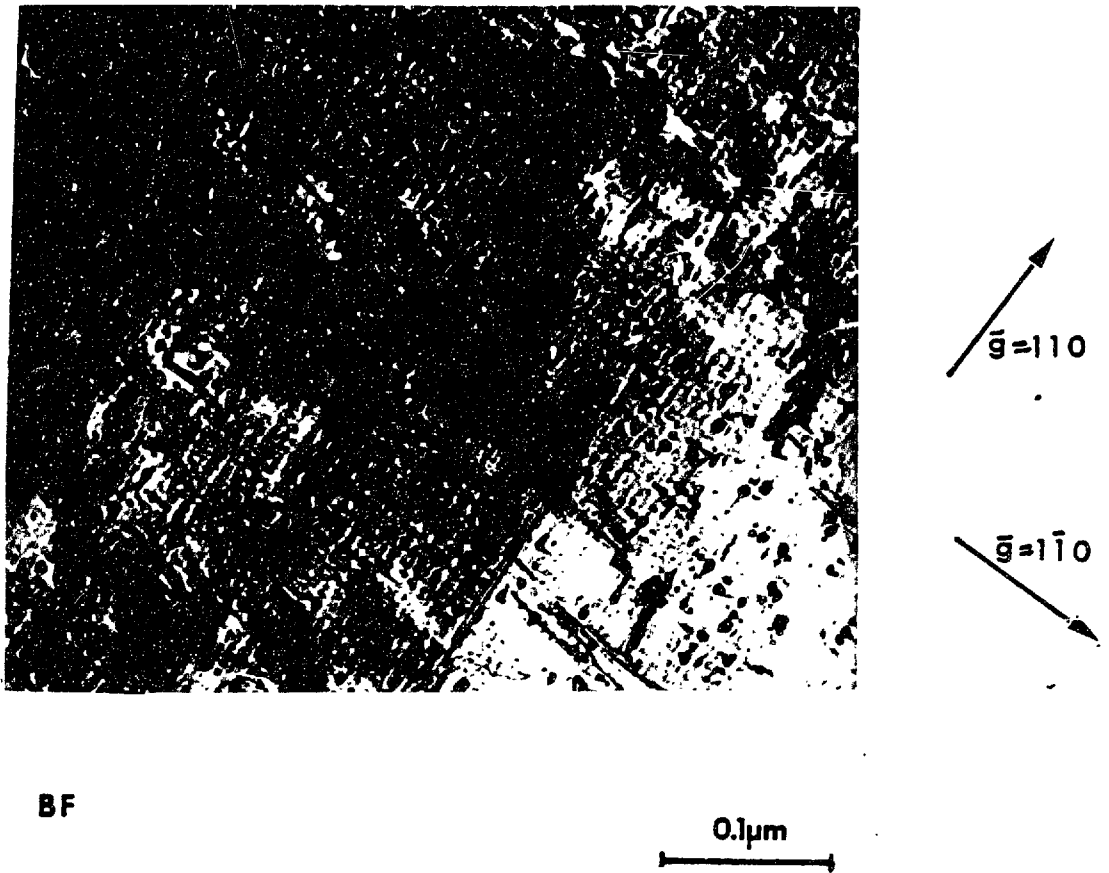


Figure 31 Typical Tweed (mottled) structure in Cu-Al-Ni alloys, alloy B1. Orientation of the foil  $\sim [001]_{\beta_1}$ .

The same kind of mottled structure has been reported to occur in other noble-metal base alloys (115 - 122). It is this phenomenon, which is often considered to be responsible for diffraction effects such as: diffuse streaking in certain directions, splitting of certain diffraction spots, appearance of some extra diffuse diffraction spots. Since all these diffraction effects are found in the present work, we assume they are associated with the mottling.

The origin of the mottling has been variously interpreted, often on the basis of incomplete arguments. The following description had been given: (i) strain contrast around coherent precipitates (115); (ii) fine precipitates surrounded by envelopes of rejected solute (116); (iii) fine-scale stress-induced martensite (117); (iv) periodic modulation of shear strains, static displacements (118,119); (v) low frequency acoustic phonon modes, or other dynamic displacements (120,121); (vi) local lattice instabilities caused by the clustering of quenched-in vacancies (122). All these theories associate the mottled structure with the presence of some continuous or localized domains of lattice distortion, regularly distributed. It is the exact nature and origin of the lattice distortion that these theories do not agree upon. In the case at hand, two descriptions of these domains seem to be more appropriate than the others: (i) fine-scale (most probably) coherent precipitation of the 2H-phase, and (ii) domains with tetragonal symmetry formed through interaction of  $\{110\}\langle 1\bar{1}0 \rangle_{\beta_1}$  displacement waves (118). The cross-hatched tweed pattern, with striations lying parallel to traces

of  $\{110\}_{\beta_1}$  planes, Figure 31, is a strong indication of presence of the distorted domains, as described in (ii).

## 6. MODELS

### 6.1. Prediction of the $\beta_1 \rightarrow \gamma_1'$ Interface Structure

The crystallography of the  $\beta_1 \rightarrow \gamma_1'$  martensitic transformation in Cu-Al-Ni alloys has been well established, both theoretically (68) and experimentally (123-126). The major crystallographic features of the transformation are summarized in Table 3.

According to the Olson-Cohen theory of interface structure (16), an interface of twinned martensite, as in the case at hand, contains alternate arrays of coherency dislocations with no anticoherency dislocation content. In order to further describe the fine structure of the  $\beta_1 \rightarrow \gamma_1'$  interface, Olson's criterion (14) for the topological significance of the potential coherency dislocations can be employed. The criterion is based on two parameters:

- $\rho_L$  - number of atoms per unit dislocation length, and
- $\beta$  - a dimensionless parameter expressing a topological resolvability of dislocation lines.

Coherency dislocations with the highest values of both  $\rho_L$  and  $\beta$  are then considered as the most significant, topologically and mechanistically.

Beginning with planes of the largest interplanar spacing and with normals near the habit plane normal,  $\vec{n}$ , a systematic calculation of the parameters  $\rho_L$  and  $\beta$  was conducted. Due to the twinned structure of the  $\gamma_1'$ -martensite, it is expected that local microtopography of the

TABLE 3. CRYSTALLOGRAPHY OF THE  $\beta_1-\gamma_1'$  TRANSFORMATION

		<u>Reference</u>
Habit Plane Normal	$\begin{bmatrix} 0.71536 \\ 0.64969 \\ -0.25724 \end{bmatrix}_{\beta_1}$	(68)
Direction of the Invariant Plane Strain	$\begin{bmatrix} 0.60100 \\ -0.77935 \\ -0.17727 \end{bmatrix}_{\beta_1}$	(68)
Magnitude of the Invariant Plane Strain	0.09589	(68)
Orientation Relationship	$(110)_{\beta_1} : 1.46^\circ$ away from $(121)_{\gamma_1'}$ .  $[1\bar{1}\bar{1}]_{\beta_1} : 0.44^\circ$ away from $[2\bar{1}0]_{\gamma_1'}$ .	(68)
Lattice Invariant Twinning Shear	$(121)_{\gamma_1'}$ [1, 0.7954, 0.5907] $_{\gamma_1'}$	(126,127)
Magnitude of the Twinning Shear	0.261	(127)

interface depends on which of the two martensite variants ( $\gamma_1'$  (I) or  $\gamma_1'$  (II)) is in contact with the parent phase.

Calculated values of the  $\rho_L$  and  $\beta$  parameters are generally affected by the choice of a reference lattice, with respect to which the Burgers

vector of coherency dislocations is defined. Two cases were considered here pertaining to the choice of either  $\beta_1$  or  $\gamma_1'$  disordered structures as reference lattices. Calculated values of  $\rho_L$  and  $\beta$ , for an atomically-flat  $\beta_1$ - $\gamma_1'$  interface, are given in Tables 4 to 7.

As anticipated, the coherency dislocations associated with the close-packed  $\{110\}_{\beta_1}$  planes (and the corresponding  $\gamma_1'$  planes) appear to have the greatest significance, in terms of both  $\rho_L$  and  $\beta$  parameters. Furthermore,  $(110)_{\beta_1}$  planes with a normal near  $\vec{n}$  show appreciably higher values of  $\rho_L$ ,  $\beta$  and the dislocation spacing,  $s$ , than other planes. Other dislocations, with some prospective significance, appear to be associated with  $(0\bar{1}1)_{\beta_1}$  and  $(101)_{\beta_1}$  and the corresponding  $\gamma_1'$ -planes. The coherency dislocations associated with the  $(0\bar{1}1)_{\beta_1}$  plane, which correspond to the twinning plane of the martensite phase, will be used in Section 6.3 for calculation of the stress field associated with the  $\beta_1$ - $\gamma_1'$  interface.

A comparison of Tables 4 and 5 with Tables 6 and 7 suggests that a choice of the reference lattice does affect  $\rho_L$  and  $\beta$ . However, both reference lattices selected here have yielded the same most significant coherency dislocation arrays of the interface. Using the data from Tables 4 to 7 and a simple calculation procedure for the dislocation line direction, an arrangement of the three most significant coherency dislocation arrays is depicted in Figure 32 ( $\beta_1$  taken as the reference lattice) and in Figure 33 ( $\gamma_1'$  taken as the reference lattice). The relative width of the lines reflects the relative value of the  $\beta$ -parameter.

TABLE 4:

COHERENCY DISLOCATIONS IN  $\beta_1-\gamma_1$  ( VARIANT I ) INTERFACE

hkl	$\alpha$	$\vec{d}/a_0$	$d, \text{\AA}$	$\vec{b}_I/a_0$	$b_I, \text{\AA}$	$\rho_L, \text{\AA}^{-1}$	$s, \text{\AA}$	$\beta$
110	15.15°	$\begin{array}{l} 1/2 \\ 1/2 \\ 0 \end{array} \Big  \beta$	2.063	$\begin{array}{l} .044620 \\ -.071246 \\ -.051746 \end{array} \Big  \beta$	0.262	0.043	7.894	0.344
200	44.33°	$\begin{array}{l} 1/2 \\ 0 \\ 0 \end{array} \Big  \beta$	1.459	$\begin{array}{l} .020852 \\ .023742 \\ -.012295 \end{array} \Big  \beta$	0.103	0.012	2.088	0.025
211	17.38°	$\begin{array}{l} 1/3 \\ 1/6 \\ 1/6 \end{array} \Big  \beta$	1.191	$\begin{array}{l} .025929 \\ -.042454 \\ -.019988 \end{array} \Big  \beta$	0.156	0.015	3.988	0.060
310	27.86°	$\begin{array}{l} 3/10 \\ 1/10 \\ 0 \end{array} \Big  \beta$	0.923	$\begin{array}{l} .017273 \\ -.025281 \\ -.009105 \end{array} \Big  \beta$	0.093	0.007	1.975	0.014
321	8.27°	$\begin{array}{l} 3/14 \\ 1/7 \\ 1/14 \end{array} \Big  \beta$	0.780	$\begin{array}{l} .017487 \\ -.028372 \\ -.013067 \end{array} \Big  \beta$	0.104	0.006	5.418	0.035
332	10.65°	$\begin{array}{l} 3/22 \\ 3/22 \\ 1/11 \end{array} \Big  \beta$	0.622	$\begin{array}{l} -.014045 \\ -.024619 \\ -.012429 \end{array} \Big  \beta$	0.091	0.004	3.365	0.015
662	3.13°	$\begin{array}{l} 6/76 \\ 6/76 \\ 1/38 \end{array} \Big  \beta$	0.335	$\begin{array}{l} .007692 \\ -.012751 \\ -.006172 \end{array} \Big  \beta$	0.047	0.001	6.127	0.008
011	129.9°	$\begin{array}{l} 0 \\ 1/2 \\ 1/2 \end{array} \Big  \beta$	2.063	$\begin{array}{l} -.037101 \\ .071517 \\ .041414 \end{array} \Big  \beta$	0.271	0.042	2.689	0.121
$\frac{1}{2}0\frac{1}{2}$	87.8°	$\begin{array}{l} 1 \\ 0 \\ 1 \end{array} \Big  \beta$	4.126	$\begin{array}{l} .008272 \\ .001356 \\ .014200 \end{array} \Big  \beta$	0.048	0.064	4.128	0.133

TABLE 5:

COHERENCY DISLOCATIONS IN  $\beta_1-\gamma_1$  (VARIANT II) INTERFACE

hkl	$\alpha$	$\vec{d}/a_0$	$d, \text{\AA}$	$\vec{b}_{II}/a_0$	$b_{II}, \text{\AA}$	$\rho_L, \text{\AA}^{-1}$	$s, \text{\AA}$	$\beta$
$\frac{11}{22}0$	$15.15^\circ$	$\begin{array}{c} 1 \\ 1 \\ 0 \end{array} \Big  \beta$	4.216	$\begin{array}{c} .020188 \\ -.024921 \\ -.004210 \end{array} \Big  \beta$	0.094	0.352	15.788	1.414
200	$44.33^\circ$	$\begin{array}{c} 1/2 \\ 0 \\ 0 \end{array} \Big  \beta$	1.459	$\begin{array}{c} .026797 \\ -.001976 \\ .037549 \end{array} \Big  \beta$	0.134	0.011	2.088	0.023
$21\bar{1}$	$17.38^\circ$	$\begin{array}{c} 1/3 \\ 1/6 \\ 1/6 \end{array} \Big  \beta$	1.191	$\begin{array}{c} .014173 \\ .003241 \\ .025801 \end{array} \Big  \beta$	0.086	0.008	3.988	0.033
310	$27.80^\circ$	$\begin{array}{c} 3/10 \\ 1/10 \\ 0 \end{array} \Big  \beta$	0.923	$\begin{array}{c} .013435 \\ -.010364 \\ .005825 \end{array} \Big  \beta$	0.052	0.004	1.975	0.008
$32\bar{1}$	$8.27^\circ$	$\begin{array}{c} 3/14 \\ 1/7 \\ 1/14 \end{array} \Big  \beta$	0.780	$\begin{array}{c} .009802 \\ .001107 \\ .016471 \end{array} \Big  \beta$	0.056	0.003	5.418	0.019
$33\bar{2}$	$10.65^\circ$	$\begin{array}{c} 3/22 \\ 3/22 \\ 1/11 \end{array} \Big  \beta$	0.622	$\begin{array}{c} .007157 \\ .005036 \\ .016871 \end{array} \Big  \beta$	0.059	0.003	3.366	0.010
$66\bar{2}$	$3.13^\circ$	$\begin{array}{c} 6/76 \\ 6/76 \\ 1/38 \end{array} \Big  \beta$	0.355	$\begin{array}{c} .004351 \\ .000891 \\ .007092 \end{array} \Big  \beta$	0.027	0.001	6.127	0.005
$01\bar{1}$	$129.90^\circ$	$\begin{array}{c} 0 \\ 1/2 \\ 1/2 \end{array} \Big  \beta$	2.063	$\begin{array}{c} -.005160 \\ -.056061 \\ -.008602 \end{array} \Big  \beta$	0.305	0.051	2.689	0.136
101	$87.80^\circ$	$\begin{array}{c} 1/2 \\ 0 \\ 1/2 \end{array} \Big  \beta$	2.063	$\begin{array}{c} .015748 \\ -.084717 \\ -.055244 \end{array} \Big  \beta$	0.234	0.039	2.064	0.082



TABLE 6;

COHERENCY DISLOCATIONS IN  $\gamma_1'$  (VARIANT I) -  $\beta_1$  INTERFACE

$(hkl)_{\gamma_1(I)}$	$\alpha$	$\vec{d}/a_0$	$d, \text{\AA}$	$\vec{b}_I/a_0$	$b_I, \text{\AA}$	$\rho_L$	$s, \text{\AA}$	$\beta$
121	15.23°	.506494 .519991 -.016239   β	2.118	-.045485 .072285 .031864   β	0.206	0.035	8.064	0.283
101	47.05°	.478913 -.025747 .012296   β	1.400	-.018343 .022892 .004170   β	0.086	0.010	1.912	0.019
321	31.02°	.326133 .157105 -.160952   β	1.156	-.024619 .039816 .018705   β	0.146	0.014	2.243	0.031
323	28.34°	.292864 .094485 .001671   β	0.898	-.016434 .023614 .008041   β	0.087	0.006	1.191	0.012
221	21.98°	.212143 .141605 -.071249   β	0.773	-.017049 .027391 .012353   β	0.101	0.006	2.064	0.013
561	27.89°	.136886 .137277 -.091504   β	0.626	-.014229 .024128 .012069   β	0.089	0.004	1.337	0.006
231	21.40°	.079611 .080784 -.027778   β	0.341	-.007710 .017692 .006010   β	0.047	0.001	0.934	0.001
12 $\bar{1}$	59.80°	-.020712 -.518810 .507448   β	2.118	.037117 -.073669 -.046277   β	0.276	0.048	2.634	0.123
001	64.93°	.871564 .002218 .980418   β	4.230	-.008316 -.001583 -.014412   β	0.049	0.081	4.612	0.114

TABLE 7:

COHERENCY DISLOCATIONS IN  $\gamma_1'$  (VARIANT II)- $\beta_1$  INTERFACE

$(hkl)_{\gamma_1(II)}$	$\alpha$	$\vec{d}/a_0$	$d, \text{\AA}$	$\vec{b}_{II}/a_0$	$b_{II}, \text{\AA}$	$\rho_L$	$s, \text{\AA}$	$\beta$
001	17.59°	$\begin{array}{l} 1.009474 \\ .940894 \\ .064302 \end{array} \Big  \beta$	4.030	$\begin{array}{l} -.028146 \\ .009874 \\ -.028670 \end{array} \Big  \beta$	0.121	0.320	13.44	1.096
10 $\bar{1}$	44.87°	$\begin{array}{l} .419813 \\ -.006608 \\ -.004469 \end{array} \Big  \beta$	1.400	$\begin{array}{l} -.019647 \\ -.025608 \\ -.049750 \end{array} \Big  \beta$	0.096	0.011	1.985	0.021
1 $\bar{2}\bar{3}$	17.33°	$\begin{array}{l} .326779 \\ .108532 \\ -.172128 \end{array} \Big  \beta$	1.185	$\begin{array}{l} -.014713 \\ -.001609 \\ -.024357 \end{array} \Big  \beta$	0.083	0.008	3.976	0.031
10 $\bar{2}$	29.23°	$\begin{array}{l} .292872 \\ .091446 \\ .004643 \end{array} \Big  \beta$	0.895	$\begin{array}{l} -.013488 \\ .012218 \\ -.003334 \end{array} \Big  \beta$	0.054	0.004	1.833	0.007
21 $\bar{5}$	8.63°	$\begin{array}{l} .212153 \\ .139434 \\ -.069176 \end{array} \Big  \beta$	0.768	$\begin{array}{l} -.010328 \\ -.000731 \\ -.014527 \end{array} \Big  \beta$	0.052	0.003	5.118	0.016
023	10.42°	$\begin{array}{l} .136889 \\ .135896 \\ -.080155 \end{array} \Big  \beta$	0.621	$\begin{array}{l} -.007014 \\ -.004636 \\ -.016974 \end{array} \Big  \beta$	0.055	0.063	3.435	0.009
013	2.45°	$\begin{array}{l} .079473 \\ .076479 \\ -.025599 \end{array} \Big  \beta$	0.330	$\begin{array}{l} -.004257 \\ -.000704 \\ -.007340 \end{array} \Big  \beta$	0.025	0.001	7.718	0.005
121	131.60°	$\begin{array}{l} -.020711 \\ -.518811 \\ .507448 \end{array} \Big  \beta$	2.119	$\begin{array}{l} .004855 \\ .056043 \\ .085021 \end{array} \Big  \beta$	0.297	0.051	2.835	0.144
12 $\bar{1}$	75.89°	$\begin{array}{l} -.484023 \\ -.046364 \\ .539389 \end{array} \Big  \beta$	2.120	$\begin{array}{l} -.023291 \\ .065918 \\ .056400 \end{array} \Big  \beta$	0.263	0.045	2.185	0.098

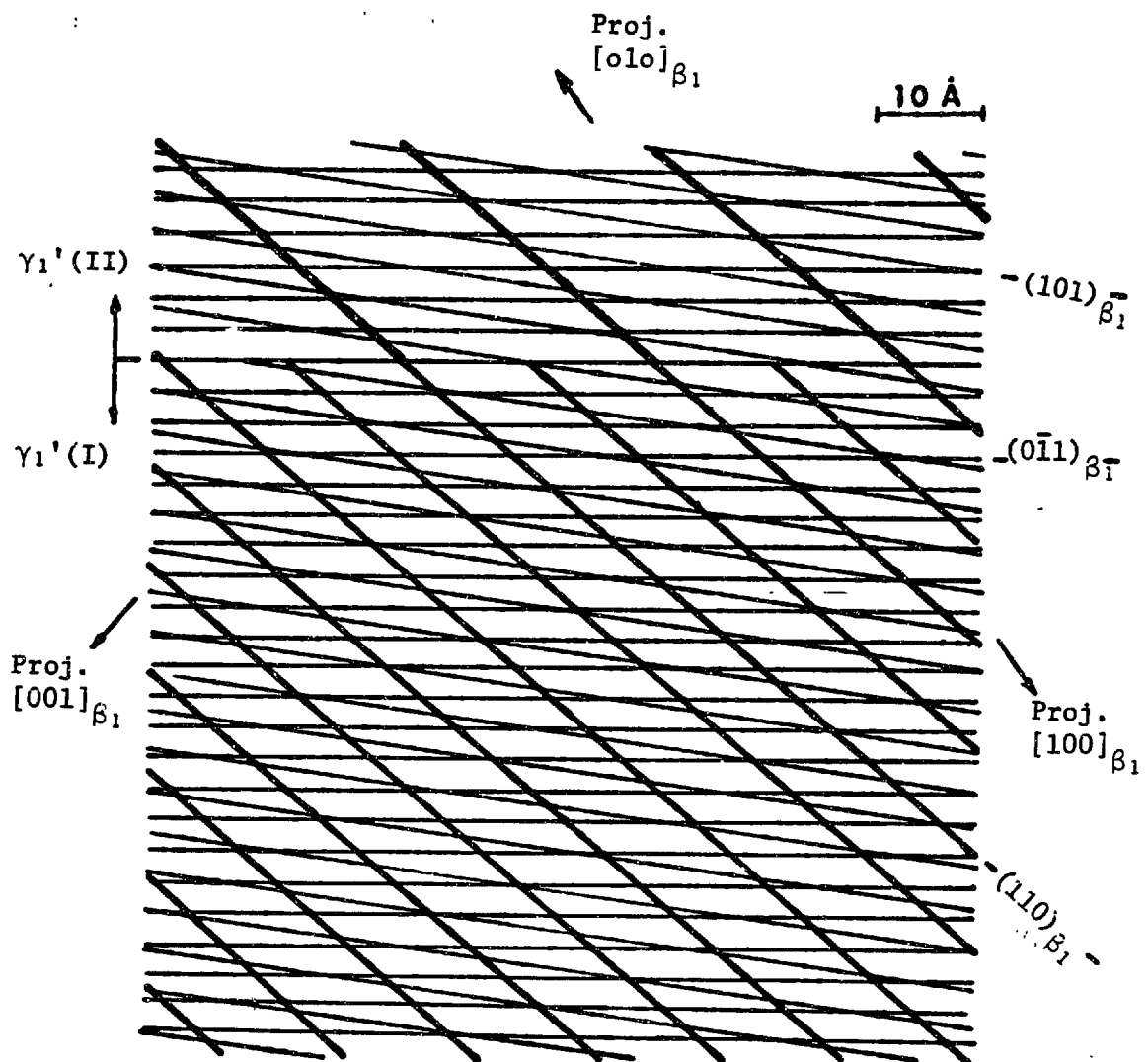


Figure 32 Computed configuration of most significant coherency dislocations in  $\beta_1$ - $\gamma_1'$  interface (Parent phase is taken as the reference lattice).

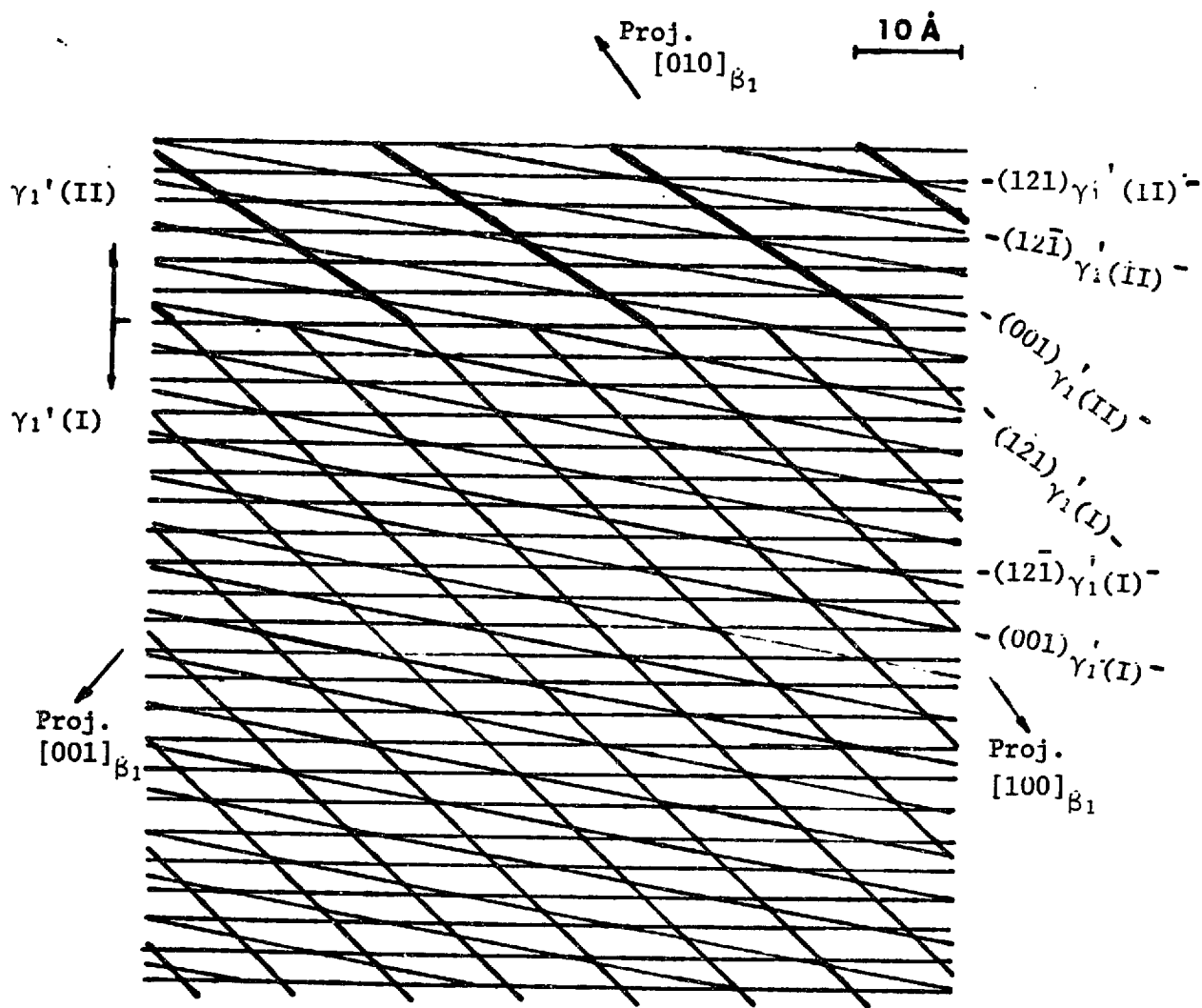


Figure 33 Computed configurations of most significant coherency dislocations in  $\beta_1$ - $\gamma_1'$  interface ( $\gamma_1'$  martensite is taken as the reference lattice).

## 6.2. The Peierls Energy of an Interface

As long as interface dislocations, both coherency and anti-coherency, are well separated, it seems appropriate and justified to consider them as individual, separate line discontinuities. Motion kinetics of the interface is then expected to be governed by individual dislocations, and various models for microscopic slip (48) can be invoked to describe possible interactions of the moving interface with potential obstacles to its motion. Specifically, for the case of twinned martensite, the Peierls energy model (128) can be applied to explain a variation in the energy of coherency dislocations accompanying their motion. The variation of the energy,  $\epsilon$ , of a dislocation moving in the y-direction is often represented as (128):

$$\epsilon = \epsilon_0 \left[ 1 - \frac{e^{-\frac{4\pi\delta}{\lambda}}}{\ln(R/\delta)} \cos 2\pi \frac{y}{\lambda} \right] \quad (22)$$

where:

$\epsilon_0$  - dislocation line tension which is proportional to the Burgers vector squared and is thus smaller for partial (coherency) dislocations than for lattice dislocations,

$\delta$  - effective width of a dislocation,

$\lambda$  - periodicity of the dislocation energy function, and

$R$  - average dislocation spacing.

The amplitude of the Peierls energy is dominated by the exponential

term in equation (22). The periodicity of the Peierls energy function,  $\lambda$ , is governed by the periodicity of the lattice and therefore should be identical for both partial and lattice dislocations, provided the dislocations are free to adopt a local minimum energy link structure. The effective dislocation width,  $\delta$ , can be expressed as:

$$\delta = (\kappa/\phi_0)^{1/2} \quad (23)$$

where:

- $\kappa$  - the strain energy gradient coefficient, and
- $\phi_0$  - the volume energy barrier for the homogeneous lattice deformation propagated by the dislocation.

$\phi_0$  is substantially smaller for the partial (coherency) dislocation which propagate transformation lattice deformation than for the lattice dislocations which propagate slip. If  $\kappa$  is taken as a constant, then the effective width become larger and consequently the amplitude of the Peierls barrier becomes smaller for partial dislocations when compared with lattice dislocations. Furthermore, since the activation volume is an inverse square root function of the Peierls energy amplitude, it takes on slightly larger values (tens of atomic volumes) for partial dislocations.

A different situation may occur when coherency dislocations are not well separated (as might be the case at hand, Section 6.1). Groups of coherency dislocations rather than individual dislocations are then expected to interact with the obstacles. In this case, the concept of the surface dislocation (5) might be more appropriate. An interface is then considered as a continuous membrane defined by the shape deformation tensor (analogous to the Burgers vector of the dislocation) and by the local orientation of the vector normal to the interface (analogous to

the dislocation line vector). The concept of the Peierls energy is expected to be applicable to the surface dislocation.

Thermally activated motion of a surface dislocation will involve nucleation of a bulge (a two-dimensional analogue of a double kink) over the Peierls barrier. This problem will be considered here.

The equation of motion of a surface dislocation, of unit area, originally lying in the x-y plane and moving in the z-direction can be written as:

$$\gamma_0 \left( \frac{\partial^2 z}{\partial x^2} + \frac{\partial^2 z}{\partial y^2} \right) - \frac{d\gamma_i}{dz} + \tau_f \cdot \gamma = 0 \quad (24)$$

where:

- $\gamma_0$  - surface tension taken as a constant;
- $\gamma_i$  - interface energy, which is a function of the interface displacement in the z-direction,
- $\tau_f$  - applied resolved shear stress, and
- $\gamma$  - macroscopic shape deformation approximated as a simple shear.

To avoid nonlinear terms in equation (24), a quasi-parabolic  $\gamma_i(z)$  function (129) can be adopted. Furthermore, an additional constraint can be applied, which involves a minimization of the activation energy associated with the critical bulge nucleation event.

The following solutions of equation (24) are then obtained:

The Bulge Shape:

$$z = \lambda(1-\beta) \left[ 1 + \cos\left(\frac{x}{\lambda} \sqrt{\frac{\Delta\gamma_1}{\gamma_0}}\right) \cos\left(\frac{y}{\lambda} \sqrt{\frac{\Delta\gamma_1}{\gamma_0}}\right) \right], \quad (25a)$$

The Activation Energy:

$$\Delta G = \frac{\pi^3}{4} \gamma_0 \lambda^2 (1-\beta)^2, \quad (25b)$$

and The Activation Volume:

$$V^* = \frac{\pi^3}{16} \frac{\lambda^3}{(\Delta\gamma_1/\gamma_0)} (1-\beta), \quad (25c)$$

where:  $\lambda$  - wavelength of the interface energy variation,  
function,  $\gamma_1(z)$ ,

$$\beta = \tau_f / \hat{\tau},$$

$\hat{\tau}$  - maximum of the Peierls friction stress, and

$\Delta\gamma_1$  - the Peierls energy amplitude.

To evaluate the activation volume using equation (25c) the relative Peierls energy amplitude,  $\Delta\gamma_1/\gamma_0$ , should be first estimated. An analogous quantity for lattice dislocations is often considered to be  $10^{-4}$  to  $10^{-3}$  for metals. The Peierls energy amplitude,  $\Delta\gamma_1$ , as demonstrated by Roitburd (151), is strongly affected by an effective width of a dislocation or an interface. If the strain-gradient-energy coefficient (148) is taken to be equal for both line and planar defects, then the defect



width is dominated by the energy barrier of the homogeneous deformation, which is propagated by motion of the defect. This energy barrier is expected to be smaller for interfaces, which propagate lattice deformations, than for lattice dislocations, which produce slip. This means that, in general, interfaces or interface (coherency) dislocations have a larger width, and thus a lower amplitude of the Peierls barrier, when compared with lattice dislocations. There is another important difference between lattice and interface dislocations. The energy of a lattice dislocation has two components, one associated with its long-range stress field and another minor component arising from the dislocation core. It is the second component of the dislocation energy that is usually considered to vary with dislocation position. An interface, on the other hand, in its equilibrium reference state, possesses no long-range stress field. A bulging of the interface then gives rise to both a variation of the core energy and a variation of the long-range strain energy. This can increase the relative amplitude,  $\Delta\gamma_i/\gamma_o$ , of the Peierls barrier for an interface. It is thus expected that the magnitude of  $\Delta\gamma_i/\gamma_o$  for interfaces is comparable with the corresponding quantity for lattice dislocations. For metals substitution of  $\lambda = 10^{-10}$  m,  $\beta = 0$  and  $\Delta\gamma_i/\gamma_o = 10^{-4}$  into equation (25c) yields  $V^* \approx 2 \times 10^4 \Omega$  ( $\Omega$ -atomic volume). However, much lower values of  $V^*$  can be expected if  $\lambda$  is taken to be a small fraction of the lattice parameter.

Substituting the previously mentioned values for  $\lambda$ ,  $\beta$  and  $\Delta\gamma_i/\gamma_o$  and  $\gamma_o = 10 - 50$  m J/m<sup>2</sup> into equation (25b) yields  $\Delta G^* = 10^{-7}$  to  $10^{-6}$  eV.

Such a small value of the activation energy suggests that the Peierls barrier associated with an interface can be easily surmounted by thermal activation. However, it is hardly likely that, in these circumstances, the Peierls energy barrier can be the rate controlling mechanism of the interface motion.

### 6.3. Stress Field of the $\beta_1-\gamma_1'$ Interface

Interface dislocations representing an interphase-boundary can be considered as source functions of the stress field of the interface. For the case of twinned martensite, therefore, the selection of the most significant coherency dislocation arrays is expected, in general, to affect the interface stress-field function. However, at a distance from the interface considerably larger than the dislocation spacing, the stress-field appears to be practically independent of the choice of dominating coherency dislocations. It is, therefore, often preferred to consider those coherency dislocation arrays, which simplify the calculation of the interface stress field. Such simple coherency dislocation arrays, in the case of an  $\beta_1-\gamma_1'$  interface, are shown in Figure 34. Figure 34a shows "twinning dislocations", one on each twinning plane of the  $\beta_1-\gamma_1'$  (II) interface, where  $\gamma_1$  (II) refers to the second twinned oriented variant of the martensite. Line direction (defined as the intersection of the twinning and the habit planes) and the Burgers vector (parallel to the twinning shear direction) can be obtained using the data from Table 3. A parallel continuous "coherency dislocation array", Figure 34b, is next added to cancel out the long-range stress field components associated with the twinning dislocation

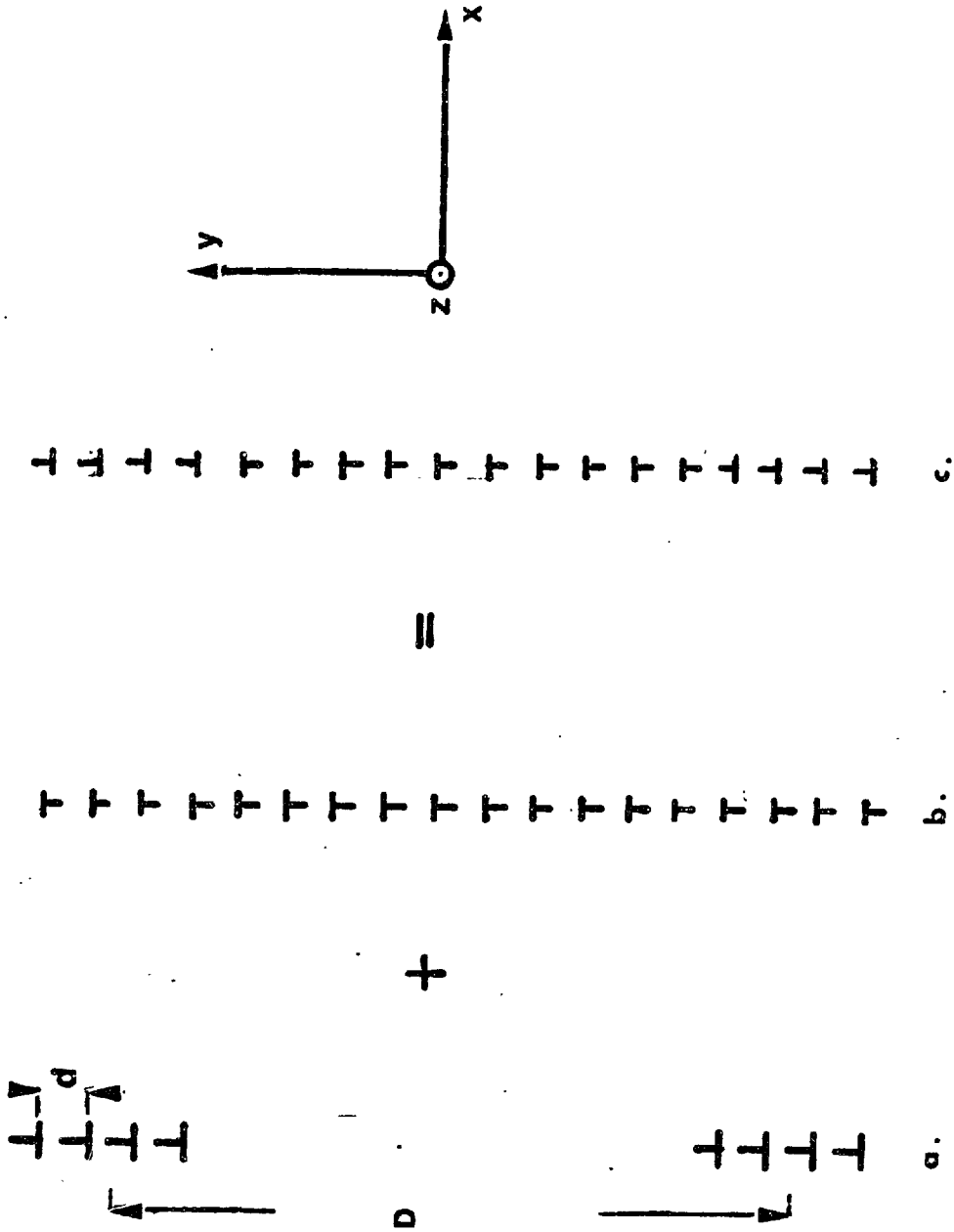


Figure 34 Discrete dislocation model of an  $\beta_1-\gamma$  martensitic interface: (a) twinning dislocations producing second variant of martensite,  $\gamma_1(\text{II})$ ; (b) "coherency" dislocations which cancel out long range stress field of the twinning dislocations; (c) total interfacial structure.

array. Superposition of these two arrays, shown in Figure 34c, yields an interface model containing alternating arrays of coherency dislocations. These dislocations correspond to those which are horizontal in the calculated interfacial structures of Figures 32 and 33.

All the dislocations shown in Figure 34c are very close to the pure screw orientation, with the angle between the Burgers vector and the line direction being only  $\sim 10.5^\circ$ . Therefore, the interface model shown in Figure 34c is approximated in these calculations by corresponding alternating arrays of pure screws. This means that with respect to a coordinate system defined by the interface normal,  $\vec{n}$ ;  $\vec{n} \times \vec{l}$ ; and dislocation line direction,  $\vec{l}$ , the interface stress tensor contains only two non-zero components,  $\sigma_{xz}$  and  $\sigma_{yz}$ . These two stress components are obtained by summing over the two alternating screw dislocation arrays, and can be expressed as

$$\sigma_{xz} = \frac{\mu b}{2D} \left[ \sum_{n=-N}^{n=N} \frac{\sin \frac{2\pi}{D} (y+nd)}{\cosh 2\pi \frac{x}{D} + \cos \frac{2\pi}{D} (y+nd)} + 0.29 \cdot \frac{D}{d} \frac{\sin 2\pi y/d}{\cosh 2\pi \frac{x}{d} - \cos 2\pi y/d} \right] \quad (26)$$

$$\sigma_{yz} = \frac{\mu b}{2D} \left[ \sum_{n=-N}^{n=+N} \frac{\sinh 2\pi \frac{x}{D}}{\cosh 2\pi \frac{x}{D} + \cos \frac{2\pi}{D} (y+nd)} - 0.29 \frac{D}{d} \frac{\sinh 2\pi \frac{x}{d}}{\cosh 2\pi \frac{x}{d} - \cos 2\pi y/d} \right] \quad (27)$$

where:  $\mu$  - shear modulus,

$b$  - Burgers vector of a twinning dislocation,  $b \approx 0.6425\text{\AA}$

$D$  - periodicity of interfacial dislocation structure, i.e., combined widths of the two adjacent variants of martensite,

- d - interfacial dislocation spacing and  $2N = 0.29 D/d$  - number of twinning dislocations within one period of interfacial structure.

Calculations done using equations (26) and (27) indicate that this stress field has a range of  $\sim D$ . Constant-stress contours, shown in Figure 35, suggest a periodic function of the stress field with the wavelength being equal to the combined widths of the two adjacent variants of martensite.

#### 6.4. Interaction of a Moving Interface with Discrete Second Phase Particles

In this section, different possible interaction mechanisms of a moving  $\beta_1-\gamma_1'$  martensitic interface with discrete particles are considered. When possible quite general solutions for interaction energies and interaction forces are sought. In other cases, however, specific solution pertaining to the interaction of the  $\beta_1-\gamma_1'$  interface with the particles identified in Section 5.5 are of primary interest.

By analogy with theories of precipitation- and work-hardening, possible mechanisms of interaction of a martensitic interface with discrete particles were divided into two categories:

- i) Interaction mechanisms which do not involve a physical contact between a particle and an interface, referred to hereafter as "long-range interaction mechanisms"; and
- ii) interaction mechanisms occurring when a particle is encountered

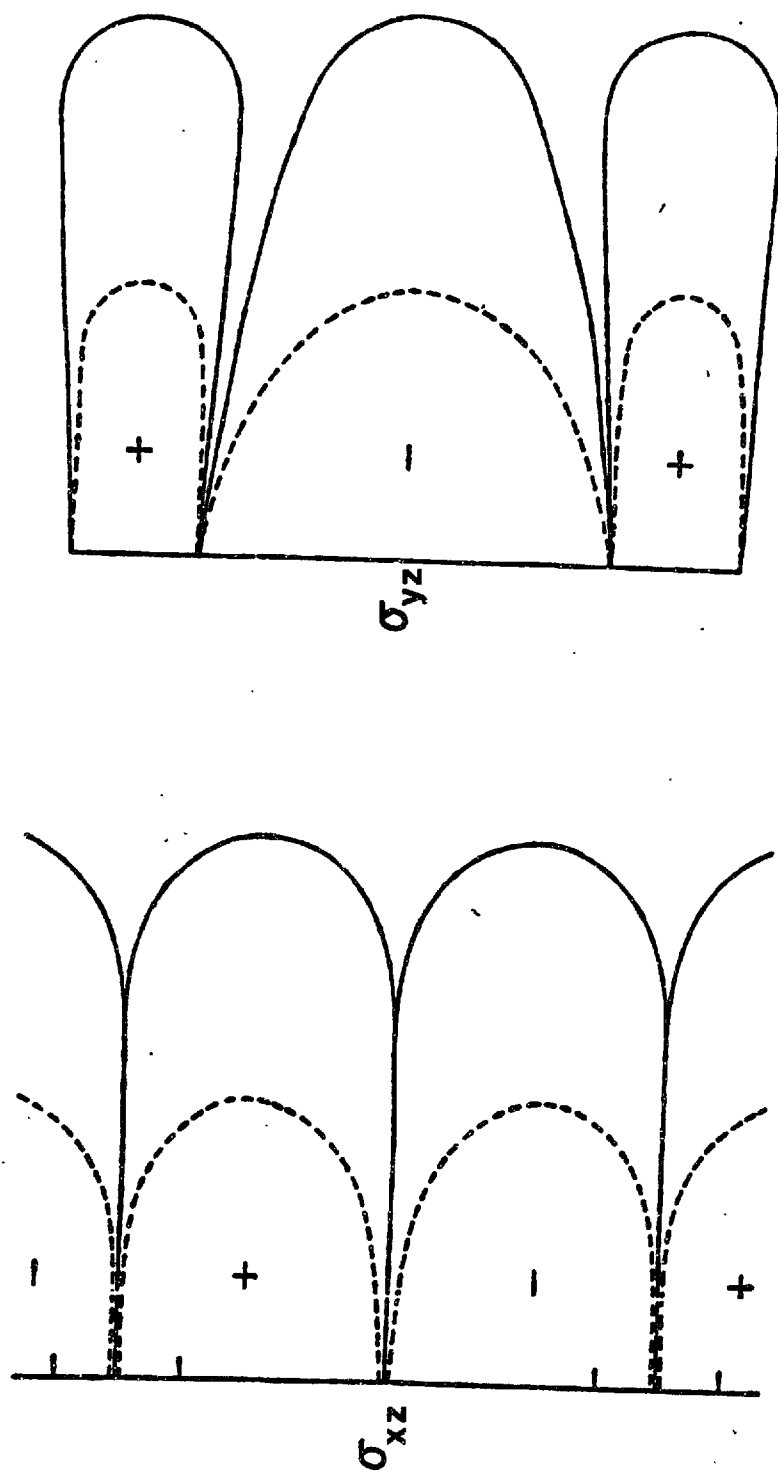


Figure 35 Constant-stress contours for a simplified dislocation model of an  $\beta_1-\gamma_1$  martensitic interface.

by a section of moving interface referred to as "short-range interaction mechanisms".

As will be shown later, there is no clear demarcation between these two types of interactions. Long-range interactions may affect the structure and morphology of a particle and, therefore, give rise to some changes in the short-range types of interaction and vice-versa.

#### 6.4.1. Long-Range Interactions

Long-range interactions involve stress and strain fields and corresponding interaction energies associated with a martensitic interface and second phase particles. When the interaction energy varies with relative position and distance of the interface and a particle, then a gradient of interaction energy defines an interaction force. In order to comply with the convention for the sign of the interaction force, the gradient term is usually preceded by a minus sign.

It is common practice to distinguish between two types of long-range interactions:

- i) modulus interaction, and
- ii) strain interaction.

Both cases were considered in the preceding sections. Due to the complexity of the problem, only isotropic linear elasticity models are considered.

### Modulus Interaction

The elastic energy density of a strained body is a function of both stress and strain components and the elastic constants of the material (119). Within the scope of the isotropic theory of elasticity, elastic constants are averaged into appropriate elastic moduli, as discussed in Section 5.3. When a material contains second-phase particles with different elastic moduli than the matrix phase, the stored elastic strain energy is changed due to the presence of these "modulus-misfit" particles. As already shown in Section 6.3, there is a stress field associated with the martensitic interface which has a range comparable with the periodicity of the interface structure. The strain energy associated with this stress field is changed when the moving interface encounters a modulus-misfit second-phase particle. The (negative) gradient of the elastic strain energy change then defines the modulus interaction force,  $F_M$ , between the interface and the particle.

A difference in elastic moduli between the parent phase,  $\mu_0$ , and a second phase,  $\mu$ , is often expressed in terms of a single "modulus misfit parameter",  $\epsilon_\mu$ , defined as:

$$\epsilon_\mu = \frac{\mu - \mu_0}{\mu_0} \quad (28)$$

Since the Poissons ratio is usually considered to be constant,  $\epsilon_\mu$  expresses a misfit in both shear and Young's moduli.

A general analysis of the modulus interaction of a martensitic interface and a particle appears to be very complicated. It not only



involves a parameter similar to  $\epsilon_{ij}$ , but also includes the periodicity of the interface structure, mode of the lattice-invariant deformation, relative position of the particle with respect to the interface, size, and shape of the particle, etc. Therefore, in this work, only the modulus interaction of the  $\beta_1-\gamma_1'$  interface with specified particles was considered. However, some generality of the solutions was regained by the use of appropriate dimensionless parameters, which are applicable to other martensitic interfaces.

A detailed derivation of the modulus interaction force between the  $\beta_1-\gamma_1'$  interface and various particles is presented in Appendix B.

The coordinate system defined in Section 6.3 will be used here. This means that the interface lies in the y-z plane (with twinning dislocations running in the z-direction) and advances in the positive x-direction. Conversely, the process can be visualized as a motion of second phase particles in the negative x-direction with respect to the stationary interface at  $x = 0$ . It is experimentally verified (31,130) that the twin-boundaries in the  $\gamma_1'$ -martensite remain planar as the interface advances. This means that the particle path and the modulus interaction force possess both x and y components.

A martensitic interface separates two phases, a parent phase and a martensite phase, which in general have different elastic moduli. Therefore, modulus misfit parameters take on different values depending on whether the particle is embedded in the parent or in the martensite phase. The modulus interaction force varies within the volume of a particle, the extent of the variation depending on the relative particle

size. Accordingly, one can consider different cases of the interface-particle modulus interaction.

Case 1. Elastic moduli of the parent phase and the martensite are taken to be equal. Also, second-phase particles are considered to be small enough that a variation of the interaction force throughout the particles can be ignored. Figure 36 depicts the modulus interaction force as a function of the  $\beta_1-\gamma_1'$  interface-particle distance for different relative positions of the particle with respect to the periodic structure of the interface. This relative position is specified by a point of intersection of the particle and the interface, as shown in the figure 36(a). To achieve some generality of the solution, the force-distance curves in Figure 36 which are in fact the obstacle profiles, are represented by the corresponding dimensionless parameters,  $F_M D / \mu_o \epsilon_\mu r^3$  and  $x/D$ ,  $r$  is the radius of a spherical particle. Since the interaction force blows up at  $x=0$ , a cut-off radius, equal to the atomic radius, is introduced. On the negative side of the  $x$ -axis, the interaction force,  $F_M D / (\mu_o \epsilon_\mu r^3)$  becomes negative. However, due to the symmetry of the problem, force-distance curves for  $x < 0$  have the same shape as those shown in Figure 36. Intensity of the interaction and details of the obstacle profile, Figure 36, depend significantly on the relative position of the particle, i.e. the particle path with respect to the interface. Since  $F_M D / (\mu_o \epsilon_\mu r^3)$  changes sign at  $x=0$ , there will always be a resisting (and driving) effect of a particle on the moving interface, regardless of the sign of  $\epsilon_\mu$  and the direction of the interface motion. In other words, elastically hard particles,  $\epsilon_\mu > 0$ , will oppose the motion of an approaching interface whereas soft

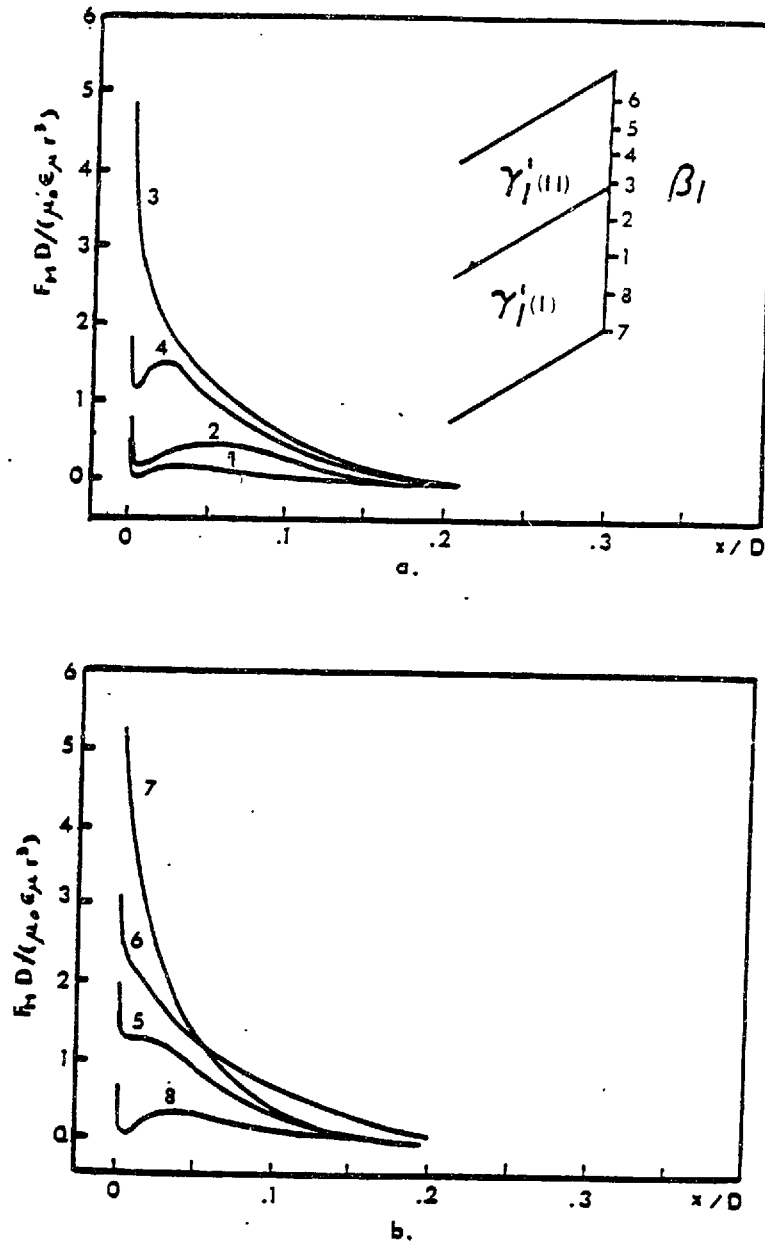


Figure 36 Obstacle profiles corresponding to the modulus interaction between the  $\beta_1$ - $\gamma_1'$  interface and a second-phase particle. Shear elastic moduli of the parent phase and the martensite are taken to be equal. This is the small particle solution which neglects a variation of the interaction force through the particle. Different curves correspond to different paths of the particle, as shown in (a).

particles,  $\epsilon_\mu < 0$ , will impede the motion of a departing interface.

Figure 37 depicts sheared obstacle profiles (Section 2.2.3) corresponding to a modulus interaction of the  $\beta_1-\gamma_1'$  interface and a second phase particle. The sheared profiles are obtained by plotting the interaction force,  $F_M D/(\mu_o \epsilon_\mu r^3)$  versus a width,  $\Delta x/D$ , of the corresponding unsheared profiles from Figure 36. Again, the intensity of interaction is sensitive to the particle path. Yet, the force-distance curves for different paths have the same shape, characteristic of this type of interface-particle interaction.

According to the procedure described in Section 2.2.3, obstacle profiles, both unsheared and sheared, enable a determination of the stress dependence of the activation energy. Figure 38 shows a dimensionless activation energy parameter,  $\Delta G/\mu_o \epsilon_\mu r^3$  plotted against the dimensionless interaction force,  $F_M D/\mu_o \epsilon_\mu r^3$ . Again, it can be concluded that the curves are of the same shape, but the magnitude of the activation energy is very much dependent on the relative position of a particle with respect to the interface. It is expected, therefore, that the particles associated with the highest activation energies will dominate the kinetics of the interface motion.

Case 2. Elastic moduli of the parent phase and the martensite are again taken to be equal. However, the variation of the interaction force within the particle is taken into account. An exact analytical treatment and the corresponding numerical solutions, which involve an integration procedure throughout the particle volume, are complicated and cumbersome. An approximate numerical solution was obtained here by the following procedure: A particle was first divided into 1,000

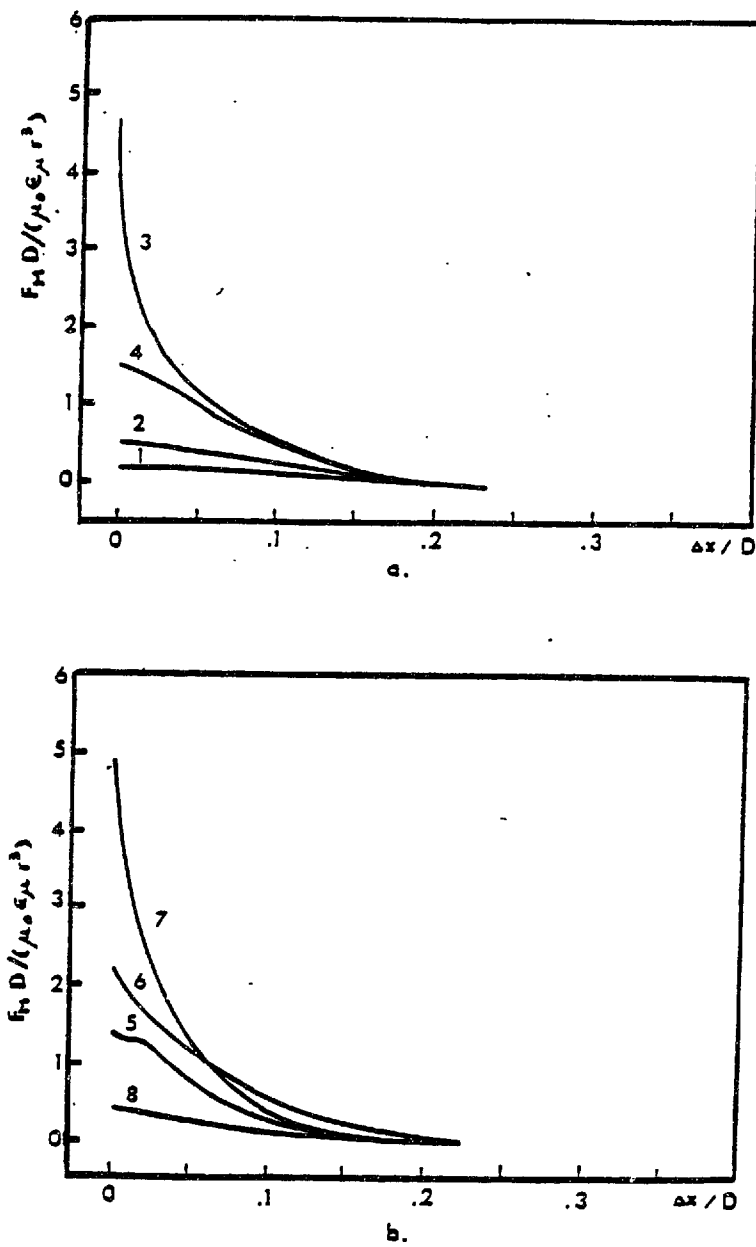


Figure 37 Sheared obstacle profiles corresponding to the unsheared obstacle profiles of figure 36.

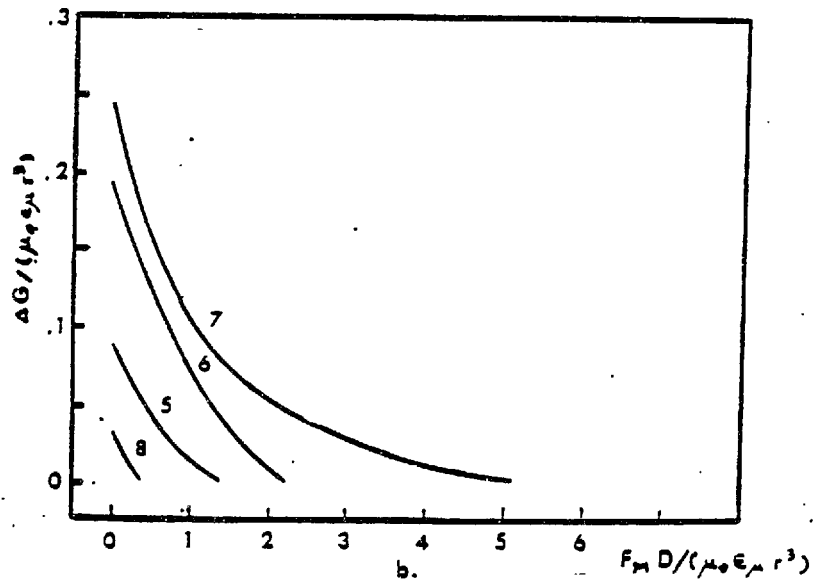
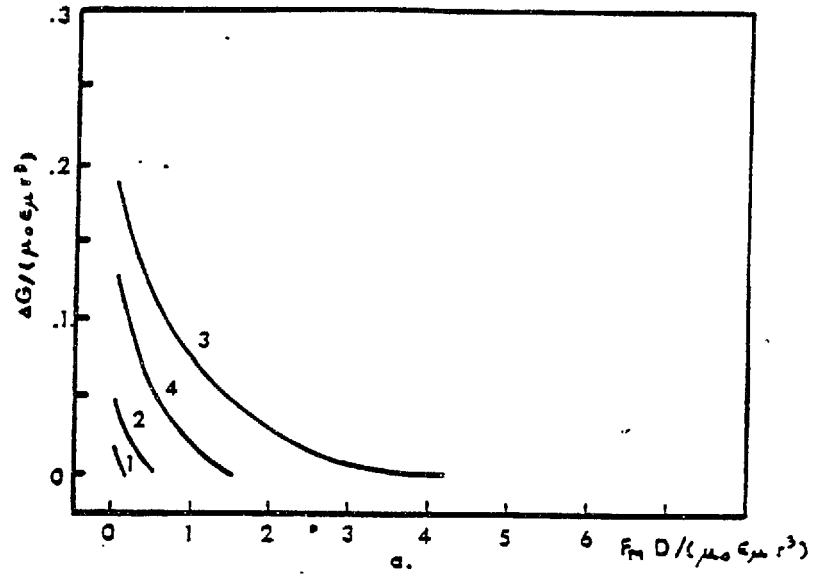


Figure 38 Interaction force dependence of the activation energy corresponding to the obstacle profiles shown in figures 36 and 37. Curve numbers refer to different particle paths, see figure 36(a).

identical elements, and the small-particle solution (case 1) was then applied to each of these elements. The average interaction force between the moving interface and the particle was then obtained by a simple summation over all the particle elements. The effect of this averaging procedure on the obstacle profiles is shown in Figures 39 and 40. Particles with a radius  $D/10$  and  $D$  are considered. The small particle solution, case 1, is also shown for a comparison. A substantial lowering of the maximum of the interaction force, as well as a longer range of interaction is associated with this averaging procedure. Furthermore, obstacle profiles became broader, and the maximum of the interaction force, for the unsheared profiles, is shifted away from the interface.

An activation energy vs. interaction force plot, corresponding to the obstacle profiles of Figures 39 and 40 is shown in Figure 41. For clarity no small particle solution is depicted. It is seen that, except in a range of very low interaction force, the activation energy is reduced due to the averaging procedure. Yet, the characteristic shape of the activation energy vs. interaction force curves is maintained.

Case 3. It is taken that the elastic moduli of the parent phase and the martensite are different. However, the procedure is simplified by ignoring a variation of the interaction force throughout the particle. This case differs from case 1 only in that the  $\epsilon_{\mu}$  takes different values for  $x > 0$  (parent phase) and for  $x < 0$  (martensite phase). Therefore, the dimensionless obstacle profiles (Figures 36 and 37) and corresponding activation energy plots (Figure 38) developed when discussing case 1 can be applied here. The modulus interaction force,  $F_M$ , depends on

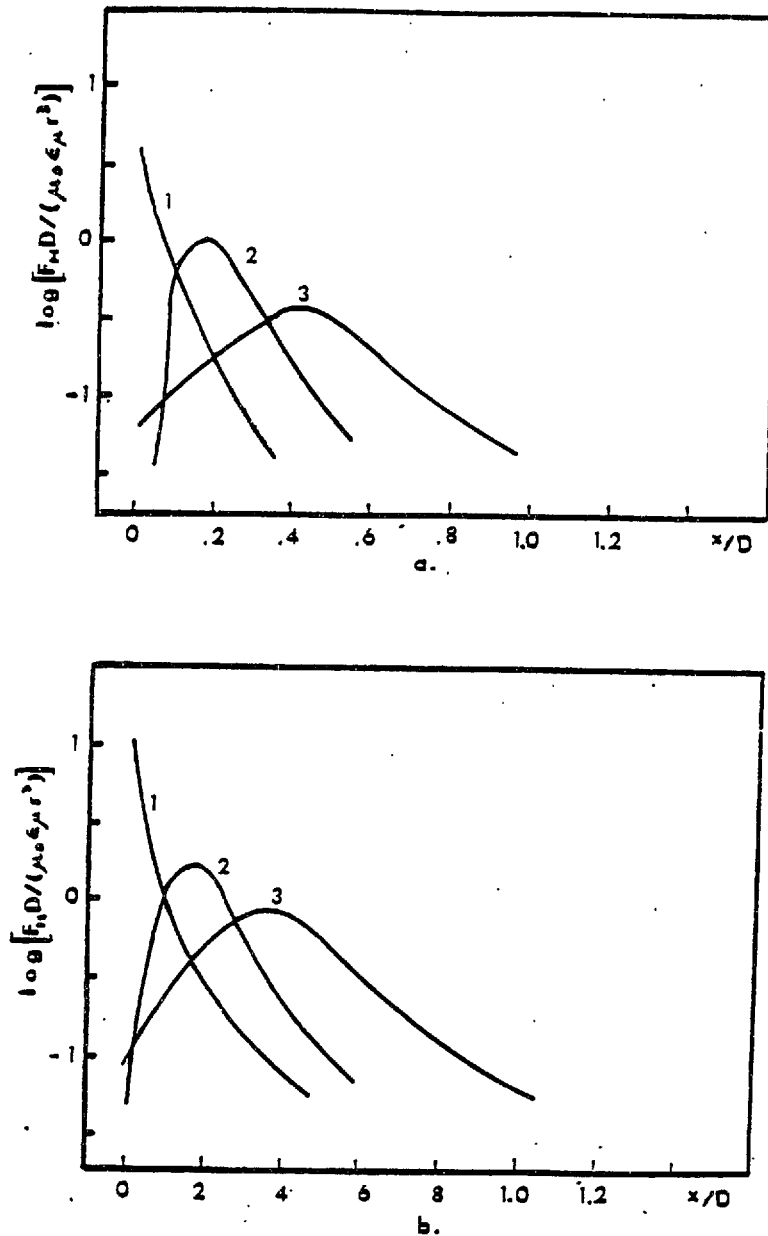


Figure 39 Average obstacle profiles associated with the modulus interaction between the  $\beta_1-\gamma_1'$  interface and a second phase particle: 1-small particle approximation; 2-particle radius equal to  $D/10$ ; 3-particle radius equal to  $D$ . Plot (a) correspond to the particle path 3 and plot (b) to the particle path 7 in figure 36(a). Sheared elastic moduli of the parent phase and the martensite are taken to be equal.



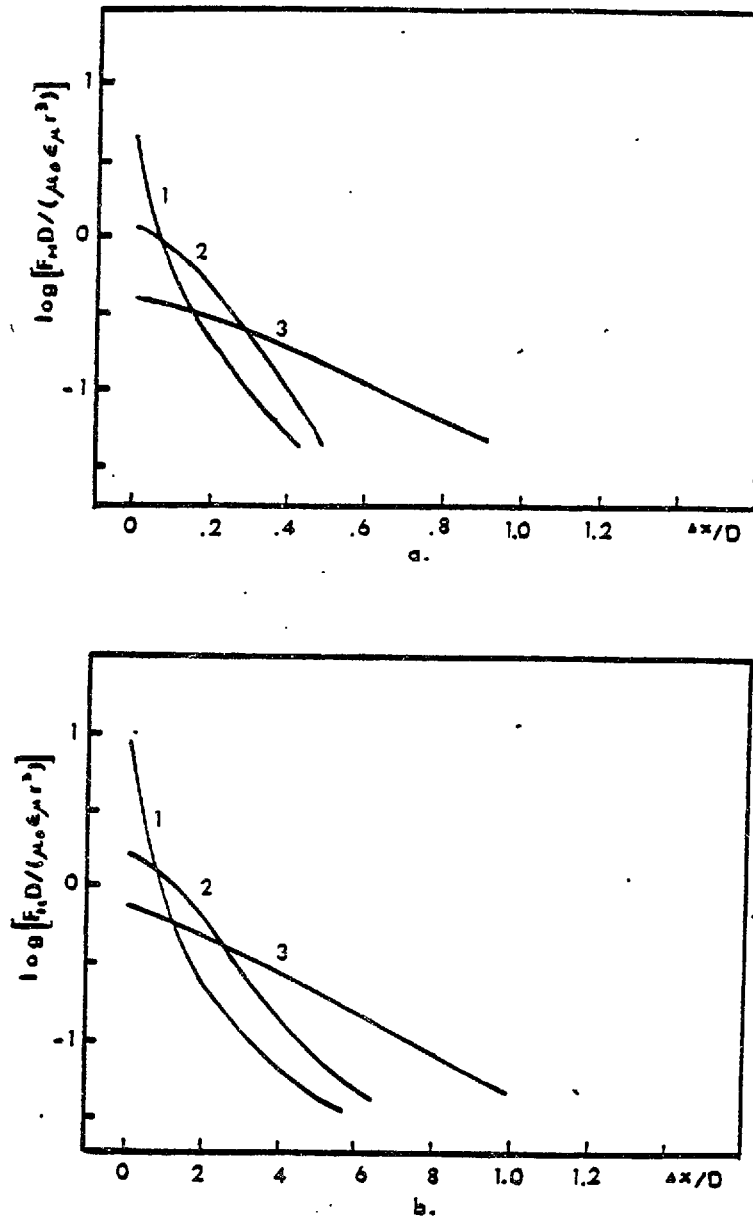


Figure 40 Average sheared obstacle profiles corresponding to the unsheared obstacle profiles shown in figure 39.

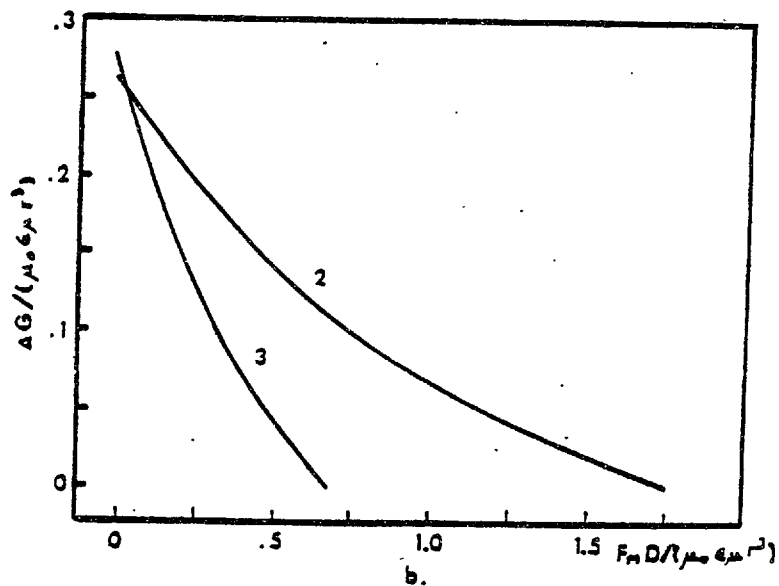
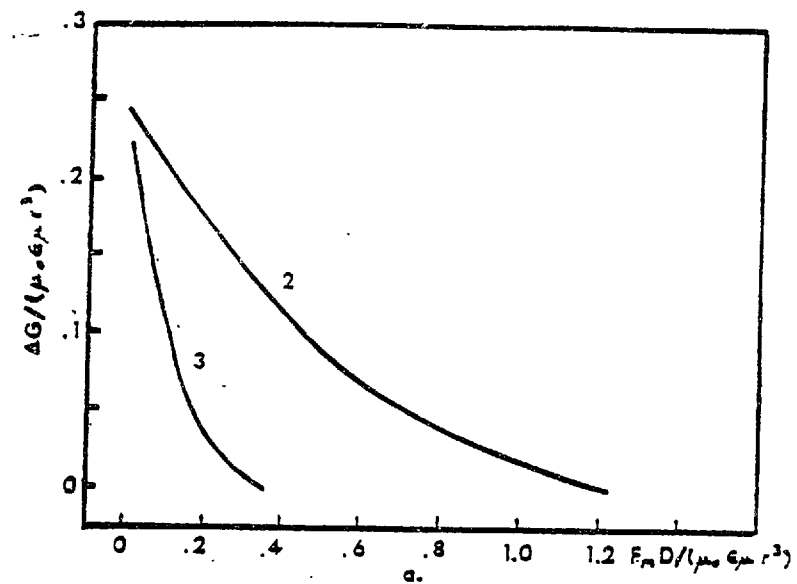


Figure 41 Interaction force dependence of the activation energy corresponding to the obstacle profiles shown in figures 39 and 40. The small particle solution is not depicted.

$\epsilon_{\mu}$ , which may not only have different magnitude, but also different sign for the parent phase and the martensite. Consequently, the intensity and the nature (driving or retarding) of the interface-particle interaction will depend on whether the particle is embedded in the parent or in the martensite-phase. For example, the 2H-type second-phase particles in Cu-Al-Ni alloys, Section 5.5, have the identical structure and consequently the same elastic moduli as  $\gamma_1'$  martensitic phase. There would then be no interface-particle modulus interaction while the 2H-particle is situated in the martensitic phase. The interaction of the interface and a 2H-particle, embedded in the parent phase, on the other hand, is described by Figures 36-38.

Case 4. The last case to be considered takes into account both the modulus mismatch between the parent-phase and the martensite, as well as the variation of the interaction force throughout the particle volume. Only, the specific case of the interaction between the  $\beta_1$ - $\gamma_1'$  interface and a 2H-particle is treated here. Since the elastic moduli of the 2H-phase and the  $\gamma_1'$ -martensite are equal, there is no interaction between the martensitic interface and a 2H-particle which is completely surrounded by martensite. Thus, when a 2H-particle straddles the interface only the part of the particle which resides in the parent  $\beta_1$ -phase interacts with the interface. Figure 42 shows the obstacle profiles associated with 2H-particles with a radius equal to  $D/10$  and  $D$ . Corresponding curves for case 2 are also shown for comparison. A difference occurs only in a region adjacent to the interface where the particle resides partially in both the parent phase and the martensite. Interaction force is slightly increased and the obstacle

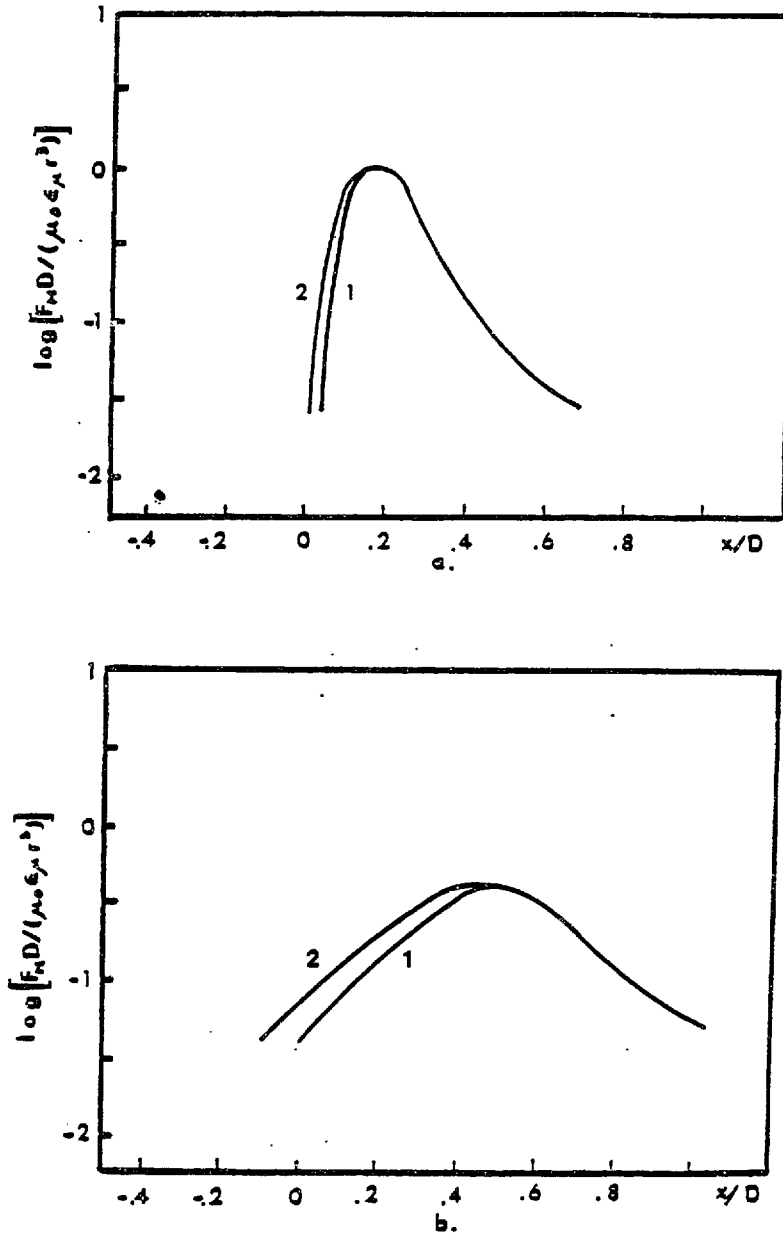


Figure 42 Average obstacle profiles associated with the modulus interaction between the  $\beta_1$ - $\gamma_1'$  interface and a 2H-phase particle with a radius  $D/10$ , (a), and  $D$ , (b). Curves 1 correspond to a solution which takes shear moduli of  $\beta_1$  and  $\gamma_1'$  to be equal. Curves 2 refer to a solution which takes shear moduli of  $\gamma_1'$  and 2H-phase to be equal.

profiles become broader. The same findings hold for the sheared obstacle profiles shown in Figure 43. This leads to an increment in the activation energies, what is shown in Figure 44.

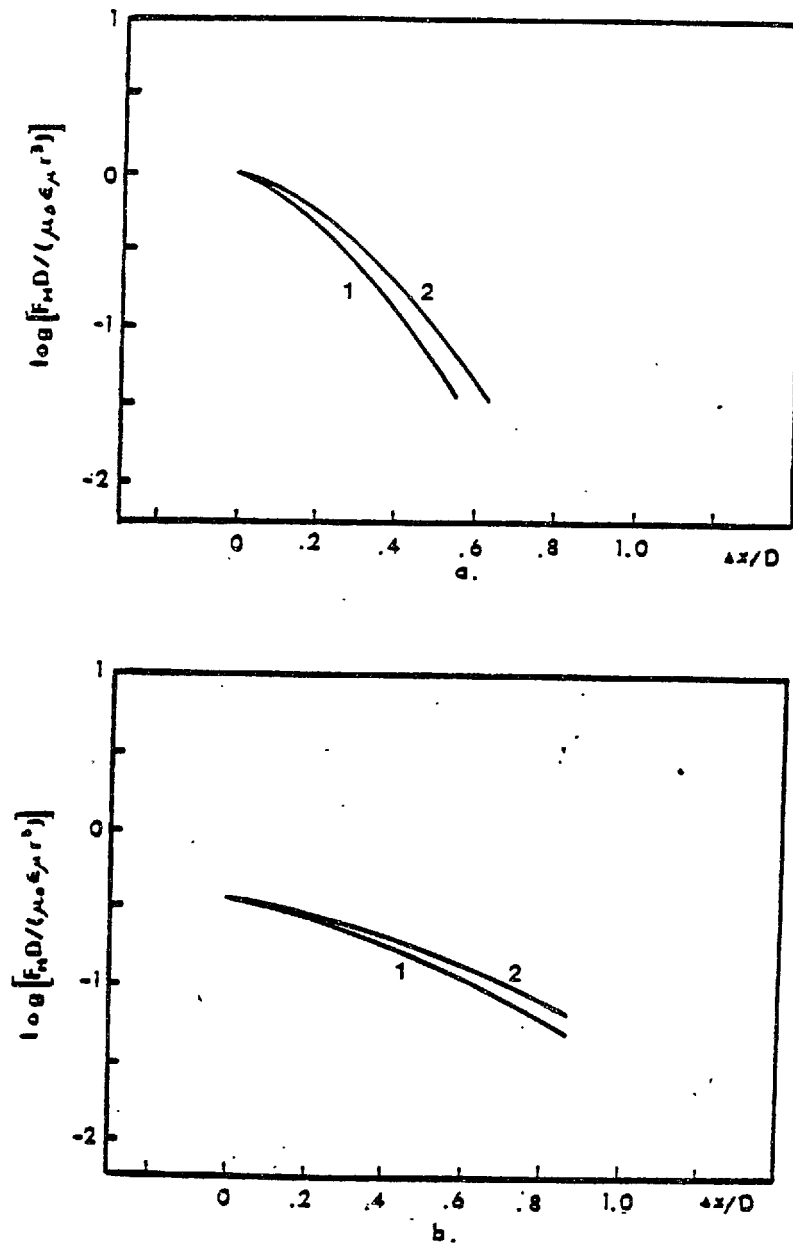


Figure 43 Averaged sheared obstacle profiles corresponding to the unshaded obstacle profiles shown in figure 42.

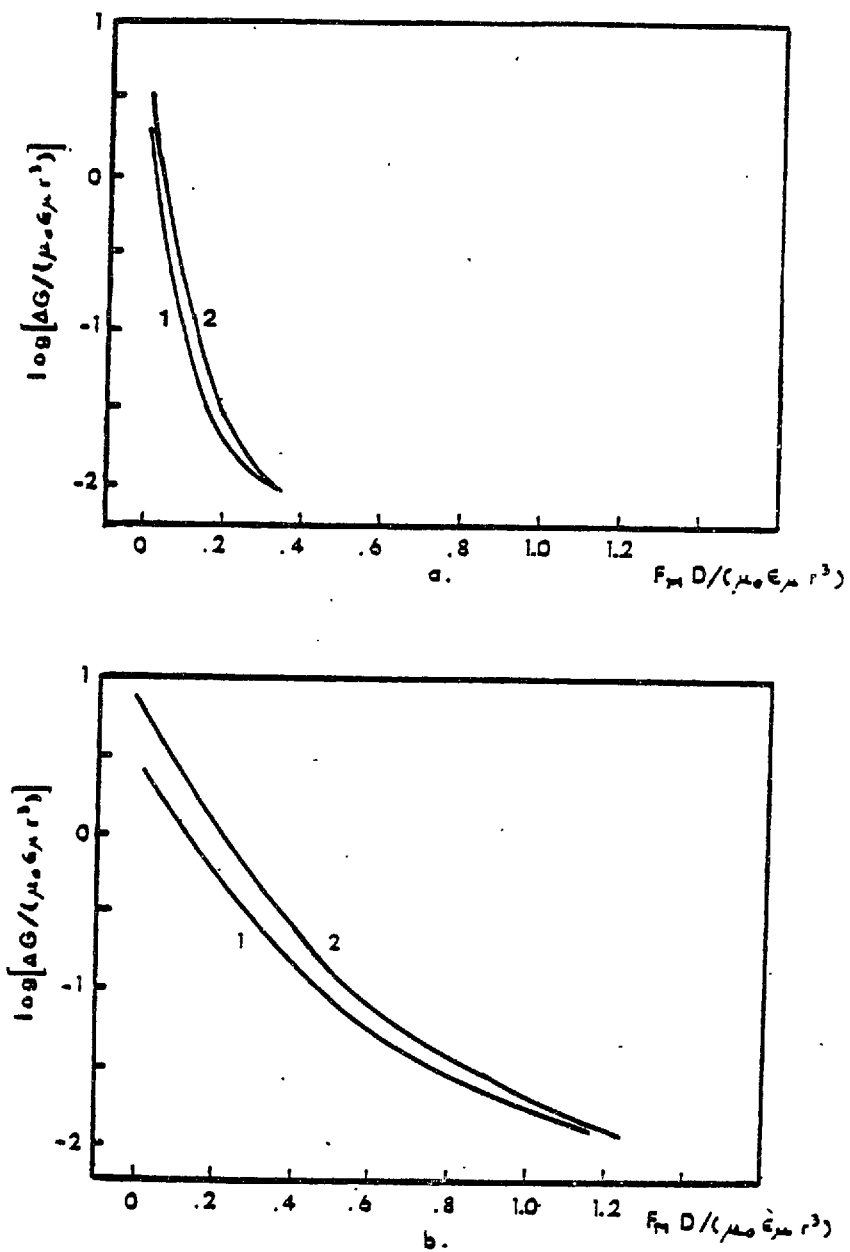


Figure 44 Interaction force dependence of the activation energy associated with the obstacle profiles shown in figures 42 and 43.

### Strain Interaction

An interaction energy between a defect and an elastic inclusion has been defined by Eshelby (131) as:

$$E = - \int_V \sigma_{ij} \epsilon_{ij}^T dV \quad (29)$$

where  $\sigma_{ij}$  = stress field of the defect;  
 $\epsilon_{ij}^T$  = stress free transformation strain of the inclusion,  
 and  
 $V$  = volume of the inclusion.

A strain interaction between an interface and a second-phase particle can be described by equation (29), if the interface is considered to be a defect and the particle is treated as an inclusion. The negative gradient of the interaction energy then defines a strain interaction force,  $F_S$ .  $\epsilon_{ij}^T$  is a symmetrical tensor and in a general case has six different nonzero elements. This makes a general solution for the interface-particle strain interaction very complicated. Therefore, only the strain interaction between a  $\beta_1$ - $\gamma_1'$  interface and  $\gamma$ - and 2H-particles and strain domains, identified in Section 5.5, is considered.

For the  $\gamma$ -phase the transformation strain can be described as a pure dilatation:  $\epsilon_{11}^T = \epsilon_{22}^T = \epsilon_{33}^T \neq 0$ . It is readily verified that the total strain interaction force between the interface and a  $\gamma$ -particle is zero, for reasons of symmetry.

$\epsilon_{ij}^T$  for the internally twinned 2H-particles, as discussed in Section 5.5, can be considered as an IPS, with the invariant plane near  $\{331\}_{\beta_1}$ . There are thus twelve equivalent variants of the 2H-particles,



and as many  $\epsilon_{ij}^T$ 's, when referred to the parent phase. If the structure of the 2H-phase is fixed and unaffected by the martensitic transformation, then for each variant of 2H-phase, the form of  $\epsilon_{ij}^T$  will depend on whether the particle is surrounded by the parent phase or by the martensite. A relation between the two forms of  $\epsilon_{ij}^T$ , for each 2H-variant, is dependent on the relative particle size with respect to the periodicity of the interface structure.

For small particles, it is the martensitic lattice deformation,  $\underline{S}$ , that relates two forms of  $\epsilon_{ij}^T$  for each variant of the second phase particles. When the particle size is comparable with the periodicity of the interface structure, two  $\epsilon_{ij}^T$ 's are related by  $\underline{E}$ . In any case, if the 2H-phase is not affected by the martensitic transformation, the strain interaction between the martensitic interface and 2H-particles will depend upon the structure of the surrounding matrix. In other words, the strain interaction for the forward motion of the interface will differ from the interaction associated with the reverse motion of the interface. The same argument holds when the 2H-phase undergoes a transformation different from the martensitic transformation. A detailed derivation of the strain interaction force,  $F_S$ , between the  $\beta_1-\gamma_1'$  interface and a 2H-particle is presented in Appendix C. Calculation done here involved all twelve variants of the 2H-phase and eight characteristic particle paths. The effect of different  $\epsilon_{ij}^T$ , for a 2H-particle embedded in martensite on the strain interaction was also investigated. The variation of the interaction force throughout the particle was accounted for by the averaging procedure described in the previous section. Only some of the characteristic results which

demonstrate effects of the transformation variants, particle path, etc., are presented here.

Figure 45 shows the obstacle profiles associated with the strain interaction between the  $\beta_1-\gamma_1'$  interface and different variants of the 2H-phase for a fixed particle path. The strain interaction force is expressed by a dimensionless parameter,  $F_S \cdot D / (\mu_0 \cdot r^3)$ . The same  $\epsilon_{ij}^T$  was taken for both the positive and the negative side of the x-axis, in order to simplify the calculation. Obviously, different variants of the 2H-phase give rise to different obstacle profiles. The curves are asymmetric, with respect to the position of the interface,  $x=0$ , and contain either a very steep upheaval or a very steep valley. Also, there are some subsidiary maxima and minima on the force-distance curves but they correspond to considerably smaller magnitudes of the interaction force. This means that some of the variants of the 2H-phase will become strong obstacles to the interface motion in the forward direction, whereas the other variants will strongly impede the motion of the interface in the reverse direction.

Figure 46 shows an effect of the particle path on the obstacle profile for the variant 3 of the 2H-phase. The magnitude of the interaction force as well as the position of its maximum with respect to the interface are sensitive to the particle path. However, the general shape of the curves is preserved.

Obstacle profiles correspond to different transformation strains,  $\epsilon_{ij}^T$ , for a 2H-particle completely embedded in the martensite are shown in Figure 47.  $\epsilon_{ij}^T$  was taken to have either the same form in both parent phase and martensite (curve 1), or to be modified by the

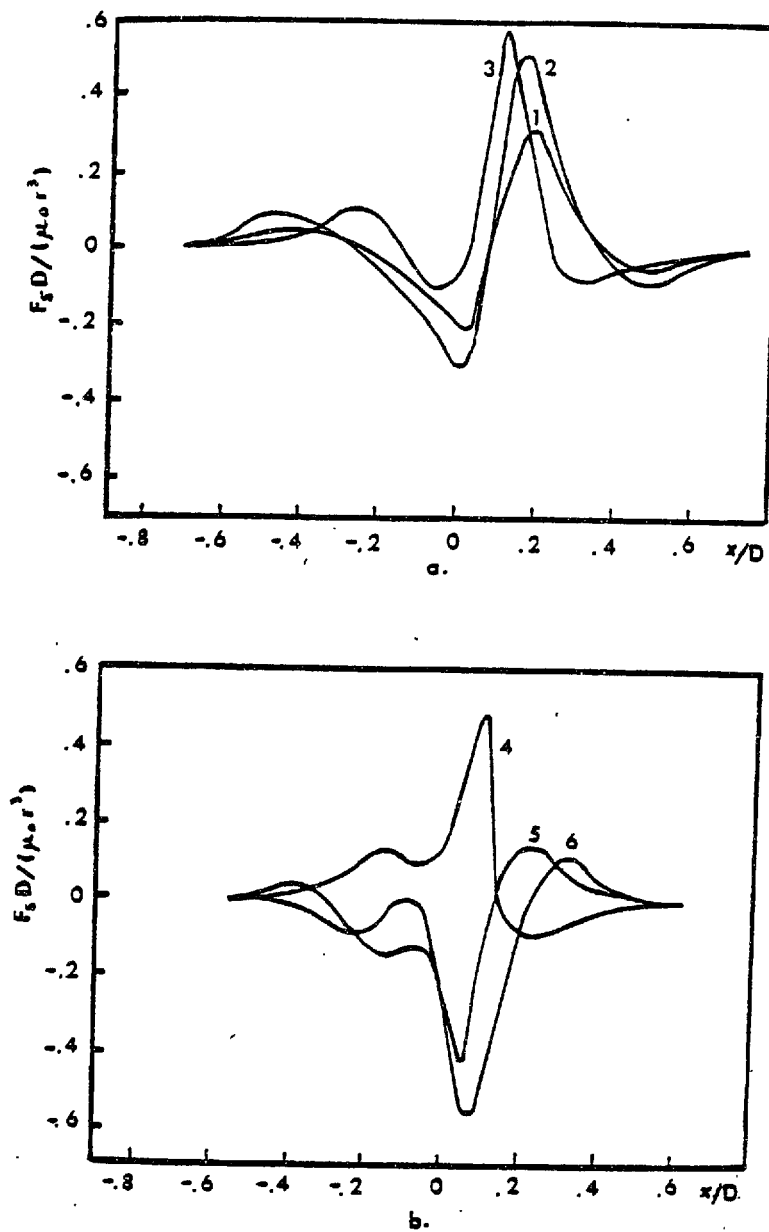


(Figure 45)

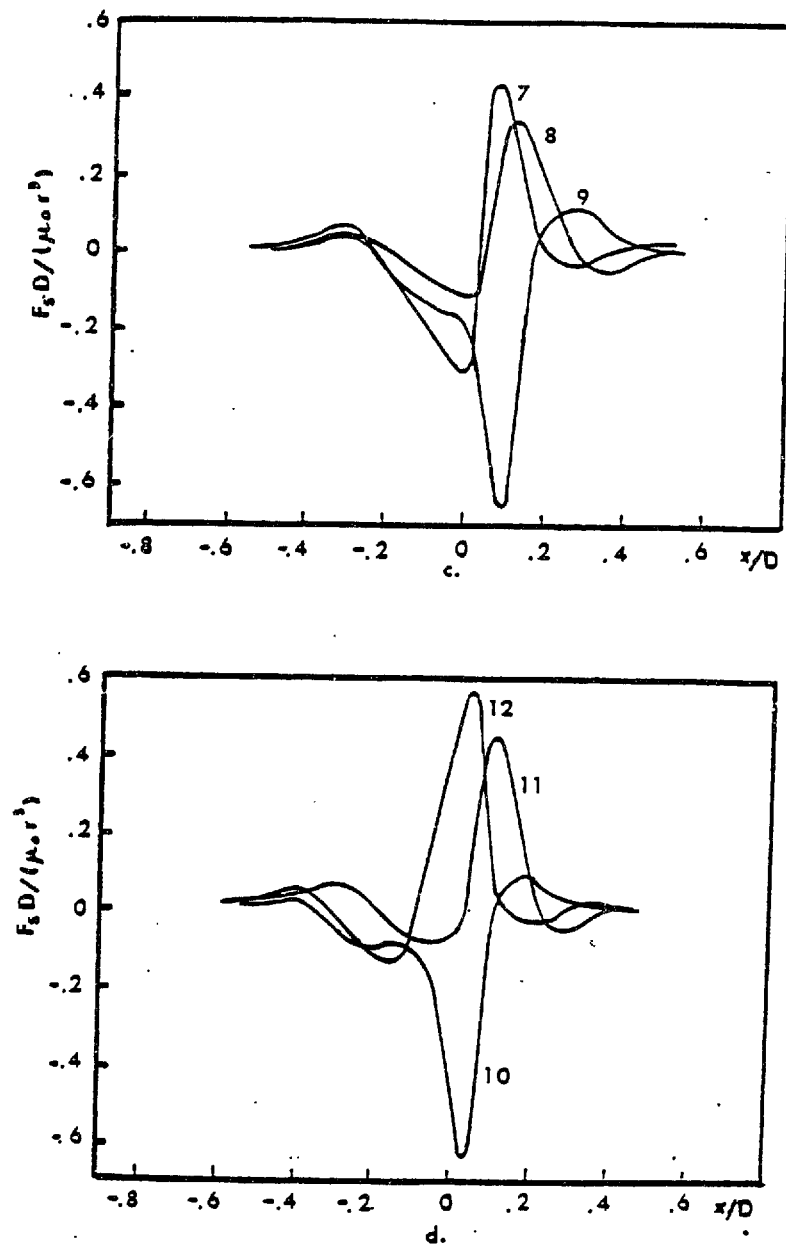


Figure 45 Obstacle profiles associated with the strain interaction between the  $\beta_1$ - $\gamma_1'$  interface and a 2H-phase particle. Curve numbers refer to different transformation variants of the 2H-phase. It was assumed that  $\epsilon_{ij}^1$  is the same at both sides of the interface.

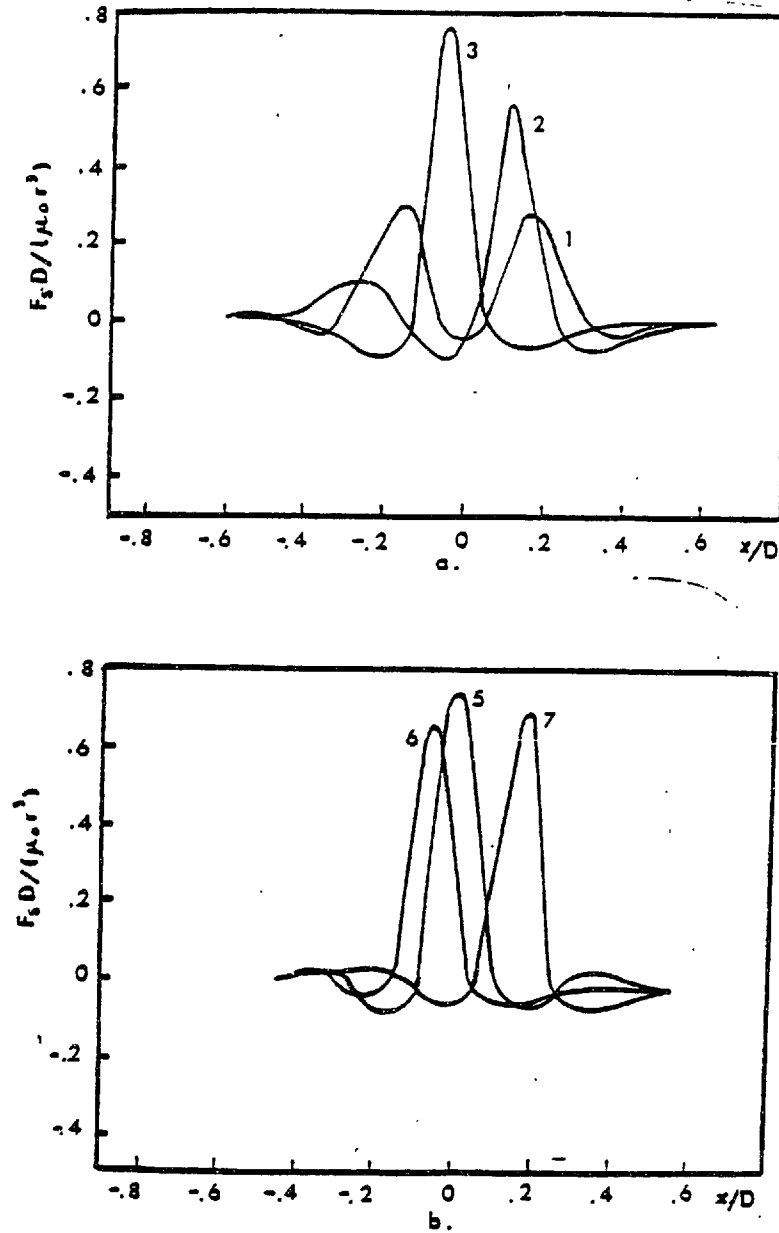


Figure 46 Effect of the particle path on the obstacle profile associated with the strain interaction between the  $\beta_1-\gamma_1'$  interface and a 2H-particle (variant 3).  $\epsilon_{ij}$  is assumed to be equal on both sides of the interface. Curve numbers refer to different particle paths, see figure 36(a) for indexing.

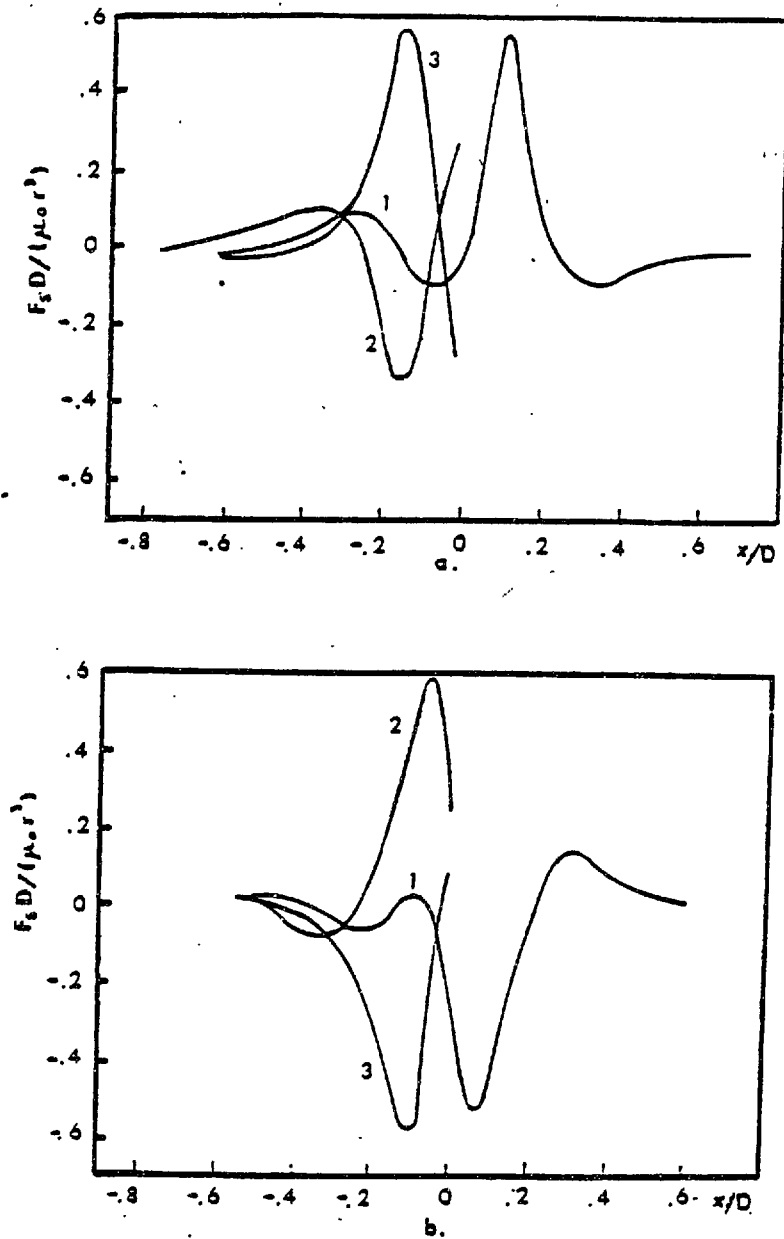


Figure 47 Obstacle profiles associated with strain interaction between the  $\beta_1-\gamma_1'$  interface and a 2H-particle variant 3, (a), and variant 6, (b). Curve numbers refer to different  $\epsilon_{ij}$ 's on the negative side of the x-axis: 1- $\epsilon_{ij}$  is equal on both sides of the x-axis; 2- and 3-  $\epsilon_{ij}$  at the negative side of the x-axis is modified by  $S_{ij}$  and  $E_{ij}$ , respectively.

martensitic lattice deformation,  $\underline{S}$  (curve 2), or by the macroscopic shape change  $\underline{E}$  (curve 3). It is seen that  $\epsilon_{ij}^T$  can affect not only the magnitude but also the sign of the interaction force. Some variants, depending on a choice of the  $\epsilon_{ij}^T$ , can give rise to a pair of obstacles. This pair of obstacles is often strong only in one direction of the interface motion and becomes substantially weaker for the reverse direction. Figure 48 shows the effect of particle size on both the unsheared and sheared obstacle profiles.  $\epsilon_{ij}^T$  was taken to be the same on both sides of the x-axis. Larger particles, obviously, give rise to smaller values of  $F_S \cdot D / (\mu_0 r^3)$  and a longer range of interaction. The effect of particle size on the activation energy is shown in Figure 49.

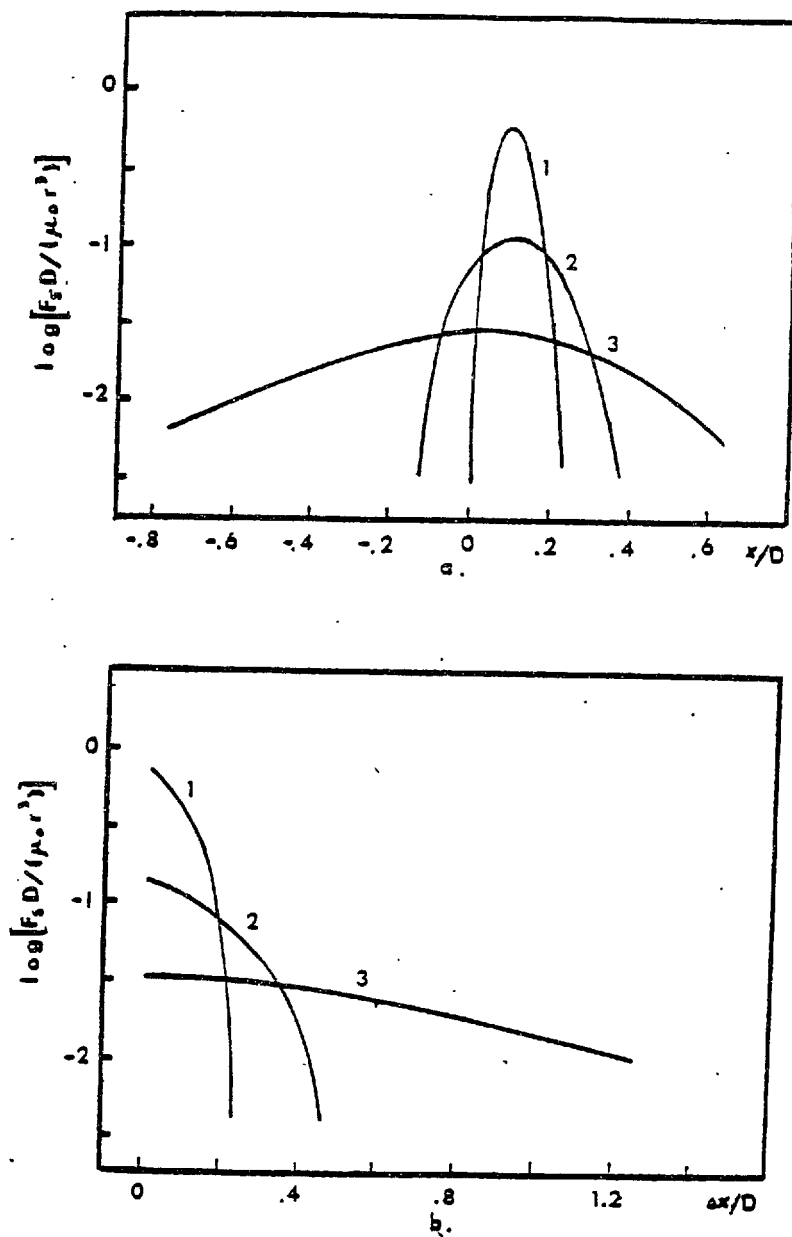


Figure 48 Average obstacle profiles, (a), and average sheared obstacle profiles, (b), associated with the strain interaction between the  $\beta_1-\gamma_1'$  interface and a 2H-particle, variant 3. Curve numbers refer to different particle size: 1- small particle solution; 2- and 3- particle radius equal to  $D/10$  and  $D$ , respectively.



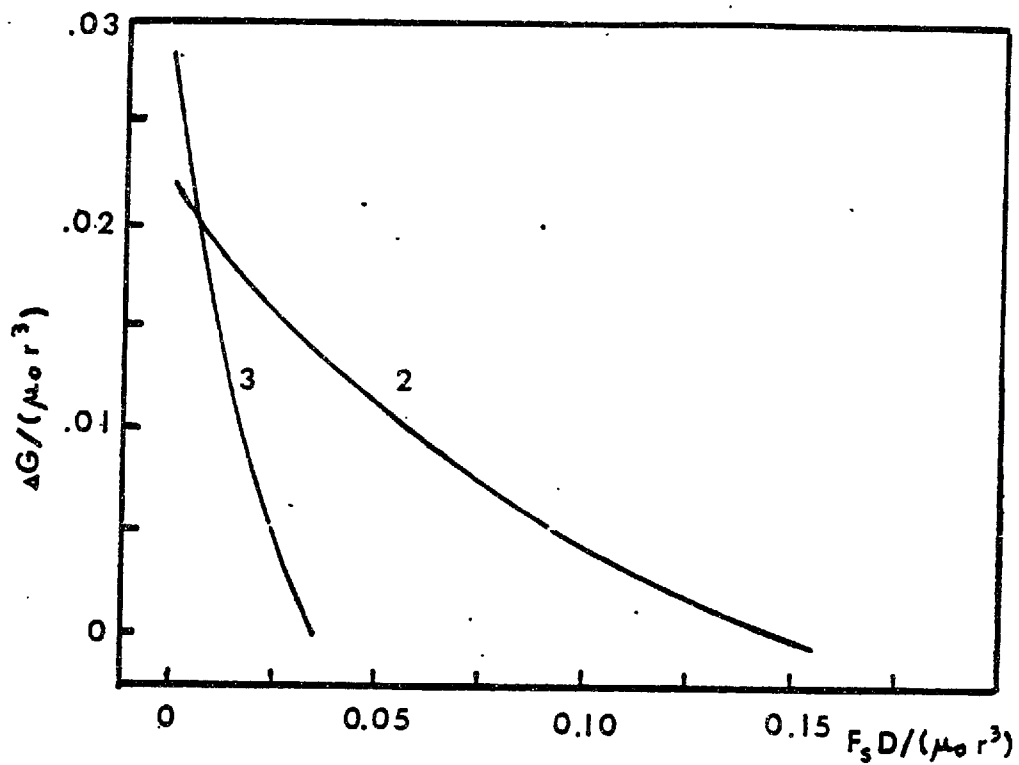


Figure 49 Interaction force dependence of the activation energy associated with the obstacle profiles shown in figure 48. The small particle solution is not plotted.

### 6.4.2 Short-range interactions

Various kinds of interactions can occur when a particle comes into contact with a moving interface. The internal structure of the interface and its microtopographical features are now expected to play an important role. Interaction involves a highly disturbed region of the core of the interface dislocations. Linear elastic calculations, similar to those applied to the long-range interactions, are no longer valid. Consequently, use should be made of nonlinear elasticity and high-order elastic constants. This makes a quantitative analysis of the short-range interactions between an interface and a particle very complicated. Only some simple quantitative models of the short-range interactions will be considered.

Interaction of an interface with a particle gives rise to structural and morphological changes of the particle and/or the interface. The negative gradient of the ensuing energy change then defines the short-range interaction force,  $F_{SR}$ . Some types of short-range interactions are associated with an energy change which is recoverable during reverse motion of the interface. When referred to the transformational hysteresis, Figure 3, these interactions affect  $\tau_0$  rather than the height of the hysteresis, i.e. the friction stress,  $\tau_f$ . Therefore, they should be excluded from an analysis of the rate controlling mechanism of the interface motion, at least for the reversible martensitic transformations, as is the case at hand.

### Structure and Shape Change of Particle

An interface separates two structures related by a lattice deformation,  $\underline{S}$ , and a macroscopic shape change,  $\underline{E}$ . As the interface advances,

it propagates both  $\underline{S}$  and  $\underline{E}$ . Depending on its structure, size, etc., a particle may or may not undergo either  $\underline{E}$  or  $\underline{S}$  or some related transformation, when it comes into contact with the interface. However, any of these transformations is expected to be reversible, and the particle will be converted back to its original structure and shape during the reverse motion of the martensitic interface. This type of short-range interaction thus does not affect the height of the transformation hysteresis, Figure 3, and will not be considered further. It should be noticed, however, that a temporary change of structure and shape of a particle may affect its long-range interaction with the interface, as discussed in Section 6.4.1.

#### Lattice friction stress change

Consider the case when the moving martensitic interface penetrates second phase particles, which then undergo some transformation, not necessarily  $\underline{S}$  or  $\underline{E}$ . Portions of the interface penetrating the particles will experience a different Peierls stress than will the portions outside the particles. A force corresponding to this type of interaction between an interface and a spherical particle is found to be:

$$F_{SR} = \Delta\tau \cdot \pi \cdot (2rx - x^2) \quad (30)$$

The corresponding obstacle profile is shown in Figure 50. The maximum of the interaction force is governed by the difference in the lattice friction stress,  $\Delta\tau$ , and by the particle size. The range of interaction, on the other hand, is equal to the particle size.

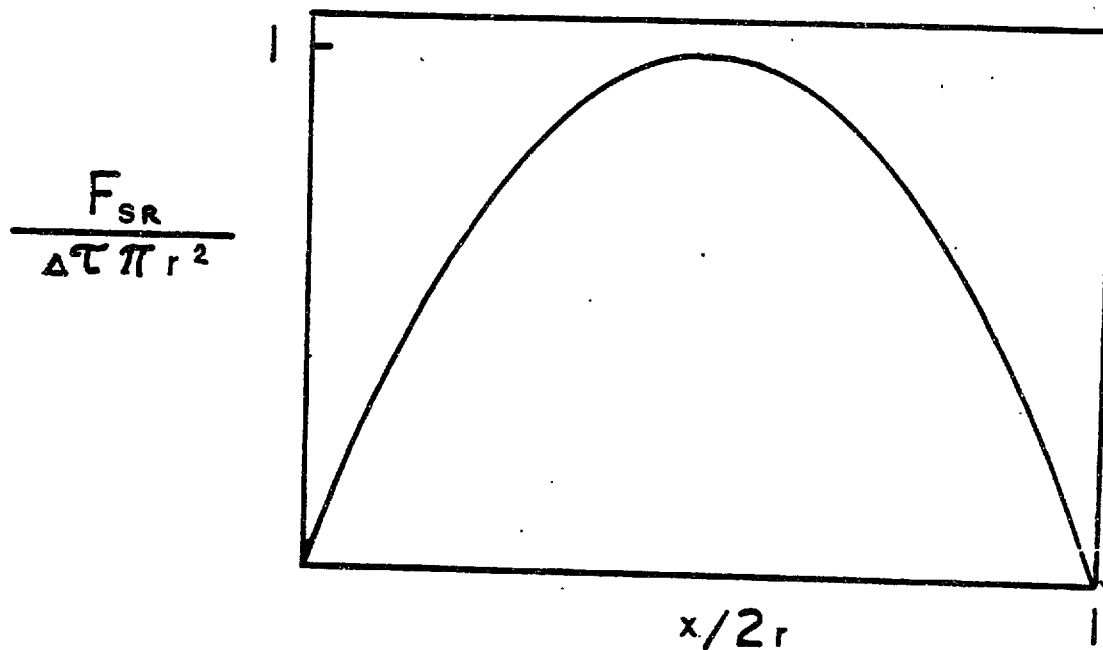


Figure 50 Obstacle profiles associated with the short-range interaction between an interface and a second-phase particle with different lattice friction stress,  $\Delta\tau$ .

### Interfacial Energy Change

The energy of an interface is dominated by the core energy of the interface dislocations. The dislocation core is a highly perturbed region and its energy is dependent on higher order elastic constants. This makes an exact calculation of the interfacial energy difficult, and only some rough estimates exist. Nevertheless, it is expected that the interfacial energy may vary considerably from one system to another. This means that when an interface penetrates a second phase particle, portions of the interface inside and outside the particle will have, in general, different surface energies. In a limiting case when the interface does not penetrate the particle, this energy difference,  $\Delta\gamma$ , becomes equal to the interface energy. This problem has already been treated, by Zener (132), for grain boundary migration. A force corresponding to this type of interaction between an interface and a spherical particle is found to be

$$F_{SR} = 2\pi\Delta\gamma (r-x) \quad . \quad (31)$$

The corresponding obstacle profile is shown in Figure 51. The shape of this profile is found to be very sensitive to the particle shape and its orientation with respect to the interface. For example, a particle of a cuboidal shape, with a face parallel to the interface, gives rise to an obstacle profile containing only two  $\delta$ -functions at  $x = 0$  and  $x = 2 \cdot r$ .

Figure 52 shows a plot of the activation energy versus the interaction force for a Zener type of interaction between a spherical particle and an interface.

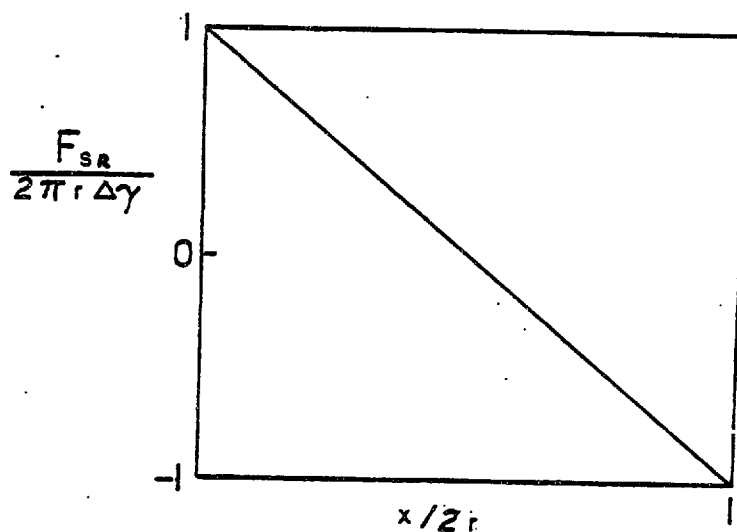


Figure 51 Obstacle profile associated with an interface energy change attending the short-range interaction between an interface and a particle.

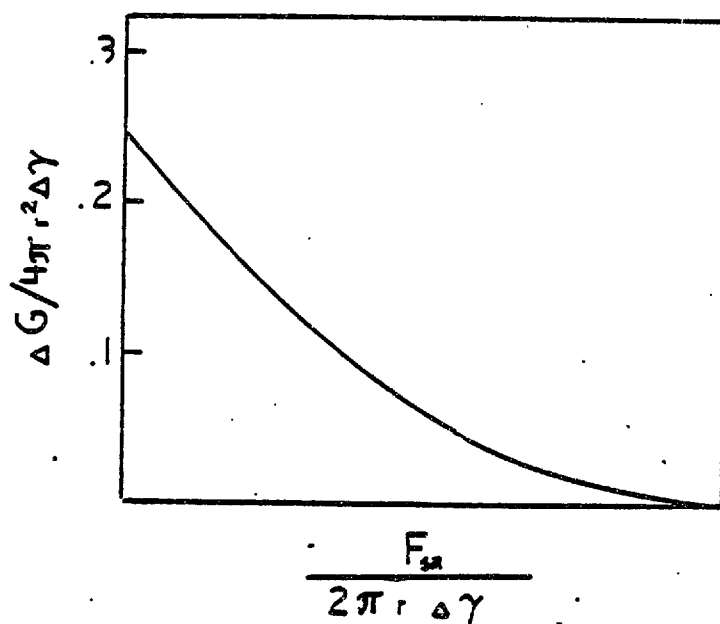


Figure 52 Interaction force dependence of the activation energy for the obstacle profile shown in figure 51.

### 6.4.3. Derivation of driving force-activation volume relations.

The analysis presented so far in this section involved different interactions between a planar interface and a single second-phase particle. The analysis yielded an interaction force exerted by the particle on the interface and its variation with interface-particle distance. To find the total interaction force on an interface, which interacts with a population of second-phase particles, a superposition should be made over all the particles within the range of interaction. A simplified analysis of the interaction of an interface with regularly distributed second-phase particles is shown in Figure 53. The particles are approximated as lying on the corners of a square grid, the edge length of which is equal to the average planar particle spacing,  $\ell$ . The frictional interaction force per area is then obtained by dividing the interaction force by  $\ell^2$ . With respect to Figure 53, the critical thermally activated event corresponds to the interface overcoming the central particle with the assistance of the applied driving force. The interface is allowed to bow out, as sketched, to transmit the applied load to the particle. However, the surface tension of the interface (as discussed in section 6.2) is assumed to guarantee relatively small curvature of the interface. The volume of the critical configuration, the true activation volume, can therefore be approximated by the volume of a square pyramid of the basal area  $2\ell^2$  with a height equal to the stress dependent activation distance,  $\Delta X$ .

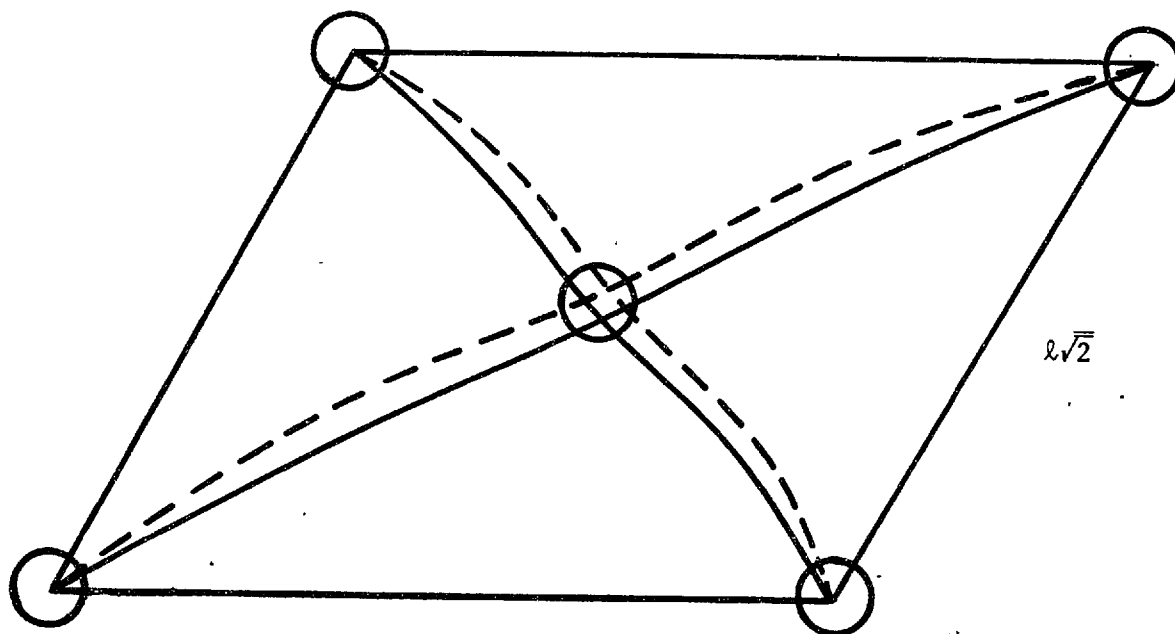


Figure 53 Schematic representation of the critical event of an interaction between an interface and regularly distributed second phase particles, the average planar spacing of which is  $l$ .



## 7. DISCUSSION

### 7.1 Comparison of Model and Experimental Results

In chapters 4 and 5, the measured mobility of the  $\beta_1-\gamma_1'$  martensitic interface in thermoelastic CuAlNi alloys was described. Obstacle profiles and corresponding plots of activation energy versus friction stress were constructed. When discussed in terms of the theory of thermally-activated slip, the experimental results were attributed to a rate controlling interaction of the moving  $\beta_1-\gamma_1'$  interface with discrete second-phase particles. Subsequent TEM examination revealed the presence of various precipitates, identified as  $\gamma$ -phase and 2H-phase.

In Chapter 6 different possible mechanisms of interaction between a  $\beta_1-\gamma_1'$  interface and a second phase particle were modelled in more general terms. It was shown that a number of parameters, which vary from one system to another, can affect substantially both the intensity and the nature of interface-particle interactions.

In this section a quantitative comparison is made between the measured mobilities of the  $\beta_1-\gamma_1'$  interface and those predicted by the models. This includes a use of some quantities (shear modulus, particle radius, etc.), measured in this work, as well as an estimation of others (interface energy, lattice friction stress, etc.) on the basis of available literature data.

Analysis of the interface-particle interaction is simplified by assuming a uniform distribution of particles, with a spacing equal to the average planar particle spacing,  $\lambda$ . An interface segment is

visualized to interact with five particles, four of them situated at the corners of a square with edge length  $\ell\sqrt{2}$  and the fifth particle in the center. The critical event of the interface motion then corresponds to a surmounting of the center particle. The volume of the atomic configuration participating in this critical event, the true activation volume, can be approximated by the volume of the corresponding square pyramid, the height of which is equal to the interaction force (stress) dependent activation distance. Obviously the critical atomic configuration is three-dimensional in character, as opposed to the corresponding two-dimensional configuration of a line dislocation. It is therefore expected that a surface dislocation is associated with larger activation volumes than a line dislocation when interacting with a given obstacle.

An interaction force between an obstacle and the interface is simply converted into a friction stress by dividing it by  $\ell^2$ . The friction stress is then converted into the corresponding volume driving force applying the procedure described in Section 5.4.

The isotropic shear modulus of the  $\beta_1$ -phase is taken to be  $5 \cdot 10^{10}$  N/m<sup>2</sup> and the period of the interface structure,  $D$ , is estimated to be 50 nm (124,133-134).

### 7.1.1 $\gamma$ -phase precipitates

The interaction forces between a  $\gamma$ -phase particle, of the size observed in Section 5.5.3, and the  $\beta_1$ - $\gamma_1'$  interface were computed for different short- and long-range interactions, using the models derived in Section 6.4. The coarse scale precipitation of the  $\gamma$ -phase gives rise to very broad obstacle profiles. In the range of measured activation

volumes, Figure 12, the obstacle profiles associated with the  $\gamma$ -phase predicted by the models have very low slopes. Activation volumes in this region arise from obstacle profiles close to their maxima. Consequently, the concept of rate control by thermal activation may not be appropriate for these obstacles. Furthermore very high values of activation energy, estimated to be a few hundred electron volts, were associated with these obstacles. Thus, it is concluded that the  $\gamma$ -phase particles, when they impede the interface motion, can only contribute to the athermal part of the friction stress and driving force ( $\Delta g_{\mu}/\mu_0 = 3 \cdot 10^{-5} - 4.4 \cdot 10^{-5}$ ). Since the transformational strain of the  $\gamma$ -phase is a pure dilation, there is no strain interaction between the interface and a  $\gamma$ -particle. Other possible interface-particle interactions can individually account for the measured athermal driving force if the following estimates are taken:  $\epsilon_{\mu} = 2.4$  for the modulus interaction;  $\Delta \tau = 0.12 \mu_0$  for the lattice friction stress change interaction, and  $\Delta \gamma = 6 \cdot 10^4 \text{ mJ/m}^2$  for the interfacial energy change interaction. All these values are unreasonably high so that even superposition of these interaction mechanisms for the  $\gamma$ -particles can provide at best a minor contribution to the measured athermal driving force.

### 7.1.2. 2H-phase precipitates

The interaction forces between the  $\beta_1 - \gamma_1'$  interface and 2H-phase were computed for different types of interaction, and for both particle sizes, observed in Section 5.5.4. Again it was found that the 2H-particles are associated with very broad obstacle profiles, which rules them out as the rate controlling thermal obstacles. The 2H-particles are thus considered as contributing primarily to the athermal component. The

strain interaction between the interface and the 2H-particles of radii 10 nm and 75 nm, using the model from Section 6.4.2, is associated with an athermal driving force  $\Delta g_{\mu}/\mu_0 = 9 \cdot 10^{-5}$  and  $1.4 \cdot 10^{-4}$  respectively. This good agreement between the model predictions for the strain interaction and the measured athermal driving force  $\Delta g_{\mu}/\mu_0 = 3 \cdot 10^{-5} - 4.4 \cdot 10^{-5}$ , can be improved by increasing the effective particle spacing used in the computation of the driving force. This correction seems to be justified since the model solution used referred to the interface-particle interaction associated with the strongest interaction. Of course, only a fraction of the 2H-particles observed is associated with this strong interaction, and their spacing is larger than the average particle spacing used. For the modulus misfit interaction an estimate  $\epsilon_{\mu} = 0.18$  was first made, by assuming that the 2H-phase has the same isotropic shear modulus as the  $\gamma_1'$  phase (135). The model for the modulus interaction then predicts  $\Delta g_{\mu}/\mu_0 = 4.2 \cdot 10^{-5} - 1.5 \cdot 10^{-4}$ . With the correction for the particle spacing these values could be made to agree even better with the measured ones. The lattice friction stress change interaction could individually account for the measured athermal driving force if  $\Delta\tau \approx 10^{-2} \mu_0$ . In the same way the interfacial energy change interaction can have a major contribution to the measured  $\Delta g_{\mu}/\mu_0$  only for  $\Delta\gamma = 5 \cdot 10^2 - 5 \cdot 10^3 \text{ mJ/m}^2$ , depending on the particle size. These values of  $\Delta\tau$  and  $\Delta\gamma$  are unreasonably high, and the corresponding short-range interface-particle interactions can have only a minor contribution to the measured athermal driving force. This means that the measured athermal behavior arises primarily from the strain and the modulus interaction between the interface and 2H-phase particles.

### 7.1.3 Tweed structure

As discussed in Section 5.5.5, the tweed structure has been attributed to domains of lattice distortion which are distributed regularly throughout the crystal. In some models these domains are envisaged to form a continuous periodic modulation in lattice distortion. Interaction of a moving interface with these strain modulations can be treated in a similar way to that used to describe the age-hardening phenomenon in spinodally modulated alloys (136-138). Quantitative analysis of this type of interaction is very complicated and is not dealt with here. It is interesting to note, however, that the special case of unidirectional strain modulations normal to the interface is analogous to the Peierls type of interaction, Section 6.2, with appropriate modification of the energy amplitude and periodicity. An alternative treatment of the interaction of the tweed structure with the moving interface is adopted here. The tweed structure is modelled as fine scale precipitation. Two different cases are considered: (i) strain domains with tetragonal distortion,  $\epsilon_{33}^T \neq 0$ , parallel to one of the cube axes; and (ii) coherent 2H-phase precipitates, both with particle spacing 15 nm. The models for interface-particle interaction, referring to the small particle approximation, Section 6.4, are used here.

As shown in Section 6.4, the modulus interaction force depends on  $\epsilon_{\mu} \cdot r^3$  or  $\epsilon_{\mu} \cdot V_p$ , where  $V_p$  is the volume of the interacting particle. The best agreement between the single modulus interaction and the measured behavior is obtained by setting  $\epsilon_{\mu} \cdot V_p = 6 \cdot 10^{-27} \text{ m}^3$ , Figure 54. If the tweed strain domains are considered to be related to clustering of quenched-in vacancies (122), then an upper limit can be set for  $\epsilon_{\mu} = -1$ . This then

requires a domain size of 480 atomic volumes to account for  $\epsilon_{\mu} V_p$ . A similar analysis for the tweed domains treated as the 2H-phase, with  $\epsilon_{\mu} = 0.18$ , requires a domain size of 2700 atomic volumes.

The strain interaction for domains of tetragonal distortion depends on  $\epsilon_{33} V_p$  and the best agreement with the measured obstacle profile is obtained for  $\epsilon_{33} V_p = 7 \cdot 10^{-28} \text{ m}^3$ . The domain size suggested by the single modulus interaction,  $V_p = 480\text{-}2700\Omega$ , is associated with quite reasonable values of  $\epsilon_{33} = 0.021\text{-}0.11$ . When the tweed domains are treated as the 2H-phase, the best agreement is obtained for the particle size of  $950\Omega$ . It is very important to emphasize that a variation of the periodicity of the martensitic interface structure can help make the predictions of the models for the modulus and the strain interactions agree much better with the measured obstacle profile, than shown in Figure 54. A recent TEM study of the  $\beta_1\text{-}\gamma_1$  interface (137) shows indeed that the period of the interface structure is often less than the 50 nm assumed throughout this work.

The lattice friction stress change interaction and the interfacial energy change interaction depend on  $\Delta\tau(V_p)^{1/3}$  and  $\Delta\gamma(V_p)^{1/3}$ , respectively. When compared with the measured obstacle profile, these two interactions, individually or combined, predict a relatively shorter range of interaction, Figure 54. The best agreement with the measured behavior in the range of low activation volumes is obtained by taking:  $\Delta\gamma(V_p)^{1/3} = 10^{-6} \text{ mJ/m}$ . For a domain size in the range of  $480\text{-}2700 \Omega$  this yields  $\Delta\tau = 4.5 \cdot 10^3 \mu_0$  and  $\Delta\gamma = 500\text{-}880 \text{ mJ/m}^2$ . The magnitudes of both  $\Delta\tau$  and  $\Delta\gamma$  are at least one order of magnitude higher than their reasonable estimates. For constant values of  $\Delta\tau(V_p)^{1/3}$ , and  $\Delta\gamma(V_p)^{1/3}$ ,  $\Delta\tau$  and  $\Delta\gamma$

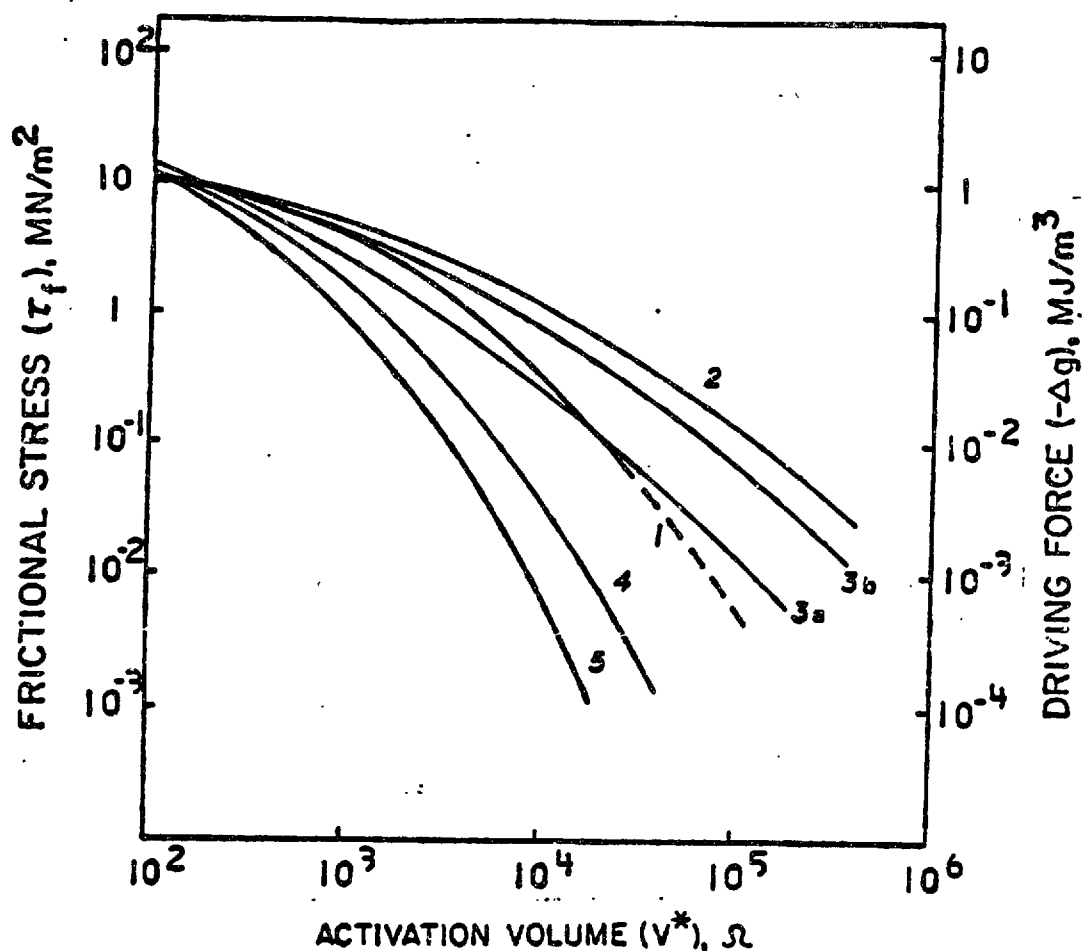


Figure 54 Comparison of the measured obstacle profile, curve 1 with different obstacle profiles derived from the models for the interaction of the  $\beta_1$ - $\gamma_1$  interface with strain (tweed) domains: curve 2 - modulus interaction; curve 3a - strain interaction, tweed domains with a tetragonal distortion; curve 3b - tweed domains of the 2H-phase; curve 4 - lattice friction stress change interaction; curve 5 - interface energy change interaction.

as estimated above, can be reduced by one order of magnitude by increasing the particle volume by three orders of magnitude. This however would not be consistent with the observed size of the tweed structure. The lattice friction stress interaction and the interfacial energy change interaction, thus, can have only a minor contribution to the measured thermal component of the friction stress (driving force). Conversely, the modulus and the strain interaction between the moving interface and the tweed domains become very likely rate controlling mechanisms of the interface motion. It is particularly interesting to note a very close similarity between the measured obstacle profile, curve 1, Figure 54, and the model predicted profile for a single strain interaction between the tetragonally distorted tweed domains and the interface, curve 3a. Figure 54, for the assumed periodicity of the martensitic interface structure.

#### 7.1.4 Other prospective mechanisms of interaction

The measured mobilities of the  $\beta_1-\gamma_1'$  martensitic interface, as discussed in previous sections can be explained successfully, by the athermal interaction of the interface with discrete 2H-phase particles and the thermally activated interactions with strain domains. In this section other possible interactions are considered.

Besides the modulus and strain interactions another type of long-range interaction may exist between the  $\beta_1-\gamma_1'$  interface and internally-twinned 2H-particles (140). The transformation twins in  $\gamma_1'$ -martensitic and thus in the 2H-phase, are found to thicken or become thinner when a stress is applied (133, 141-143). This observation is the basis of several different theories of the shape memory effect (133, 141). It



is conceivable that 2H-twins behave similarly when a 2H-particle finds itself in the stress field of a moving interface. Changes in the thickness of twins are accomplished by motion of twinning dislocations, which can be spaced either well-apart or close together. In either case, motion of the twinning dislocations will be associated with some friction stress, which will appear for both forward and reverse motion of the martensitic interface, and affect the transformation hysteresis. Quantitative analysis of this type of interaction, which involves two moving defects is complicated. It is expected that this interaction should bear some similarity with the solute-drag mechanism of dislocation motion. Namely, motion of both the interface and the twinning dislocations are time- and temperature-dependent processes. There must be, therefore, a temperature region and corresponding interface velocity region, in which the interaction of the two moving defects is maximized.

It is well established (133, 134, 139, 144, 145) that twin widths in martensite gradually increase with distance from the interface. Again, this change is accomplished by motion of twinning dislocations. These dislocations are now expected to be spaced well apart since the change in twin width is very gradual. The twinning dislocations are dragged along, as the martensitic interface advances, and interact with the same obstacles as the interface. However, since well-separated, these dislocations will behave more like line dislocations. The critical event of thermally-activated motion is then more two-dimensional in character, giving rise to smaller values of activation volume. This type of interaction, thus, can account for the relatively

small values of the activation volume which were found experimentally. It is, however, difficult to separate the contribution of this interaction from the contribution made by the interaction of the interface with strain domains to the short-range part of the measured obstacle profile.

Interaction of the interface with lattice dislocations is excluded from being the rate controlling mechanism of the interface motion, because the density of dislocations is small, and  $\beta_1-\gamma_1'$  martensitic transformation is almost ideally thermoelastic.

The  $\beta_1-\gamma_1'$  martensitic transformation involves some shuffling, which produces the correct sequence of the close packed planes in the martensitic phase. The shuffling does not produce any shape change, and is often considered to be accomplished by an array of dislocation dipoles. These shuffling dislocations then represent yet another component of the interface dislocation structure. When superposed upon the (lattice-deformation) coherency dislocations, these may affect the microtopography of the interface and become the most significant coherency dislocation array, Section 6.1.

In a system in which the parent phase (and thus the martensitic phase) is ordered and the lattice-invariant deformation is a twinning shear, another type of shuffling is often required to produce a correct structure of the twinned martensitic. Namely, the lattice invariant twinning, in general, preserves the lattice, but not necessarily the structure of the ordered martensite. This kind of shuffling was analyzed by Lieberman (146), who demonstrated its relationship to the shape memory phenomena in AuCd alloys. It is interesting that in Cu-Al-Ni alloys, both types of shuffling are identical, and very small

(145). As a time dependent process, completion of shuffling may be delayed until after the moving interface has passed, giving rise to a structurally incomplete martensite. When referred to the transformation hysteresis, this structural change increases  $\tau_0$ . If enough time elapses before the reverse motion of the interface, shuffling will be completed, producing the correct structure of twinned martensite. By the same token, an incomplete structure of the parent phase is produced during the reverse run of the interface, what now decreases  $\tau_0$ . In other words, this type of interaction between the interface and transformation shuffling increases the transformation hysteresis, and thus produces a component of the friction stress. The increment of the friction stress caused by the delayed shuffling is governed by the free energy difference between the imperfect (unshuffled) and perfect (shuffled) structure of martensite. Since the required shuffling in the case at hand is very small, it is hardly likely that the shuffling plays any important role in the kinetics of interface motion, especially in the low interface velocity range investigated in this work.

## 7.2 Anomalous Behavior at Temperatures below $\sim 210\text{K}$

As discussed in Section 5.1, an anomalous positive temperature dependence of the friction stress is found at temperatures below 210K. This behavior is inconsistent with the concept of thermally-activated motion of the  $\beta_1-\gamma_1'$  interface, which, as shown in Section 7.1, accounts quite well for the measured mobilities of the interface in the range of temperature between 210K and 410K. It should be noted that the temperature range of anomalous behavior is associated with a slightly higher positive temperature dependence of the shear elastic constant  $C'$ , Figure

9. This elastic constant represents a resistance to  $\{110\}_{\beta_1} \langle \bar{1}\bar{1}0 \rangle_{\beta_1}$  shear, which is usually considered to be the first Bogers-Bugers shear (147), for  $\beta_1-\gamma_1'$  martensitic transformation. It seems then natural to expect that the  $C'$  is more related to the friction stress than the isotropic shear modulus, particularly when the material is highly anisotropic, as in this case. If the friction stress and  $C'$  are indeed directly related then  $\tau_f/C'$  should show the same negative temperature dependence in the entire temperature range explored here. However, this is not the case.  $\tau_f/C'$  does show a weaker but still positive temperature dependence in the temperature range below 210K. Other elastic constants, associated with different potentially important shear modes, show either weaker positive or normal negative temperature dependence, and cannot account for the anomalous behavior either. Even though this analysis failed, it is believed that the common temperature range of the anomalous behavior of  $\tau_f$  and of the larger positive dependence of  $C'$  is not incidental. However, lower values of  $C'$  do not only soften the resistance of the lattice to the corresponding shear strain, but also might affect the structure of the interface, and possibly interact with the second-phase precipitates. There are a number of theoretical works (148-150) which predict that the interface becomes more diffuse, with the softening of the lattice, i.e. elastic constants. Interaction of a diffuse interface with discrete obstacles is expected to be less intense than the interaction of a sharp interface, which was treated throughout this thesis. This is analogous to the reported softening of the obstacle profiles associated with an increase in particle size, Section 6.4. Since the  $\{110\}_{\beta_1} \langle \bar{1}\bar{1}0 \rangle_{\beta_1}$  shear mode is one of

the shears involved in  $\beta_1 \rightarrow 2H$  change it is conceivable that the softening of C' in the temperature range below 210K, may interact with the 2H-phase, making it grow. This affects the friction stress and may be associated with the anomalous behavior.

To summarize, it seems likely that softening of C' is related to the anomalous temperature dependence of the friction stress. Although some possible interactions of lattice softening and interface mobility can account for the anomaly, the exact origin of this behavior is still unknown.

### 7.3 Kinetics of Martensitic Interface Motion

In Section 7.1 it was shown that the measured mobilities of a single  $\beta_1-\gamma_1'$  martensitic interface could be accounted for by rate controlling interactions with discrete second phase particles and strain domains. In their interactions with prospective obstacles to their motion, coherency dislocations, modelled as a surface dislocation, were shown to behave in many respects similarly to line dislocations, but there are some significant differences caused by differences in geometry. Since the entire analysis to this point has been concerned exclusively with the single-interface thermoelastic  $\beta_1-\gamma_1'$  martensitic interface, it is important to discuss how, and to what extent, the findings from this work are applicable to the general problems of martensitic interface motion and martensitic growth. This is done by recognizing the important differences and similarities in the growth characteristics of single-interface thermoelastic and the more common non-thermoelastic transformations.

Since the lattice-invariant deformation in the  $\beta_1-\gamma_1'$  transformation is accomplished by twinning, the interface structure can be described in terms of coherency dislocations. In the more general case, when the lattice-invariant deformation proceeds by slip, some anticoherency lattice dislocation arrays reside in the interface. In either case, growth of martensite involves both the motion of existing interface dislocations and the formation of new ones. In the case of single-interface transformations, dislocation nucleation is often assumed to occur at free surfaces, which rules out this process from being a rate controlling step in martensitic growth. In the more general case of the growth of martensitic plates, calculations of the activation energies (33) suggested that both the dislocation motion and the anticoherency dislocation nucleation are possible rate-controlling mechanisms of the interface motion. While the anticoherency dislocations possess the larger Burgers vectors, their interaction with coherency dislocations produces no long-range strain field and their formation together is thus self-compensating. Activation-energy estimates (33) suggest that thermally assisted formation of anticoherency dislocations is viable under the conditions for which martensitic transformations are known to occur, and may be the rate-controlling step as proposed in earlier treatments of the transformation kinetics (152, 153). Experimental and theoretical investigation done in this work, on the other hand, suggest that the thermally-assisted motion of coherency dislocations is also a possible rate controlling step in the martensitic growth process. Which of the two processes, coherency dislocation motion or anticoherency dislocation nucleation, is the rate controlling step may vary

from one system to another. However, it is important to invoke the findings of Olson and Cohen (154) that the basic nucleation-kinetics behavior of the fcc  $\rightarrow$  hcp martensitic transformation is essentially the same as that of the fcc  $\rightarrow$  bcc transformation in the same alloy system. Since the lattice invariant deformation is absent in the fcc  $\rightarrow$  hcp case, they concluded that the coherency-dislocation motion is the most likely rate controlling step of the nucleation kinetics. Since the nucleation process is believed to be the growth start-up from the existing martensitic embryos, their conclusion might be applicable to the growth process of grown martensitic plates. This also means that the basic findings in this work can be applied to the general problem of martensitic interface motion.

Since the  $\beta_1-\gamma_1'$  martensitic transformation is thermoelastic, the driving force attending the nucleation of martensite is relatively low (155), so that the martensitic interface is always close to equilibrium. Non-thermoelastic martensitic transformations, on the other hand, are characterized by a large driving force for nucleation, which then drives interfacial dislocations during the growth process. Growth of a martensite plate, modelled as an oblate spheroid, is often conceptually separated into edgewise or radial growth and sidewise growth or thickening. Raghavan and Cohen (156) have used the free energy gradients in the radial and thickness directions to evaluate the net transformational forces for driving the interfacial dislocations. They showed that these transformational forces are very large, so that eventually martensitic interfaces in both radial and thickness directions attain very high velocities, which correspond to the phonon drag-controlled regime, where

the thermal activation does not play any significant role. After the radial growth is stopped by an obstacle, thickening continues with a decreasing rate, and a continuous transition from the drag-controlled regime into the thermally-assisted regime of interface motion is expected. It is thus this final stage of the plate thickening for which it is expected that the findings of this work are especially applicable.

Interaction of the  $\beta_1-\gamma_1'$  martensitic interface with lattice dislocations was ruled out from being the rate controlling mechanism of the interface motion for two reasons: (i) the density of lattice dislocations was found to be relatively low, and (ii) the plastic deformation in the accommodation of the transformation shape change seemed to be insignificant. In the general case neither of the two conditions stated above should exist, and the interactions of martensitic interfaces with lattice dislocations must be considered. When spaced well-apart, interface dislocations are expected to react individually with lattice dislocation producing dislocation jogs or some sessile dislocation configurations. Interaction of closely spaced interface dislocations, i.e. a surface dislocation, with lattice dislocations produces interface steps. For low-index rational interfaces these steps may play an important role in the martensite growth through the operation of some pole mechanisms (33). High index rational and irrational interfaces are already stepped, so that the introduction of new steps through the intersection of the interface with lattice dislocation introduces only some local perturbation in the periodic stepped structure of the interface. Since the pole mechanism is usually considered unnecessary for the motion of the high-index rational and



irrational interfaces, it remains unclear how the interaction of the interface with intersecting lattice dislocations affects its thermally activated motion.

Tangled lattice dislocations, usually observed in the parent phase adjacent to the martensitic plates, produce localized regions of high distortion, and thus can be approximately treated in a similar way to discrete second phase particles and strain domains. The long-range strain interaction between the interface and the dislocation tangles can become the rate controlling mechanism for interface motion, and is expected, at least in a range of low driving force, to follow the behavior found in this work. It should be pointed out that generation of the dislocation tangles, i.e. plastic zones around the moving martensite plates, does not only introduce a new prospective rate controlling obstacle to interface motion but also alters the effective driving force acting on the moving interfaces (47). With these modifications included, the results of this work can be applied to the martensitic transformations with a substantial amount of plastic accommodation deformation.

In the range of low interface velocity investigated in this work, it was confirmed that the motion of the interface proceeds almost isothermally. The chemical driving force attending the martensitic transformation was consequently defined as the corresponding free energy difference. At the highest employed interface velocity, which was excluded from the analysis, the thermal effect of the transformation appeared to disturb the isothermal conditions significantly. In most general instances martensitic growth is neither isothermal nor adiabatic, so that a more general thermodynamic driving force is required than the

free energy (isothermal growth) or the enthalpy (adiabatic growth) change. This is another modification to be introduced, when models developed in this work are applied to the more general case of martensitic interface motion in nonisothermal conditions.

The entire analysis in this work has been done under the assumption of relative temperature insensitivity of the important activation parameters. This was justified by the experimental verifications of a weak temperature dependence of the elastic constants. In cases when the elastic constants show significant variation with temperature, the modified activation analysis, outlined in Section 2.2.3, should be employed before use is made of the models developed in this work.

## 8. CONCLUDING REMARKS

Over a temperature range of 210 to 410K and a velocity range of  $10^{-6}$  to  $10^{-2}$  m/s, the mobility of the  $\beta_1-\gamma_1'$  interface is consistent with thermally-activated motion. This behavior is rationalized in terms of rate control by the interaction of the interface, modelled as a dislocation array, with the observed fine-scale particle dispersion, i.e. the tweed structure. The strain and modulus type of interactions appear to be the most probable controlling interactions. The overall shape of the measured obstacle profile and of the corresponding activation energy driving force relation, along with the magnitudes of the activation volume, support this conclusion. Other potential rate controlling mechanisms are determined to have a minor, if any, contribution to the measured behavior. The interaction of the interface with lattice dislocations was neglected due to their low observed density consistent with the thermoelastic character of the martensitic transformation. In the more general case when the dislocation density is significantly higher (as when accommodation of the transformation shape change occurs by slip) the interface-dislocation interaction may become important. As long as the interface is considered as a continuous surface dislocation, however, it does not seem that this interaction could give rise to a thermally surmountable obstacle to the interface motion. The Peierls energy barrier for the interface motion has a very low activation energy and is thus easily surmountable by thermal activation. For metals, the Peierls barrier is thus less likely to be a rate

controlling mechanism of the interface motion (at temperatures near ambient).

The athermal component of the measured friction stress (driving force) is attributed to the long range interaction of the  $\beta_1-\gamma_1'$  martensitic interface with the observed coarser scale particles of the 2H-phase. The strain interaction and modulus interaction most likely provide a major contribution to this athermal component. In the more general case of non-thermoelastic martensitic transformations where the transformation shape change is accommodated by slip, interaction of the moving interface with lattice dislocations may become important. Though the detailed mechanism of the interface-dislocation interaction is not clear, and probably depends on the dislocation morphology and density, a similar behavior as for the interface-particle interaction might be expected.

The entire concept of thermally activated motion of martensitic interfaces rests on the assumption that the effective force which drives the interfaces (i.e. the friction stress or the driving force, as used throughout this work) is significantly smaller than the corresponding threshold force, and that the associated activation energy has some reasonably low value. When the effective driving force on an interface exceeds the corresponding threshold value, as may be the case for martensitic transformations in the rapid stage of the growth of a martensite plate, thermal activation has little significance. The final stage of growth of martensitic plates, however, proceeds under lower net driving force, and is expected to be controlled by thermal activation. Some modifications of the models derived for the single-interface thermoelastic transformations would be required for application to such a case. These modifications would take into account, for

example, the deviation from isothermal conditions often met in non-thermoelastic martensitic transformations, as well as the dynamic interaction of the interface with simultaneous accommodation slip. The experience gained here in examining the intrinsic mobility of a simple single interface in a thermoelastic alloy under well-defined conditions should provide the groundwork for the development of models for these more complex phenomena.

## 9. SUGGESTIONS FOR FUTURE WORK

1. Details of the short range (low  $V^*$ ) behavior of the  $\beta_1-\gamma_1'$  single-interface motion could not be discerned in this work due to the intervention of the anomalous lattice softening effect at temperatures below 210K; i.e., in the temperature range  $M_s$  to  $\sim M_s + 60K$ . Further low temperature mobility information can be obtained using Cu-Al-Ni alloys with significantly lower  $M_s$  temperature.
2. The critical stress for the martensite nucleation increases with testing temperature, while the yield stress shows a negative temperature dependence. Cu-Al-Ni alloys with low  $M_s$  are thus expected to deform by slip at high temperature, rather than undergoing a martensitic transformation. Some preliminary work on alloy B1 suggested an onset of the slip at temperatures above  $\sim 350^\circ C$ . It is expected that alloys with lower  $M_s$  may start yielding by slip at lower temperatures. Thus, this provides an ideal opportunity for comparing kinetics of the slip dislocations motion and of the martensitic interface motion in the same alloy.
3. Lattice softening in a temperature region just above the  $M_s$  temperature is often considered to affect the interface width. This can be conveniently investigated by the high-resolution electron microscopy, using Cu-Al-Ni alloys with  $M_s$  close to room temperature.

4. Further development of the models for the martensitic interface motion proposed in this work should include the effect of the high anisotropy found in this work, diffusiveness of the interface, etc.

APPENDIX A: HEAT TRANSFER ANALYSIS FOR A SINGLE-INTERFACE MARTENSITIC TRANSFORMATION

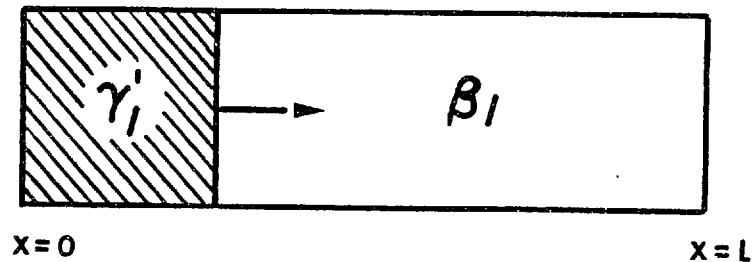


Figure A.1 A simple model for a single interface  $\beta_1-\gamma_1'$  transformation.

For a simple model shown in Figure A.1 a heat conduction equation can be written as:

$$\frac{\partial T}{\partial t} = a^2 \frac{\partial^2 T}{\partial x^2} + b\delta(x-vt) \quad (A1)$$

where: T- temperature,

t- time,

$a^2$ - thermal diffusivity,

$\delta(x-vt)$ - Dirac's  $\delta$ -function,

v- interface velocity,

$b=\Delta Hv/c$ ,

$\Delta H$ - enthalpy change accompanying the  $\beta_1-\gamma_1'$  transformation,

c- specific heat.

For a stress-induced transformation in a compression test in which a parallel-sided specimen is in contact with metal platens the following initial and boundary conditions might be considered appropriate:

I.C.  $T(x,0) = 0$



$$\text{B.C. } T(0,t) = T(L,t) = 0$$

Using the method of Laplace transformation (157,158) the following solution was obtained:

$$\begin{aligned}
 T(x,t) = & b/v \{ - \operatorname{erfc}(x/2a\sqrt{t}) + 0.5( \exp[-v(x-vt)/a^2] \operatorname{erfc}(x/2a\sqrt{t}- \\
 & v\sqrt{t}/a) + \exp[v(x+vt)/a^2] \operatorname{erfc}(x/2a\sqrt{t} + v\sqrt{t}/a) + [ 1 + \\
 & \exp[ - v(x-vt)/a^2 ] u(t-x/v) ) \} + b/v \sum_{m=1}^{\infty} \sum_{n=1}^{\infty} (-1)^m \\
 & \{ \operatorname{erfc}[(2nL+(-1)^m x)/2a\sqrt{t}] + 0.5[ \exp[ v^2 t - v(2nL+(-1)^m x)/a^2 ] \\
 & \operatorname{erfc}[(2nL+(-1)^m x)/2a\sqrt{t} - v\sqrt{t}/a] + \exp[v^2 t + v(2nL+(-1)^m x)/a^2 ] \\
 & \operatorname{erfc}[(2nL+(-1)^m x)/2a\sqrt{t} + v\sqrt{t}/a] \} \quad (\text{A2})
 \end{aligned}$$

where  $u(t-x/v)$  refers to a step function.

The following values were attributed to the parameters appearing in equations (A1) and (A2):

<u>Parameter</u>	<u>Reference</u>
$a^2 = 16.3 \text{ mm}^2/\text{s}$	(65)
$c = 23,8 \text{ J/mole K}$	(64)
$\rho = 7.1 \text{ gr/cm}^3$	this work
$\Delta H = 515 \text{ J/mole}$	(159)
$L = 20 \text{ mm}$	this work

Figure A.2 shows the predicted thermal effect for the single-interface  $\beta_1-\gamma_1'$  transformation. When compared with figure 8 it shows a fairly good agreement. This model allows an estimation of temperature profile along the specimen for any arbitrary position of the moving interface, what is shown in Figure A3. In this way one can estimate the temperature in regions adjacent to the moving interface. Furthermore, using the model a variation in the temperature of the interface, as it is displaced, can be obtained, as depicted in Figure A4.

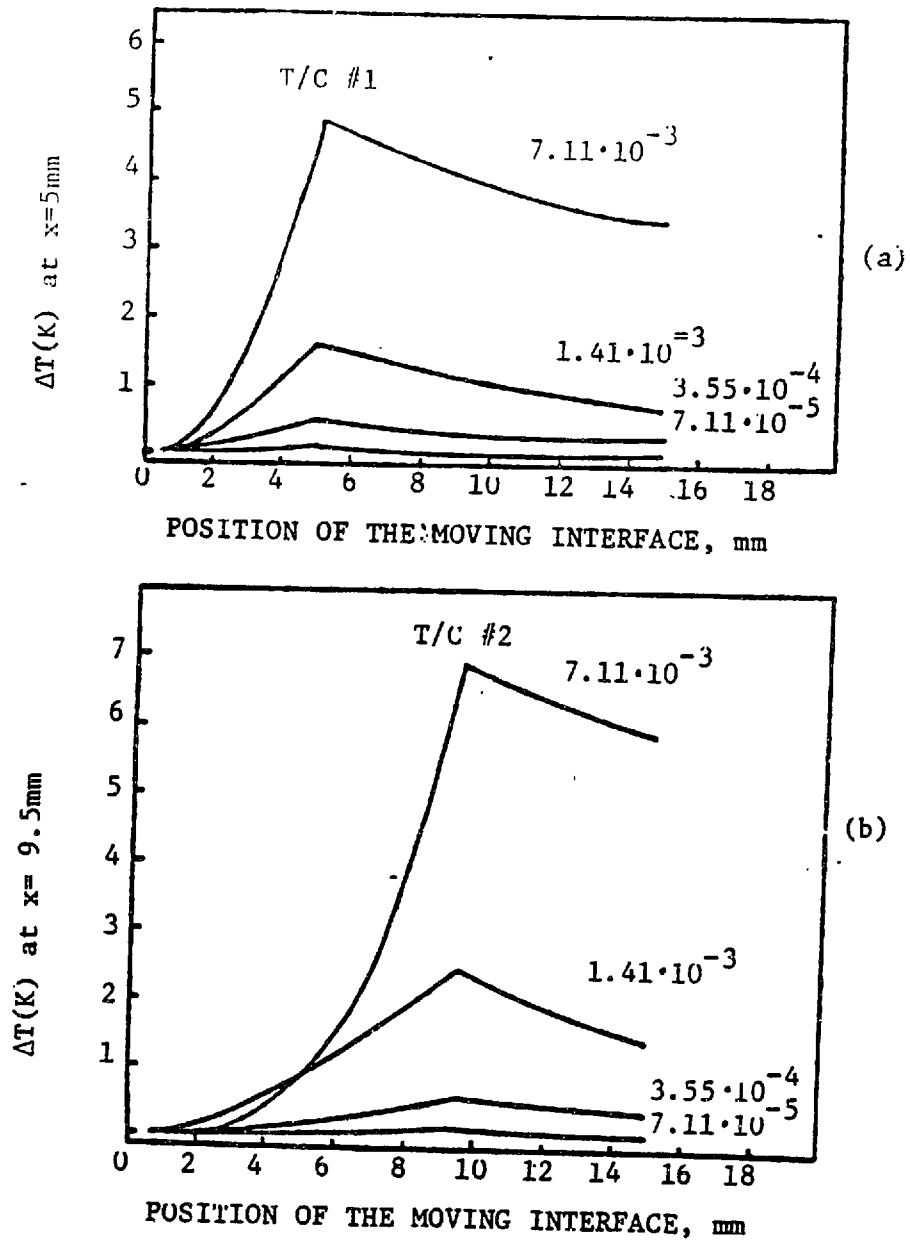


Figure A2 The model-derived thermal effect due to single interface stress-induced  $\beta_1-\gamma_1'$  martensitic transformation expressed as a temperature increment,  $\Delta T$  (K), at two positions: (a)  $x=5\text{mm}$  and (b)  $x=9.5\text{mm}$  which varies with a position of the moving interface. The numbers on the plots give the interface velocity in m/s.

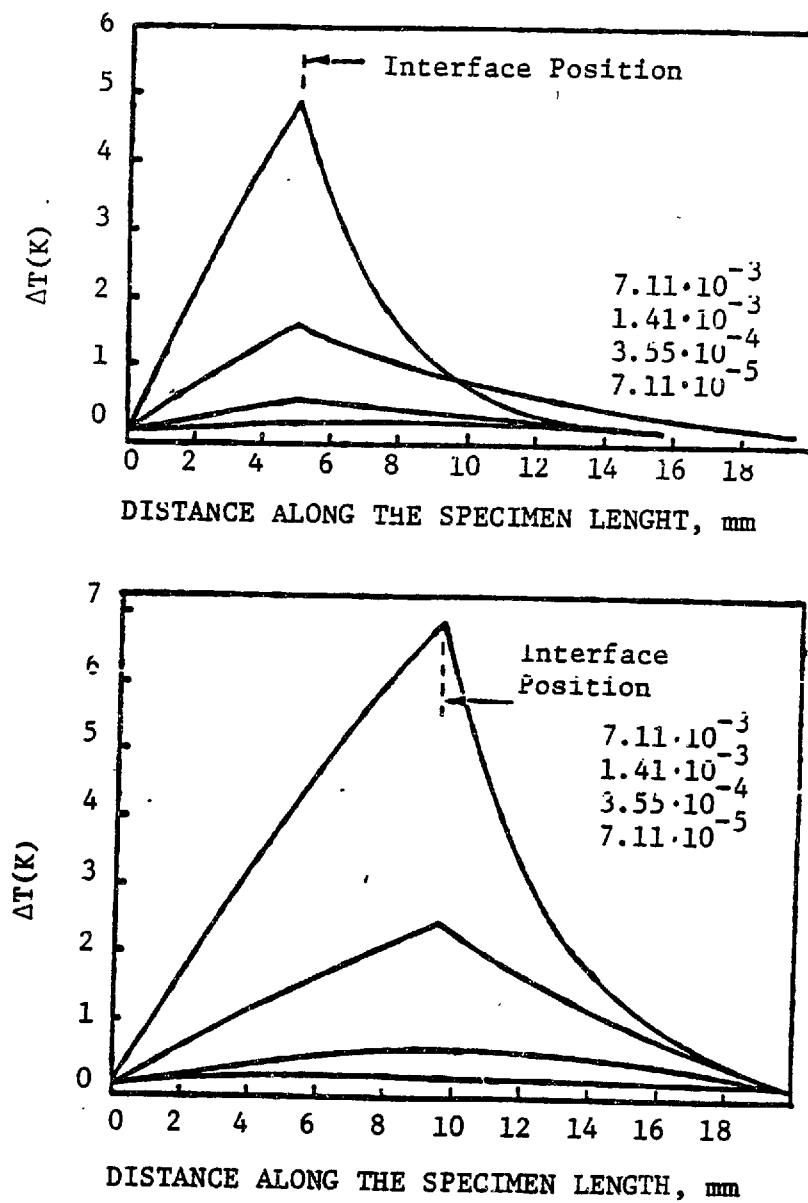


Figure A3 The temperature profiles  $\Delta T(K)$ , along the specimen length corresponding to two different positions of the moving interface: (a)  $x=5$  mm; (b)  $x=9.5$  mm. The numbers on the plot give the interface velocity in m/s.

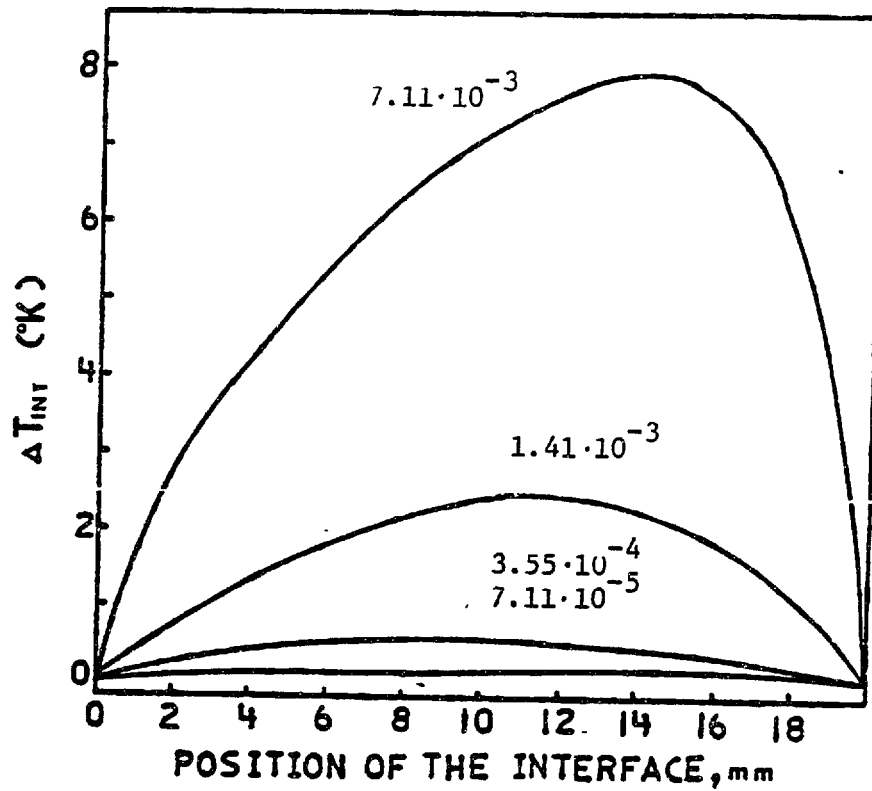


Figure A4 Variation of the interface temperature accompanying its motion. Numbers in the plot correspond to the interface velocity in m/s.

APPENDIX B: MODULUS INTERACTION BETWEEN THE  $\beta_1-\gamma_1'$  MARTENSITIC INTERFACE AND A SECOND-PHASE PARTICLE

The change in the elastic strain energy caused by the presence of a modulus-misfit particle of radius ,r ,in the stress field of the  $\beta_1-\gamma_1'$  interface is :

$$\Delta E = \frac{4}{3} \pi r^3 \frac{\epsilon_\mu}{2\mu} ( \sigma_{xz}^2 + \sigma_{yz}^2 ) \quad (B1)$$

Accordingly, the interaction force is:

$$F_M = - \frac{d\Delta E}{dx} = \frac{4}{3} \pi r^3 \left[ \sigma_{xz} \frac{\partial \sigma_{xz}}{\partial x} + \sigma_{yz} \frac{\partial \sigma_{yz}}{\partial x} + \frac{dy}{dx} \left( \sigma_{xz} \frac{\partial \sigma_{xz}}{\partial y} + \sigma_{yz} \frac{\partial \sigma_{yz}}{\partial y} \right) \right] \quad (B2)$$

The stress functions  $\sigma_{xz}$  and  $\sigma_{yz}$  were given in Section 6.3.

The following two computer programs (in BASIC ) compute the modulus interaction force, expressed as  $F_M D / \mu_o \epsilon_\mu r^3$  . Program #1 deals with small particles; whereas Program #2 takes into account the variation of the interaction force within a particle of finite size.

PROGRAM #1: INTERFACE -PARTICLE MODULUS INTERACTION / SMALL PARTICLE APPROXIMATION

```

100 INIT
110 PRINT "MODULUS MISFIT"
120 PRINT "N,Z,W,D,I,F,S"
130 INPUT N,Z,W,D,I,F,S
140 PAGE
150 PRINT "MODULUS MISFIT"
160 PRINT "SMALL PARTICLE APPROXIMATION"
170 PRINT "PARTICLE PATH IS Y= 1.17*X-";-Z
180 PRINT "X", "X/W", "FORCE", "LOG(FORCE)"
190 PRINT
200 FOR X=1 TO F STEP S
210 A1=0
220 A2=0
230 A3=0
240 A4=0
250 B1=0
260 B2=0
270 B3=0
280 B4=0
290 Y=1.17*X+Z
300 IF 2*3.141*X/D>40 THEN 360
310 GO TO 390
320 LET N=N/2
330 LET D=D*X2
340 GO TO 340
350 LET X1=2*3.141*X/W
360 LET S1=(EXP(X1)-EXP(-X1))/2
370 LET C1=(EXP(X1)+EXP(-X1))/2
380 LET X2=2*3.141*X/D
390 LET S2=(EXP(X2)-EXP(-X2))/2
400
410
420
430

```

```

440 C2=(EXP(X2)+EXP(-X2))/2
450 N=INT(N)
460 FOR M=-N TO N STEP 1
470 LET Y1=2*3.141*(Y+M*D)/W
480 LET A1=SIN(Y1)/(C1+COS(Y1))
490 LET A2=SIN(Y1)*S1/(C1+COS(Y1))^2
500 LET A3=S1/(C1+COS(Y1))
510 LET A4=(C1*COS(Y1)+1)/(C1+COS(Y1))^2
520 NEXT M
530 LET Y2=2*3.141*Y/D
540 LET B1=81+80/276*W/D*SIN(Y2)/(C2-COS(Y2))
550 LET B2=80/276*W^2/D^2*S2*SIN(Y2)/(C2-COS(Y2))^2
560 LET B3=80/276*W/D*S2/(C2-COS(Y2))
570 LET B4=80/276*W^2/D^2*(C2*COS(Y2)-1)/(C2-COS(Y2))^2
580 LET D1=-0.005544/N^2*((A1+B1))*(A2-B2)+(A3-B3)*(A4+B4)
590 LET D2=-0.005544/N^2*((A1+B1))*(A4+B4)*1.17)
600 LET D3=-0.005544/N^2*((A3-B3))*(A2+B2)*1.17)
610 LET D4=D1+D2+D3
630 IF D4<=0 THEN 660
640 PRINT X,X/W,D4,LGT(D4)
650 GO TO 670
660 PRINT X,X/W,D4
670 NEXT X
680 END

```

PROGRAM #2: INTERFACE-PARTICLE MODULUS INTERACTION / FINITE PARTICLE SOLUTION

```

100 INIT
110 PRINT "MODULUS MISFIT"
120 PRINT "N9,Z,W,D9,I,F,S,S9"
130 INPUT N9,Z,W,D9,I,F,S,S9
140 PAGE
150 PRINT "MODULUS MISFIT"
160 PRINT S*S9;"A PARTICLE SIZE"
170 PRINT "PARTICLE PATH IS Y= 1.17*X-";-Z
180 PRINT "X", "X/M", "FORCE", "LOG(FORCE)"
190 PRINT
200 R=0
210 FOR X9=1 TO F STEP S
220 D5=0
230 LET D4=0
240 LET Y9=1.17*X9+Z
250 LET P=-2 TO 2
260 FOR X=X9+P*S9
270 N=N9
280 D=D9
290 FOR Q=-2 TO 2
300 LET Y=Y9+Q*S9
310 A1=0
320 A2=0
330 A3=0
340 A4=0
350 B1=0
360 B2=0
370 B3=0
380 B4=0
390 B5=0
400 B6=0
410 B7=0
420 B8=0
430 IF 2*3.141#ABS(X/D)>40 THEN 450

```



```

440 GO TO 480
450 LET H=N/2
460 LET D=D*2
470 GO TO 430
480 LET X1=2*X3.141*X/W
490 LET S1=(EXP(X1)-EXP(-X1))/2
500 LET C1=(EXP(X1)+EXP(-X1))/2
510 LET X2=2*X3.141*X/D
520 LET S2=(EXP(X2)-EXP(-X2))/2
530 LET C2=(EXP(X2)+EXP(-X2))/2
540 FOR M=-INT(H) TO INT(H) STEP 1
550 LET Y1=2*X3.141*(Y+M*D)/W
560 LET A1=SINC(Y1)/(C1+COS(Y1))
570 LET A2=A2+SINC(Y1)*S1/(C1+COS(Y1))*T2
580 LET A3=A3+S1/(C1+COS(Y1))
590 LET A4=A4+(C1*COS(Y1)+1)/(C1+COS(Y1))*T2
600 NEXT M
610 LET Y2=2*X3.141*X/D
620 LET B1=B1+80/276*X/W/D*SINH(Y2)/(C2-COS(Y2))
630 LET B2=B2+80/276*W/T2/D*T2*S2*SINC(Y2)/(C2-COS(Y2))*T2
640 LET B3=B3+80/275*X/W/D*S2/(C2-COS(Y2))
650 LET B4=B4+80/276*W/T2/D*T2*(C2*COS(Y2)-1)/(C2-COS(Y2))*T2
660 LET D1=-0.005544/N*T2*(A1+B1)*(-A2-B2)+(A3-B3)*(A4+B4)
670 LET D2=-0.005544/N*T2*(A1+B1)*(A4+B4)*I.17
680 LET D3=-0.005544/N*T2*(A3-B3)*(A2+B2)*I.17
690 LET D5=D5+D1+D2+D3
700 R=R+1
710 NEXT P
720 NEXT P
730 LET D4=D5/25
740 IF D4<=0 THEN 770
750 PRINT X9,X9/W,D4,LGT(D4)
760 GO TO 780
770 PRINT X9,X9/W,D4
780 NEXT X9

```

APPENDIX C: STRAIN INTERACTION BETWEEN THE  $\beta_1-\gamma_1'$  MARTENSITIC INTERFACE AND A SECOND PHASE PARTICLE

The  $\epsilon_{ij}^T$  of the particle is considered to be an invariant plane strain (IPS). There are then two nonzero components of  $\epsilon_{ij}^T$ :  $\epsilon_{13}^T = \epsilon_{31}^T$  and  $\epsilon_{33}^T$ . The primed basis is defined by the projection of the displacement direction onto the invariant plane,  $\vec{d}_p$ ,  $\vec{d}_p \times \vec{n}$ , and by the invariant plane normal,  $\vec{n}$ .

With respect to the unprimed basis defined by the martensitic interface, then :

$$\epsilon_{13}^T = (a_{11}a_{33} + a_{13}a_{31})\epsilon_{13}^{T'} + a_{13}a_{33}\epsilon_{33}^{T'} \quad (C1)$$

$$\epsilon_{23}^T = (a_{21}a_{33} + a_{23}a_{31})\epsilon_{13}^{T'} + a_{23}a_{33}\epsilon_{33}^{T'} \quad (C2)$$

where  $a_{ij}$ 's are directional cosines defining a rotation between the two coordinate systems.

The strain interaction force between the interface and a particle of radius  $r$  is then:

$$F_s = - \frac{dE_s}{dx_1} = \frac{4}{3} \pi r^3 \left[ \epsilon_{13}^T \left( \frac{\partial \sigma_{13}}{\partial x_1} + \frac{dx_2}{dx_1} \right) + \epsilon_{23}^T \left( \frac{\partial \sigma_{23}}{\partial x_1} + \frac{dx_2}{dx_1} \frac{\partial \sigma_{23}}{\partial x_2} \right) \right] \quad (C3)$$

The following two computer programs compute the strain interaction force between the  $\beta_1-\gamma_1'$  interface and a particle, the  $\epsilon_{ij}^T$  of which is an IPS. Program #3 treats the case of a small particle, whereas Program #4 takes into account the variation of the interaction force throughout the particle.

Program #5 treats the case of small particles with  $\epsilon_{ij}^T$  being a general orthorhombic distortion rather than an IPS.

```

PROGRAM #3; INTERFACE-PARTICLE STRAIN INTERACTION / SMALL PARTICLE SOLUTION/ $\epsilon_{ij}^T$  --.IPS
100 INIT
110 PRINT "STRUCTURE MISFIT"
120 PRINT "N9,Z,W,D9,I,F,S"
130 INPUT N9,Z,W,D9,I,F,S
140 PRINT "E1 THROUGH E9"
150 INPUT E1,E2,E3,E4,E5,E6,E7,E8,E9
160 PAGE
170 PRINT "STRUCTURE MISFIT"
180 PRINT "TWINNED PARTICLES"
190 PRINT "SMALL PARTICLE APPROXIMATION"
200 PRINT "PARTICLE PATH IS  $\gamma = 1.17 * X -$ "; -Z
210 PRINT "X", "X/W", "FORCE", "LOG(FORCE)"
220 PRINT FOR X=I TO F STEP S
230 N=N9
240 D=D9
250 A1=0
260 A2=0
270 A3=0
280 A4=0
290 B1=0
300 B2=0
310 B3=0
320 B4=0
330 LET Y=1.17*X+Z
340 IF 2*X3.141*ABS(X/D)>40 THEN 420
350 GO TO 450
360 LET N=N/2
370 LET D=D*2

```

```

440 GO TO 400
450 LET X1=2*3.141*X/W
460 LET S1=(EXP(X1)-EXP(-X1))/2
470 LET C1=(EXP(X1)+EXP(-X1))/2
480 LET X2=2*3.141*X/D
490 LET S2=(EXP(X2)-EXP(-X2))/2
500 LET C2=(EXP(X2)+EXP(-X2))/2
510 FOR M=-INT(N) TO INT(N) STEP 1
520 LET Y1=2*3.141*(Y+M*D)/W
530 LET A1=A1+SIN(Y1)/(C1+COS(Y1))
540 LET A2=A2+SIN(Y1)*S1/(C1+COS(Y1))^2
550 LET A3=A3+S1/(C1+COS(Y1))
560 LET A4=A4+(C1*COS(Y1)+1)/(C1+COS(Y1))^2
570 NEXT M
580 LET Y2=2*3.141*Y/D
590 LET B1=B1+80/276*W/D*SIN(Y2)/(C2-COS(Y2))
600 LET B2=B2+80/276*W/D^2*S2*SIN(Y2)/(C2-COS(Y2))^2
610 LET B3=B3+80/276*W/D*S2/(C2-COS(Y2))
620 LET B4=B4+80/276*W/D^2*(C2*COS(Y2)-1)/(C2-COS(Y2))^2
630 D1=(E1+E3+E7)*0.0479-0.00295*E3*E9
640 D2=(E4+E6+E7)*0.0479-0.00295*E6*E9
650 D3=-0.382/N*(-A2-B2+1.17*(A4+B4))
660 D4=-0.382/N*(A4+B4+1.17*(A2+B2))
670 D5=D1*D3+D2*D4
680 IF D5<0 THEN 710
690 PRINT X,X/W,D5,LGT(D5)
700 GO TO 720
710 PRINT X
720 NEXT X
730

```

PROGRAM #4: INTERFACE-PARTICLE STRAIN INTERACTION / FINITE PARTICLE SOLUTION /  $\epsilon_{ij}^T$  - IPS

```

100 INIT
110 PRINT "STRUCTURE MISFIT"
120 PRINT "N9,Z,W,D9,I,F,S,S9"
130 INPUT N9,Z,W,D9,I,F,S,S9
140 PRINT "E1 THROUGH E9"
150 INPUT E1,E2,E3,E4,E5,E6,E7,E8,E9
160 PAGE
170 PRINT "STRUCTURE MISFIT"
180 PRINT "TWINNED PARTICLES"
190 PRINT 5*S9;"A PARTICLE SIZE"
200 PRINT "PARTICLE PATH IS Y= 1.17**X-";-2
210 PRINT "X", "X-W", "FORCE"; "LOG(FORCE)"
220 PRINT
230 R=0
240 FOR X9=1 TO F STEP S
250 LET D5=0
260 LET D6=0
270 LET Y9=1.17**X9+2
280 FOR P=-2 TO 2
290 LET X=X9+P*S9
300 N=N9
310 Q=Q9
320 FOR Q=-2 TO 2
330 LET Y=Y9+Q*X9
340 A1=0
350 A2=0
360 A3=0
370 A4=0
380 B1=0

```

```

440 B2=0
450 B3=0
460 B4=0
470 IF 2*3.141*ABS(X/D)>40 THEN 490
480 GO TO 520
490 LET N=N/2
500 LET D=D*2
510 GO TO 470
520 LET Y1=2*3.141*X/W
530 LET S1=(EXP(X1)-EXP(-X1))/2
540 LET C1=(EXP(X1)+EXP(-X1))/2
550 LET X2=2*3.141*X/D
560 LET S2=(EXP(X2)-EXP(-X2))/2
570 LET C2=(EXP(X2)+EXP(-X2))/2
580 FOR N=INT(N) TO INT(N) STEP 1
590 LET Y1=2*3.141*(Y+M*D)/W
600 LET A1=A1+SIN(Y1)/(C1+COS(Y1))
610 LET A2=A2+SIN(Y1)*S1/(C1+COS(Y1))^2
620 LET A3=A3+S1/(C1+COS(Y1))
630 LET A4=A4+(C1*COS(Y1)+1)/(C1+COS(Y1))^2
640 NEXT M
650 LET Y2=2*3.141*Y/D
660 LET B1=B1+80.276*M/D*SIN(Y2)/(C2-COS(Y2))
670 LET B2=B2+80.276*M/D^2*S2*SIN(Y2)/(C2-COS(Y2))^2
680 LET B3=B3+80.276*M/D*S2/(C2-COS(Y2))
690 LET B4=B4+80.276*M/D^2*(C2*COS(Y2)-1)/(C2-COS(Y2))^2
700 D1=(E1+E9+E3*E7)*0.8479-0.00295*E3*E9
710 D2=(E4+E9+E6*E7)*0.8479-0.20295*E7*E9
720 D3=0.382/N*(A2-B2+1.17*(A4+E4))
730 D4=0.382/N*(A1+B4+1.17*(A2+B2))
740 D5=D5+(D1*D3+D2*D4)
750 R=R+1
760 NEXT P
770 NEXT Q
780 LET D6=D5/25

```

```
790 IF D6<=0 THEN 820
800 PRINT X9, X9/N, D6, LGT(D6)
810 GO TO 830
820 PRINT X9, X9/N, D6
830 NEXT X9
840 END
```

PROGRAM #5: INTERFACE-PARTICLE STRAIN INTERACTION/ SMALL PARTICLE SOL. /  $\epsilon_{ij}^T$  -ORTHORHOMBIC DISTORTION

```

100 INIT
110 PRINT "STRUCTURE MISFIT"
120 PRINT "N9,Z,W,D9,I,F,S"
130 INPUT N9,Z,W,D9,I,F,S
140 PRINT "E1 THROUGH E9"
150 INPUT E1,E2,E3,E4,E5,E6,E7,E8,E9
160 PAGE
170 PRINT "STRUCTURE MISFIT"
180 PRINT "SMALL PARTICLE APPROXIMATION"
190 PRINT "PARTICLE PATH IS Y= 1.17*X"-";-Z
200 PRINT "X", "X/W", "FORCE", "LOG(FORCE)"
210 FOR X=1 TO F STEP S
220 N=N9
230 D=D9
240 A1=0
250 A2=0
260 A3=0
270 A4=0
280 B1=0
290 B2=0
300 B3=0
310 B4=0
320 LET Y=1.17*X+Z
330 IF 2*3.141*ABS(X-D)>40 THEN 400
340 GO TO 430
350 LET N=N/2
360 LET D=D*2
370 GO TO 380
380 LET X1=2*3.141*X/W
390
400
410
420
430

```



```

440 S1=(EXP(X1)-EXP(-X1))/2
450 C1=(EXP(X1)+EXP(-X1))/2
460 X2=2*X3.141*X/D
470 S2=(EXP(X2)-EXP(-X2))/2
480 C2=(EXP(X2)+EXP(-X2))/2
490 M=-INT(N)/INT(N) STEP 1
500 Y1=2*3.141*(Y+M*D)/W
510 LET A1=SIN(Y1)/(C1+COS(Y1))
520 LET A2=SIN(Y1)*S1/(C1+COS(Y1))^2
530 LET A3=S1/(C1+COS(Y1))
540 LET A4=A4+(C1*COS(Y1)+1)/(C1+COS(Y1))^2
550 NEXT M
560 LET Y2=2*3.141*X/D
570 LET B1=81+90/276*X/D+SIN(Y2)/(C2-COS(Y2))
580 LET B2=82+90/276*X/D+2*92*SIN(Y2)/(C2-COS(Y2))^2
590 LET B3=83+90/276*X/D+92/(C2-COS(Y2))
600 LET B4=84+90/276*X/D+2*(C2*COS(Y2)-1)/(C2-COS(Y2))^2
610 D1=E1*E7*0.06-E2*E8*0.086+E3*E9*0.023
620 D2=E4*E7*0.06-E5*E8*0.086+E5*E9*0.023
630 D3=0.382/M*(-A2-B2+1.17*(A4+B4))
640 D4=0.382/M*(A4+B4+1.17*(A2+B2))
650 D5=D1*D3+D2*D4
660 IF D5<=0 THEN 690
670 PRINT X,X/W,D5,LGT(D5)
680 GO TO 700
690 PRINT X,X/W,D5
700 NEXT X
710 END

```

REFERENCES

1. F. C. Frank, Symposium of the Plastic Defm. of Crystn. Solids, p.150 The Physical Society, London (1950).
2. B. A. Bilby, Rep. Conf. on Defects in Crystn. Solids, p. 124, The Physical Society, London (1955).
3. W. Bollman, Crystal Defects in Crystalline Interfaces, Spring-Verlag; Berlin (1970).
4. J. W. Christian, Proc. 1st JIM Int. Symp. on New Aspects on Mart. Trans. , Suppl. Trans. JIM, p.21 (1970).
5. R. Bullough and B. A. Bilby, Proc. Phys. Soc., 69B, 1276 (1956).
6. M. S. Wechsler, D.S. Lieberman and T.A. Read, Trans. AIME, 197, 1503 (1953).
7. J.S. Bowles and J.K. Mackenzie, Acta. Met. 2 ,129 (1954).
8. J.W. Christian, Summer School on Martesite, Leuven Belgium, 1982.
9. A.P. Sutton and J.W. Christian, Proc. ICOMAT-82, Leuven Belgium, J. de Phys. 43, C4-197 (1982), Suppl.#12.
10. K.V. Vladimirovskiy, Zh. Eksper. Teor. Fiz., 17, 530 (1947).
11. F.C. Frank and J. H. van der Merwe, Proc. Roy. Soc., A198, 205 (1949).
12. J.W. Christian, Met. Trans., 13A, 599 (1982).
13. F.C. Frank, Phyl. Mag., 42, 809 (1951).
14. G.B. Olson, Acta Met., 29, 1475 (1981).
15. W.S. Owen, F.S. Schoen and G.R. Shrinivasan, Phase Transformations, ASM Metals Park, Ohio, p.157 (1970).
16. G.B. Olson and M. Cohen, Acta. Met., 27, 1907 (1979).
17. G.B. Olson and M. Cohen, Ann. Rev. Mat. Sci., 11, 1(1981).
18. G.B. Olson and M. Cohen, Proc. Int'l. Conf. Solid State Phase Transformations, Carnegie Mellon Univ., 1981, in press.
19. P. Kluge-Weiss and H. Gleiter, Acta Met., 26, 117 (1978).
20. J.W. Matthews, Surf. Sci., 31, 241 (1972).
21. M.G. Hall, H.I. Aaronson and K.R. Kinsman, Surf. Sci., 31, 257 (1972).

22. C.M. Wayman, Proc. Int'l. Conf. Solid State Phase Trans., Carnegie Mellon Univ. 1981, in press.
23. R. Sinclair, Proc. 35th Annual Meeting EMSA p.110, Claiborne's, Baton Rouge (1977).
24. S. Maharajan and G.Y.Chin, Acta Met., 21, 1353 (1973).
25. S. Maharajan, Phil. Mag., 26, 161 (1972).
26. J.A. V nables, Phil. Mag., 1, 35 (1962).
27. F. Forster and E. Scheil, Z. Metalk., 32, 165 (1940).
28. K. Oishi and L.C. Brown, Met. Trans., 2, 1971 (1971).
29. K. Otsuka, K. Nakai and K. Shimizu, Scripta Met., 8, 913 (1974).
30. L.A. Shepard, Shape Memory Effect in Alloys, ed. by J. Perkins, Plenum Publ., New York (1975), p. 419.
31. K. Otsuka, C.M. Wayman, K.Nakai, H. Sakamoto and K. Shimizu, Acta Met., 24, 207 (1976).
32. H. Sakamoto, M. Tanigawa, K. Otsuka and K. Shimizu, Proc. ICOMAT-79, Cambridge, Ma, p.633.
33. G.B. Olson And M. Cohen, Met. Trans., 7A, 1915 (1976).
34. P. Gaunt and J.W. Christian, Acta Met., 7, 529 (1959).
35. A.H. Cottrell and B.A. Bilby, Phil. Mag., 42, 573 (1951).
36. G.B. Olson and M. Cohen, Scripta Met., 9, 1247 (1975).
37. G.B. Olson and M. Cohen, Scripta Met., 11, 345 (1977).
38. Shape Memory Effects in Alloys, ed. by J. Perkins, Plenum Press New York (1975).
39. S. Kajiwara and W.S. Owen, Met. Trans., 4, 1988 (1973).
40. S. Kajiwara and W.S. Owen, Met. Trans., 5, 2047 (1974).
41. S. Kajiwara, Proc. 1st JIM Symp. on New Aspects of Martensitic Transformation, Kobe (1976), p.81.
42. T. Tadaki, T. Kakeshita and K. Shimizu, Proc. ICOMAT-82, Leuven Belgium, J.de. Phys., 43, C4-191 (1982), Suppl.#12.
43. S Kajiwara and T. Kikuchi, Acta Met., 36, 589 (1982).

44. G. Krauss Jr., Acta Met., 11, 499 (1963).
45. M. Murakami, O. Kawano and Y. Murakami, J.Inst. Metals, 99,160 (1971).
46. K. Wakasa and C.M. Wayman, Acta Met., 29, 1013 (1981).
47. D.M. Haezebrouck, MIT, doctoral research in progress.
48. V.F. Kocks, A.S. Argon and M.F. Ashby, Prog Mat . Sci., 19, (1975).
49. M.O. Peach and J.S.Koehler, Phys. Rev., 80, 36 (1950).
50. F.C. Frank, Proc. Phys. Soc. , A62, 131 (1949).
51. J. Lothe, Phys. Rev., 33, 2116 (1962).
52. F.R.N. Nabarro, Theory of Crystal Dislocations, Oxford University Press (1967).
53. A.D. Brailsford, J. Appl. Phys., 43, 1380 (1972).
54. A.V. Granato, Metallurgical Effects at High Strain Rates, Plenum Press, New York (1973) p.255.
55. J.D. Eshelby, Proc. Phys. Soc., B69, 1013 (1956).
56. J Weertman, J. Mech. Phys. Solids, 11, 197 (1963).
57. W.G. Johnston and J.J. Gilman, J. Appl. Phys., 30, 129 (1959).
58. J.J. Gilman, Micromechanics of Flow in Solids, McGraw-Hill (1969).
59. J.P. Hirth and J. Lothe, Theory of Dislocations, McGraw-Hill New York (1968).
60. R.E. Peierls, Proc. Phys. Soc., 52, 34 (1940).
61. F.R.N. Nabarro, Proc. Phys. Soc., 59, 256 (1947).
62. H. Conrad, J. Metals, 10, 582 (1964).
63. J.C.M. Li, Trans. Met. Soc.AIME, 233, 219 (1965).
64. C. Rodriguez and L.C. Brown, Met. Trans., 11A, 147 (1980).
65. L.C. Brown, Met. Trans., 12A,1491 (1981).
66. L.C. Brown, Scripta Met.,16, 1001 (1982).
67. E. Papadakis, J. Appl. Physics, 35,1479 (1964).
68. K. Otsuka and K. Shimizu, Trans. JIM, 15, 103 (1974).

69. N.F. Kennon and D.F. Dunne, *Acta Met.*, 30, 429 (1982).
70. E. Schmid and W. Boas, *Plasticity of Crystals*, Hughes (1950).
71. K. Otsuka, K. Nakai and K. Shimizu, *Scripta Met.*, 8, 913 (1974).
72. K. Otsuka, C.M. Wayman, K. Nakai, H. Sakamoto and K. Shimizu, *Acta Met.*, 24, 207 (1976).
73. J.W. Christian, *Met. Trans.*, 13A, 509 (1982).
74. M.L. Green, M. Cohen and G.B. Olson, *Mat. Sci. and Eng.* 50, 109 (1981).
75. L.A. Shepard, *Shape Memory Effects in Alloys*, ed. by J. Perkins, Plenum Publ., New York (1975) p. 419.
76. K. Otsuka and K. Shimizu, *Phil. Mag.*, 24, 481 (1971).
77. K. Otsuka, T. Nakamura and K. Shimizu, *Trans. JIM*, 15, 200 (1974).
78. C. Kittel, *Introduction to Solid State Physics*, 4th Edn., Wiley, New York (1971).
79. A. Nagasawa, N. Nakanishi, Y. Matsuo and K. Enami, *Proc. ICOMAT-79*, Cambridge, M, p. 423.
80. H.B. Huntington, *The Elastic Constants of Crystals*, Academic Press, New York (1958).
81. H.C. Ling and W.S. Owen, *Scripta Met.*, 15, 1115 (1981).
82. A. Nagasawa and Y. Ueda, *J. Phys. Soc. Japan*, 45, 1249 (1978).
83. G.M. McManus, *Phys. Rev.*, 129, 2004 (1963).
84. P. Young and A. Bienenstock, *J. Appl. Phys.*, 42, 3008 (1971).
85. A. Prasetio, F. Reynaud and H. Warlimont, *Acta Met.*, 24, 1009 (1976).
86. R.J. Schilz, T.S. Preveder and J. F. Smith, *J. Appl. Phys.*, 42, 4680 (1971).
87. N. Nakanishi, Y. Murakami and S. Kachi, *Scripta Met.*, 5, 433 (1971).
88. M. Suesawa and K. Sumino, *Scripta Met.*, 10, 789 (1976).

89. G. Guenin, M. Morin, P.F. Gobin, M. Dejonge and L. Delaey Scripta Met., 11, 1071 (1977).
90. G. Guenin and P.F. Gobin, Met. Trans., 13A, 1127 (1982).
91. O.L. Anderson, Physical Acoustics IIIB, Academic Press, New York (1965).
92. W. Voight, Lehrbuch der Kristall Physik, Tuerner Verlag, Leipzig (1928).
93. A. Reuss, Z. angew. Math., 9, 49 (1929).
94. R. Hill, Proc. Roy. Soc., A65, 349 (1952).
95. G.B. Olson and M. Cohen, Proc. Int'l Conf. Solid-Solid Phase Transformations, Carnegie Mellon Univ., (1981) in press.
96. D. R. Swann and H. Warlimont, Acta Met., 11, 511 (1963).
97. G.V. Kurdjumov, J. of Metals, 11, 449 (1959).
98. H.C. Ling and W.S. Owen, Acta Met., 29, 1721 (1981).
99. Metals Handbook, vol. 8, ASM 8th edition, p. 37,
100. A.J. Bradley, Phil. Mag., 6, 878 (1928).
101. A.J. Bradley and P.Jones, J. Inst. Metals, 51, 131 (1933).
102. A.J. Bradley, H.J. Goldsmith and H. Lipson, J. Inst. Metals, 63, 149 (1938).
103. W.O. Alexander, J. Inst. Metals, 63, 163 (1938).
104. E.E. Underwood, Quantitative Stereology, Addison-Wesley, (1970), p.148.
105. L. Delaey, A.J. Perkins and T.B. Massalski, J. Mater. Sci., 7, 1197 (1972).
106. A. Prasetyo, F. Reynaud and H. Warlimont, Acta Met., 24, 651 (1976).
107. A. Prasetyo, F. Reynaud and H. Warlimont, Acta Met., 24, 1009 (1976).
108. W. Vandermeulen and A. Deruyterre, Met. Trans., 4, 1659 (1976).
109. K. Takezawa and S. Sato, J. Jap. Inst. Metals, 37, 793 (1973).

110. Y. Murakami, L. Delaey and G.S. Dulenkopf, J. Jap. Inst. Metals, 19, 317 (1973).
111. K. Otsuka, H. Sakamoto and K. Shimizu, Trans. JIM, 20, 244 (1979).
112. L. Delaey, G. van Tendelo, J. van Landuyt and Y. Murakami, Proc. ICOMAT-79, Cambridge, Ma, p. 520.
113. H. Kubo and C.M. Wayman, Proc. ICOMAT- 79, Cambridge, Ma, p.532.
114. P. van Houte, E. Aernoudt and L. Delaey, Metallography, 6, 393 (1973).
115. H. Warlimont, Proc. 6th Intr'l. Congress for Electron Microscopy, Kyoto (1966), p. 437.
116. D.A. Karlyn, J.W. Cahn and M. Cohen, Trans. Met.Soc. AIME, 245, 197 (1969).
117. H. Pops and M. Ahlers, in The Mechanisms of Phase Transformations in Crystalline Solids, Institute of Metals Monograph No.33, London (1969) p.197.
118. J.D.C. McConnell, MIner. Mag., 38, 1 (1971).
119. L.E. Tanner, A.R. Pelton and R. Gronsky, Proc. ICOMAT-82, Leuven Belgium, J.de Physique, 43, C4-169 (1982), Suppl. #12.
120. K. Otsuka, C.M. Wayman and H. Kubo, Met. Trans., 9A, 1075 (1978).
121. K.Otsuka, H. Kubo and C.M. Wayman, Met. Trans., 12A, 595 (1981).
122. L. Delaey and H. Warlimont, Shape Memory Effects in Alloys, ed. by J. Perkins, Plenum Publ., New York, (1975), p.89.
123. M.J. Duggin and W.A. Rachinger, Acta Met.,12, 529 (1969).
124. K. Otsuka and K. Shimizu, Jap. J. Appl. Phys. , 8, 1196 (1969).
125. K. Otsuka, M. Takahashi and K. Shimizu, Met. Trans., 4, 2003 (1973).
126. K Otsuka and K Shimizu, Trans. JIM, 15, 109 (1974).
127. J.W. Christian, Theory of Transformation in Metals and Alloys, Pergamon Press, (1965), p. 774.
128. J. P. Hirth and J. Lothe, Theory of Dislocations, McGraw-Hill, New York(1968) p. 265.
129. P. Guyot and J.E. Dorn, Can. J. Phys., 45, 983 (1967).

130. H. Sakamoto, M Tanigawa, K.Otsuka and K. Shimizu, Proc. ICOMAT-79 Cambridge, Ma, p. 633.
131. J.D. Eshelby, Prog. Solid Mechanics, 2, 89 (1961).
132. C.S. Smith, Trans. AIME, 175, 47 (1948).
133. K.Otsuka, Jap. J. Appl. Phys., 10, 571 (1971).
134. K. Otsuka and k. Shimizu, J. Phys. Soc. Japan, 28, 804 (1970).
135. M. Yasunaga, Y. Funatsu, S. Kojima, K. Otsuka and T. Suzuki, Proc. ICOMAT-82, Leuven Belgium, J.de Physique, 43, C4-603 (1982), Suppl. #12.
136. J.W. Cahn, Acta Met., 11,1275 (1963).
137. M. Kato, T. Mori and L.H. Schwartz, Acta Met., 28,285 (1980).
138. M. Kato, T. Mori and L.H.Schwartz, Mat. Sci. and Eng., 51, 25 (1981).
139. T. Tadaki, T. Kakeshita and K. Shimizu, Proc. ICOMAT-82, Leuven Belgium, J. de Physique, 43, C4-191 (1982), Suppl. #12.
140. M. Cohen, private communication, MIT, 1983.
141. K. Otsuka and C.M. Wayman, Scripta Met., 9, 1017 (1975).
142. H. Sakamoto, K.Shimizu and K.Otsuka, Proc. 1st JIM Intr'l. Symp. on New Aspects of Martensitic Transformation, Kobe, (1976).
143. K.Otsuka, H. Sakamoto and K. Shimizu, Scripta Met.,10, 983 (1976).
144. K.Otsuka and K.Shimizu, Trans. JIM, 15, 103 (1974).
145. K.Otsuka and K.Shimizu, Trans. JIM, 15, 109 (1974).
146. D.S. Lieberman, M.A.Schmerling and R.W. Karz, in Shape Memory Effects in A-loys, ed. by J. Perkins, Plenum Publ., New York, (1975) p. 203.
147. G.B. Olson and M.Cohen, Met. Trans., 7A, 1905 (1976).
148. G.B. Olson and M. Cohen, Proc. ICOMAT- 82, Leuven Belgium, J. de Phys.,43, C4-75 (1982), Suppl.#12.
149. M. A. Collins, A. Blumen, J.F. Currie and J.Ross, Phys.Rev., 19, 3630 (1979).
150. J.F.Currie, A.Blumen, M.A. Collins and J. Ross, Phys. Rev.,19, 3645 (1979).



151. A.L. Roitburd, Kristalligrafiya, 7, 291 (1962).
152. L. Kaufman and M. Cohen , Prog. Met. Phys., 7, 165 (1958).
153. V. Raghavan and M. Cohen, Acta Met., 20, 333(1972).
154. G.B. Olson and M.Cohen, Proc. ICOMAT-79, Cambridge, Ma, p. 310.
155. J.W. Christian, Theory of Phase Transfprmtions in Metals and Alloys, Pergamon Press, Oxford p. 816.
156. V.Raghavan and M. Cohen, Acta Met., 20,779 (1972).
157. H.S. Carslaw and J.C. Jeager, Conduction of Heat in Solids, Claredon Press Oxford (1958).
158. Z. Nishiyama, A. Tsubaki, H. Suzuki and Y Yamada, J, Phys, Soc, Japan, 13,1084 (1958).
159. R.J. Salzbrenner and M. Cohen, Acta Met., 27, &39 (1979).

BIOGRAPHICAL NOTE

The author was born on January 25, 1952, in Valjevo, Serbia-Yugoslavia where he was raised. His secondary school education culminated in graduation from the Valjevo High School in 1971. Following this, he entered the Belgrade University and earned a B.S. degree in Metallurgy in 1975. From 1975 to 1980, he was employed at the Institute for Nuclear Science, Vinca, Yugoslavia, during which time he received an M.S. degree in Metallurgy from the Belgrade University. He then enrolled in the Department of Materials Science and Engineering at the Massachusetts Institute of Technology and was accepted as a candidate for the degree of Doctor of Philosophy in Metallurgy in February of 1980. He will receive this degree in June of 1983.